Dissertation
submitted to the
Combined Faculties for the Natural Sciences and for Mathematics
of the Ruperto-Carola University of Heidelberg, Germany
for the degree of
Doctor of Natural Sciences

Put forward by
Tessel Petri Roeltje van der Laan, M.Sc.
Born in: Gouda, The Netherlands
Oral examination: 19 October 2012

# Circumnuclear star forming rings
# in the barred galaxies
# NGC 5248 and NGC 6951

## Zusammenfassung

In dieser Doktorarbeit beobachte ich die Gasverteilung und -dynamik, sowie die stellaren Populationen in den zirkumnuklearen Sternentstehungsringen der nahen Galaxien NGC 5248 und NGC 6951. Zirkumnukleare Sternentstehungsringe sind Regionen mit einer hohen Gasdichte und Sternentstehungsrate, die sich in den Zentren von Galaxienscheiben befinden. Diese Sternentstehungsringe können durch anhaltenden Gaszufluss in Richtung des Kerns einen starken Einfluss auf die Entwicklung von Galaxien haben. Die Gasmassen, die sich in diesen Ringen aufbauen, sind hoch, wodurch es zu intensiver Sternentstehung kommt. Daher sind zirkumnukleare Sternentstehungsringe auch ein wichtiges Instrument zum Aufbau der zentralen stellaren Verdickung. Die beiden Galaxien wurden ausgewählt, weil sie sehr ähnliche globale Eigenschaften (Masse, Größe, Metallizität), aber sehr unterschiedliche zirkumnukleare Regionen besitzen; in beiden sind zirkumnukleare Sternentstehungsringe vorhanden, aber nur eine besitzt einen aktiven Kern. Detaillierte Untersuchungen der beiden Galaxien, und ihr Vergleich decken die Wechselwirkung zwischen zirkumnuklearen Sternentstehungsringen und der gesamten zentralen Region auf.

Drei zentrale Fragen werden in dieser Arbeit behandelt. Zuerst untersuche ich in diesen beiden Galaxien die Wirksamkeit der zirkumnuklearen Ringe als Gasbarriere. Des weiteren studiere ich, wie Sternentstehung in diesen Ringen verläuft und wie diese in Verbindung zu dem Gasfluss in den Ring steht. Als dritten Punkt messe ich außerdem noch das Alter und die Lebensdauer der zirkumnuklearen Ringe mit Hilfe ihrer stellaren Populationen. In beiden Galaxien sind die zirkumnuklearen Ringe wirksame, aber nicht absolute Barrieren. Die Wechselwirkung zwischen dem stellaren Balken, dem zirkumnuklearen Ring und anderen dynamischen Komponenten in der zirkumnuklearen Region erlaubt es einigem Gas aus dem Ring hinaus weiter nach innen zu strömen. Bezüglich der Art und Weise wie Sternentstehung im Ring vonstattengeht, habe ich entdeckt, dass in beiden Galaxien die Position der jüngsten Sterne im Ring in Verbindung mit der Position des einströmende Gases auf den Ring steht. Das hohe Alter der Ringe von etwa 1.5 Gyr, dass meine Analysis ergibt, bedeutet, dass die zirkumnuclearen Sternentstehungsringe viel Zeit haben, um die Zentren ihrer Galaxien umzumodelieren.

**Summary**

In this thesis I study the gas distribution and dynamics, as well as the stellar populations, in the circumnuclear star forming rings in the nearby barred galaxies NGC 5248 and NGC 6951. Circumnuclear star forming rings are regions of high gas and star formation density in the centers of disk galaxies. These star formation rings can have a strong influence on the secular evolution of their host galaxies, by halting gas inflow towards the nucleus. The gas masses that build up in these rings are high and this consequently leads to intense star formation. This makes circumnuclear star forming rings also an important tool to build up the stellar (pseudo-)bulge. These two galaxies were selected because they have very similar global properties (mass, size, metallicity), but very different circumnuclear regions, both of which containing circumnuclear star forming rings. Detailed investigation of both, and a comparison between them, thus provides new detailed insight on the interplay between circumnuclear star forming rings and the circumnuclear region as a whole.

Three questions are addressed in this work. First of all, I investigate the true effectiveness of the circumnuclear rings as a gas barrier in both galaxies. I study star formation progression in these rings and its relation to the gas flow onto the ring. The age and life span of the circumnuclear rings is derived from the analysis of their stellar populations. In both galaxies I find that while the circumnuclear rings are effective barriers, they are not absolute ones. The interplay between the large scale stellar bar, circumnuclear ring and other dynamical components in the circumnuclear region allows some gas to flow towards the very center past the ring. I find that the location of the youngest stars in the ring is close to the inflow position of the gas onto the ring in both galaxies, consistent with star formation proceeding in a 'pearls-on-a-string' mechanism with the youngest 'pearls' close to the gas inflow location. Finally, I derive ages of the rings around 1.5 Gyr, which implies that circumnuclear star forming rings have a significant amount of time to shape the circumnuclear regions of their host galaxies.

# Contents

# List of Figures

# List of Tables

# 1

# Introduction

The agents of galaxy evolution can be divided into two broad categories (Kormendy & Kennicutt, 2004); interactions with the external environment (e.g. major and minor mergers, infall of large gas reservoirs; the right side of Fig. 1.1), or internal changes (e.g. mass transport due to stellar bars and spiral asymmetries, nuclear black holes, galactic winds; the lower-left corner of Fig. 1.1). The latter are often referred to as (internal) secular evolution. In the dense environment of the high-redshift Universe the former mechanisms dominated galaxy evolution. As the Universe has been expanding, and especially now that this expansion has been speeding up (since z∼0.7), the external environment is no longer the single dominant influence on galaxy evolution. This does not mean that mergers and gas inflow along intergalactic filaments does not happen anymore - especially in groups or clusters of galaxies are environmental effects still important - but secular processes now change galaxies on time scales equal to, or faster than, the external actors. Secular evolution is especially important for the centers of galaxies, where the dynamical timescales are very short (of order a few Myr).

Secular evolution encompasses changes in both the gaseous and stellar mass distributions. Asymmetries in the gravitational potential, such as spiral arms and large scale stellar bars, are important agents of secular evolution (Fig. 1.1). Spiral arms and bars funnel gas inwards to small galactocentric radii and outwards to the edge of the disk. The increased concentration of gas in the central regions can lead to star formation, which in turn may lead to the build up of a (pseudo-)bulge (see Kormendy & Kennicutt, 2004, for the latest review on this topic). This means that secular evolution can alter a galaxy's Hubble type. Also, the inflow of gas to the very center can power an active galactic nucleus (AGN) phase whose feedback can quench inflow and star formation in the galaxy (Rees, 1984; Shlosman et al., 1990).

The aim of this thesis is to understand the role that circumnuclear star forming rings play in the secular evolution of galaxies. Circumnuclear rings have radii of 50 pc to 1 kpc and are present in the central regions of ∼20% of all nearby disk galaxies (Knapen, 2005; Comerón et al., 2010). They act as gas reservoirs, halting gas inflow, and are strongly star forming, with star formation rates of up to 50 times that of quiescent star forming galaxy disks (Kennicutt, 1998a). Depending on their life times they may build up large stellar masses in the central region.

In this thesis I study the following aspects of circumnuclear star forming rings in the two nearby galaxies, NGC 5248 and NGC 6951, using multi-wavelength data.

**Protogalactic collapse**

internal versus external

**Galaxy mergers, RAM-pressure stripping of gas**

fast versus slow

star formation,
gas recycling,
metal enrichment,
energy feedback via supernovae,
etc.

fast versus slow

**Internal secular evolution**

driven by bar instabilities,
by dark matter halos,
by bars and oval distortions,
by spiral structure,
by nuclear black holes,
by galactic winds & fountains,
etc.

internal versus external

**Environmental secular evolution**

driven by prolonged gas infall,
by minor mergers,
by galaxy harassment,
etc.

Figure 1.1: Schematic overview of the various processes that can occur in galaxy evolution. The processes are divided into fast vs. slow (vertical) and internal vs. external (horizontal). Fast vs. slow refers to the time scale upon which the evolution happens with respect to the dynamical timescale of the system. Slow evolution needs many dynamical times. Internal vs. external refers to whether the process is internal to the galaxy or if the environment plays a role. Examples for each type of evolutionary agent are given in each corner. Figure adapted from Kormendy & Kennicutt (2004).

I study the gas dynamics in and around their circumnuclear rings to determine how circumnuclear star forming rings influence gas dynamics and might quench nuclear feeding, and I analyze the stellar content in these rings to determine the life times of the rings and the duration and intensity of star formation episodes in the ring. These results are used to gain new insights in the role and importance of circumnuclear ring for shaping/modeling the central region of galaxies.

This introductory chapter provides an overview of the current state of understanding on the topics discussed in this thesis; gas motion in disk galaxies (Sect. 1.1), the relation between (dense) gas and star formation (Sect. 1.2), and highlight the position of circumnuclear star forming rings in both. I will finish this chapter with an explanation of the target selection and the instrument choices made to study the circumnuclear rings in NGC 5248 and NGC 6951 observationally (Sect. 1.3).

## 1.1 Gas motion in disk galaxies

During the evolution of the Universe, local overdensities of gas collapse under gravity, and transforms into primordial galaxies. The gas in these galaxies, as it cools, will settle into a disk. The reason is the following. By cooling, gas will lose kinetic energy, which moves the system as a whole to its lowest energy, but gas cannot lose all its energy, since angular momentum in the system must be preserved. Angular momentum is a vector ($\vec{L} = \vec{r} \times m\vec{v}$), and the orientation of $\vec{L}$ must also stay constant. Perpendicular to this axis will thus be the lowest kinetic energy ($E_{kin} = \frac{1}{2}mv^2$) state for a gas particle, since the angular momentum sets the minimal gas velocity.

Angular momentum must be preserved for the system as a whole, but it can be redistributed within the system. Reducing angular momentum allows matter to move to even more energy efficient states. Several mechanisms enable angular momentum transfer depending on whether the carrier is collisional (gas) or collisionless (stars). Stars can transfer angular momentum to dark matter haloes (Athanassoula, 2002, 2003), or, when this is not possible, small stellar mass packages can move outward and carry most of the angular momentum away, allowing most stellar mass to move inward. Gas can lose angular momentum through either viscosity, dynamical friction, magnetic fields (e.g. Beck, 2005) or gravitational torques. However, of the four, only gravitational torques are able to act over significant distances in a disk (e.g. Combes, 2004; García-Burillo et al., 2005).

Gravitational torques are generated by non-axisymmetries in the disk, such as spiral arms or large scale stellar bars. The non-axisymmetric distribution of mass results in a non-axisymmetric distribution of the gravitational potential. Each particle in a gravitational potential experiences a gravitational force due to that potential. Which leads to material being *torqued*, as described below.

Given a gravitational potential $\Phi(x, y, z)$ the gravitational force on a particle at position (x,y,z) will be $F(x, y, z) = -\nabla_{x,y,z}\,\Phi(x, y, z)$. Or, in cylindrical coordinates

$$F(r, \theta, z) = \frac{1}{r}\frac{\partial}{\partial r}(r\Phi_r) + \frac{1}{r}\frac{\partial}{\partial \theta}\Phi_\theta + \frac{\partial \Phi_z}{\partial z} \qquad (1.1)$$

The torque that a particle experiences due to the gravitational force, is given by $\vec{\tau} = \vec{r} \times \vec{F} = r F_\theta - \theta F_r$ (ignoring $F_z$, which is a valid assumption to first order in a disk). Torque is also the time derivative of angular momentum ($\vec{\tau} = \frac{\partial \vec{L}}{\partial t}$). Thus, when there is a *net* gravitational torque acting on the particle, the angular momentum of a particle will be changed. The angular momentum is absorbed/released by the perturbation that generates the torque.

In the central regions of the galaxies I will discuss in this thesis, the gravitational torques are provided by large scale stellar bars, so I will focus on their gravitational potentials from here on.

A large scale stellar bar is a bi-symmetric mass concentration centered on the nucleus, that rotates with a certain pattern speed, $\Omega_P$. As such, the gravitational torque distribution that it will produce is also bi-symmetric. Material that is in front of the bar as it rotates will get slowed down (negative torque), and material that is behind the bar will be sped up (positive torque). Thus, a four-part 'butterfly' pattern will be present, with alternating positive and negative torques at each radius (see Fig. 1.2).

Whether material loses or gains angular momentum depends on the *net* gravitational torque that this material experiences on its orbit. A large scale stellar bar is built up out of several families of closed stellar orbits. These orbits are not circular, but, to first approximation they can be described as oscillating around a circular orbit. The frequency of this oscillation is called the 'epicyclic frequency', $\kappa$, and its amplitude can be determined from the gravitational potential.

The primary stellar orbit family in a large scale stellar bar is called $x_1$ (following the nomenclature of Contopoulos & Papayannopoulos, 1980). The (1,2) oscillations of these orbits are closed in the inertial frame of the bar. (1,2) in this case means that $\kappa$ is such that stars on these orbits make two epicyclic oscillations every full rotation. In the inertial frame of the large scale stellar bar, these orbits are thus closed and elongated along the major axis of the stellar bar. Stars on these orbits always move with the bar and resonate with it (Lindblad, 1964).

The main resonances in a stellar bar potential are of the (1,2)-type (since the bar is bi-symmetric) and are called the inner (ILR) and outer (OLR) Lindblad resonances (Lindblad, 1964). A schematic diagram of them is given in Fig. 1.3. The angular speed of the disk and the epicyclic frequency vary with radius, while the bar is rotating with a fixed pattern speed. Each intersection between $\Omega - \kappa/2$ or $\Omega + \kappa/2$ and $\Omega_P$ basically give the radius of a Lindblad resonance. As can be seen, depending on $\Omega_P$ there can be zero, one, or two ILRs due to a large scale stellar bar. When there are two ILRs, they are distinguished by radius, and called inner (iILR) and outer (oILR) Lindblad resonance.

The flatness of the $\Omega - \kappa/2$ and $\Omega + \kappa/2$ curves means that (1,2) orbits are close to (i.e. in resonance with) the pattern speed $\Omega_P$ over significant ranges. The large scale stellar bar which is made up by them can thus exist over a large part of the disk, but cannot cross the CR. $x_1$ orbits primarily exist between the ILR (if there is one) or oILR (if there are two) and the co-rotation (CR) radius (Contopoulos & Papayannopoulos, 1980). Inside the (o)ILR $x_2$ orbits are the primary stable orbits. These stellar orbits are also (1,2), but now perpendicular to the major axis of the bar (see Fig. 1.4).

Stars can only exchange angular momentum with the bar at the Lindblad resonances
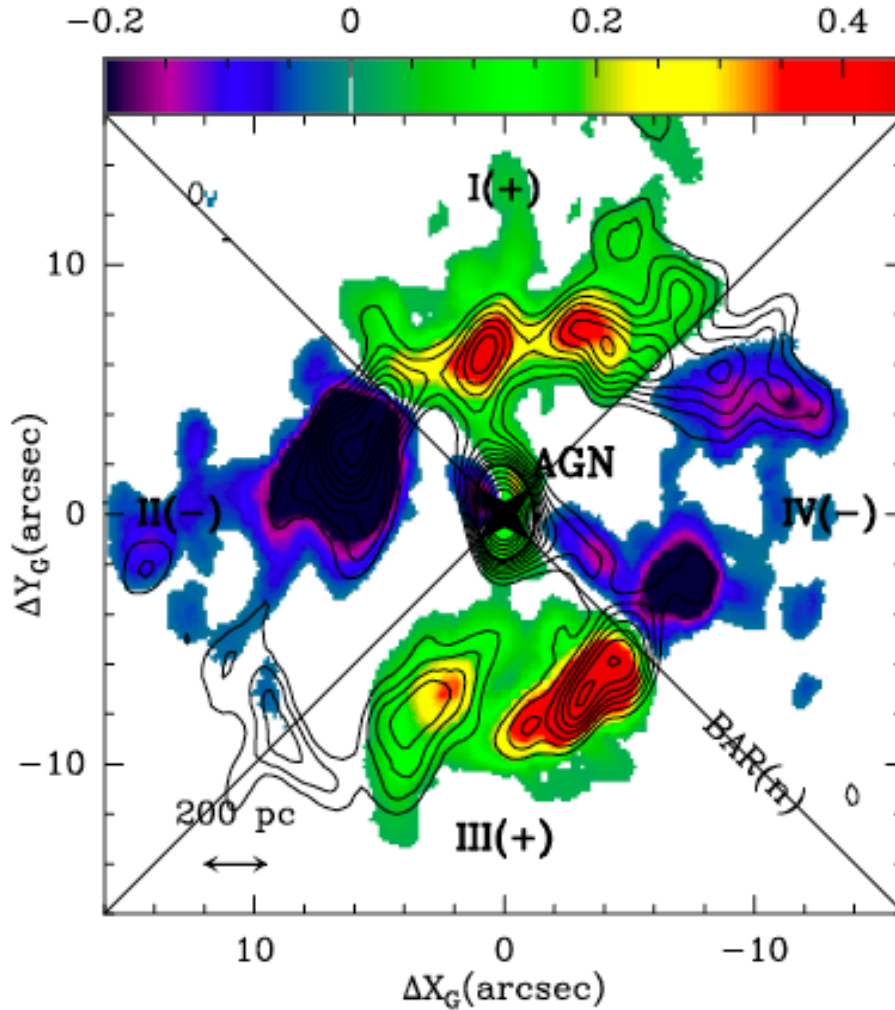
Figure 1.2: Example of the gravitational torques distribution in the central region of the barred galaxy NGC 4321. The 'butterfly' distribution of gravitational torques is visible, with the division clearly related to the orientation of the bar (PA 45° ). Positive torques are shown in green/red (quadrants I and III), and negative torques are shown in blue/purple (quadrants II and IV). Positive torques lead to outward motion, negative torques lead to inward motion. The *net* torque experienced by a particle on an orbit in this distribution determines whether a particle moves in- or outwards. The contours show the distribution of the molecular gas in the central region of NGC 4321. The rotation sense of NGC 4321 is counter-clockwise. Figure adapted from García-Burillo et al. (2005)
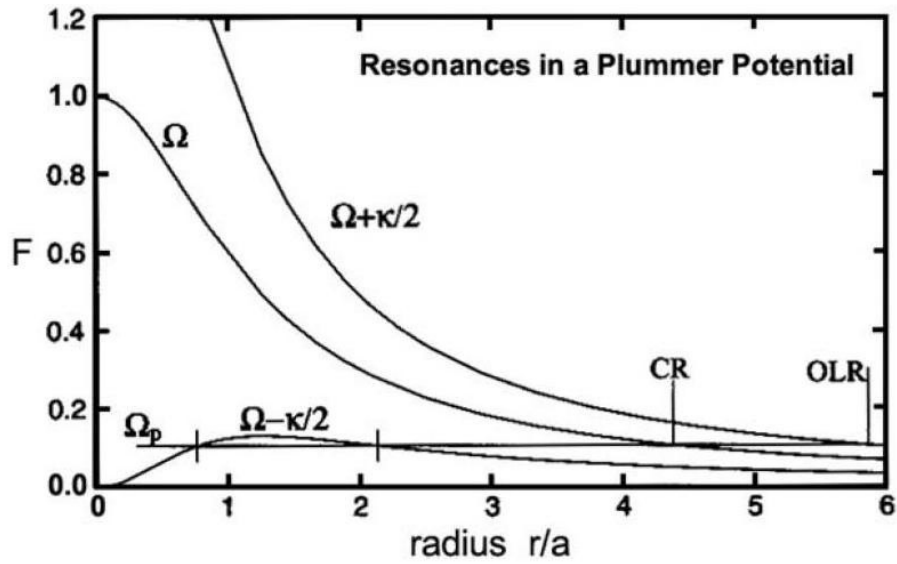
Figure 1.3: Schematic diagram of the main resonances in a barred galaxy. A large scale bar with pattern speed $\Omega_P$ will give rise to resonances at the intersections with the angular rotation curve and higher order curves. The main resonances are the inner Lindblad resonance(s) at the intersection of $\Omega_P$ with $\Omega - \kappa/2$ (may be zero, one or two depending on the exact value of $\Omega_P$), the corotation resonance at the intersection of $\Omega_P$ with $\Omega$ and the outer Lindblad resonance at the intersection of $\Omega_P$ with $\Omega + \kappa/2$. Figure adapted from Sparke & Gallagher (2000)
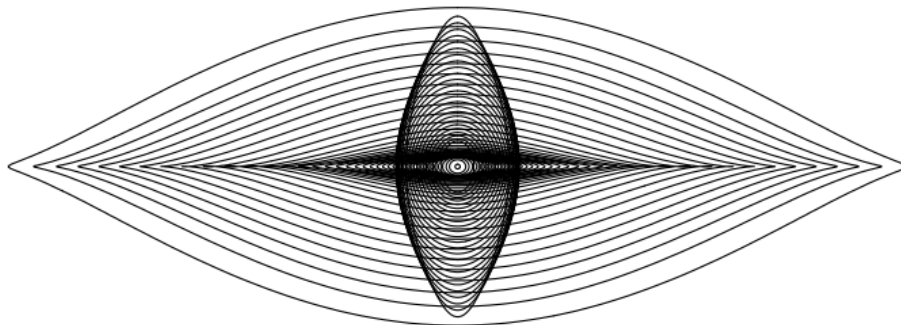


Figure 1.4: Representation of the $x_1$ (horizontal) and $x_2$ (vertical) stellar orbits in a large scale stellar bar potential. The large scale stellar bar's major axis is oriented horizontally in this figure. The $x_1$ orbits extend out to the semi-major axis of the large scale bar. The $x_2$ orbits cannot extend beyond the semi-minor axis of the large scale bar. Figure adapted from Regan & Teuben (2003)

or co-rotation radius (CR) (Binney & Tremaine, 2008). Gas is much better able to lose angular momentum, due to its collisional, dissipative nature.

Gas will try to follow the same orbits as the stars, but, since gas is dissipative, each radius can have only one orbit (compared to the crossing stellar orbits in Fig. 1.4). Therefore gas orbits must gradually change from parallel to perpendicular to the large scale stellar bar (Kalnajs, 1973). As the orbits become mis-aligned with the large scale bar, the *net* gravitational torque over an orbit is no longer zero and gas can exchange angular momentum at each radius. Inside CR the *net* gravitational torque on gas is negative and gas will move inward. At each resonance the orbits will have changed orientation by 90° , so inside ILR the *net* gravitational torque will be positive, while at the ILR the *net* gravitational torque would be zero. Therefore, in early computational models circumnuclear gas rings were generally formed near the ILR (Schwarz, 1981, 1984; Combes & Gerin, 1985; Byrd et al., 1994; Piner et al., 1995; Buta & Combes, 1996).

However, the existence of an ILR is not enough to form a circumnuclear gas ring. There are galaxies where the existence of ILRs is deduced, but no ring is found. More recent modeling of gas flows under the influence of large scale stellar bars has shown that circumnuclear rings and nuclear spirals are closely related (Englmaier & Shlosman, 2000; Regan & Teuben, 2003; Maciejewski, 2004a,b). Athanassoula (1992b) already showed that the existence of dust lanes/circumnuclear spirals offset from the semi-major axis is related to the presence of $x_2$ orbits. Regan & Teuben (2003) more specifically linked the existence of circumnuclear rings with $x_2$ orbits. They argue exclusively for the existence of $x_2$ orbits as a prerequisite for circumnuclear rings, not the existence of an ILR. Observationally, the location of ILR(s) and the region were $x_2$ orbits can exist, lie close together, leading to the continued mention of circumnuclear rings forming at the ILR in the literature.

Hydrodynamical modeling (Athanassoula, 1992b; Englmaier & Shlosman, 2000; Maciejewski, 2004b) also showed that the sound speed of the gas at the intersection between $x_1$ and $x_2$ orbits determines whether the inflow is damped (low sound speed), leading to the formation of a circumnuclear ring, or continues (high sound speed), leading to the formation of a nuclear spiral. The effectiveness of the circumnuclear ring as a gas barrier is thus high, but may not be absolute.

## 1.2 Star formation in the centers of nearby galaxies

Sakamoto et al. (1999) and later Sheth et al. (2005) showed from observations that the molecular gas fraction in the central regions of barred galaxies is higher than in unbarred ones, corroborating the role of stellar bars in moving gas inward. The high concentrations of molecular gas in the centers must lead to star formation. Indeed, most circumnuclear rings are detected via H$\alpha$ emission, which indicates that they are currently star forming (e.g. Mazzuca et al., 2008). Circumnuclear rings dominate the star formation in the central region when they are formed (Kormendy & Kennicutt, 2004). They may even dominate the star formation of the entire galaxy (Kennicutt et al., 2005).

The relation between the amount of gas present in (part of) a galaxy and the amount

of star formation that occurs because of it, is giving by the Kennicutt-Schmidt relation. This relation was first discussed by Schmidt (1959, 1963) and expanded upon by Kennicutt (1989, 1998b). It links the gas surface density to the star formation surface density, via the relation:

$$\Sigma_{SFR} \propto (\Sigma_{gas})^n \qquad \boxed{1.2}$$

An example of the relation is shown in Fig. 1.5. Different choices and assumptions can be made to determine $\Sigma_{SFR}$ and $\Sigma_{gas}$. 'Gas' can mean atomic and/or molecular gas. Atomic gas is traced through the 21 cm line of HI. Molecular gas can be traced through various tracer species. Detections of $H_2$, the most abundant molecule, cannot be used, since it is a symmetric molecule and has no permanent dipole moment. Its first observable transition is at $28\,\mu m$ and usually arises from warm gas with $T > 100\,K$ (e.g. Roussel et al., 2007). The CO line emission is most often the tracer of choice for the cold molecular phase of the ISM, since CO is abundant and easily excited, and its ground transition at 2.6mm lies in a favorable atmospheric window. The 'X-factor' is used to convert the observed CO intensity into total gas mass (X(CO) $\sim$ $2.2 \times 10^{20}\,cm^{-2}\,(K\,km\,s^{-1})^{-1}$ Solomon & Barrett, 1991; Kennicutt, 1998b; Pineda et al., 2010; Kennicutt & Evans, 2012). Also, tracers of dens(er) gas, such as HCN, HCO+ or CS, are used (e.g. Gao & Solomon, 2004; Wu et al., 2010).

To measure the star formation rate various tracers are used (for a recent detailed evaluation of these tracers see Leroy et al., 2012). H$\alpha$ is produced by ionizing radiation from young massive stars, and thus traces star formation in the last 10 Myr. The UV similarly traces young stars, but can also come from less massive A stars with ages of up to 100 Myr. Another option is to trace absorbed starlight in the dust. PAH emission, $24\,\mu m$ emission, or even the full FIR luminosity have been used as a star formation tracer. Free-free radio emission and FIR luminosity show a tight correlation (e.g. Tabatabaei & Berkhuijsen, 2010; Murphy et al., 2011), and thus the former is also used to trace star formation. Combinations of UV/optical and IR tracers are used to complement the strengths of both wavelength ranges.

From Fig. 1.5 it is clear that the KS-relation holds over many orders of magnitude in both gas and star formation surface density. Early work on the KS-law was restricted to global measures per galaxy. Now, the KS-law can also be investigated on (sub-)kpc scales. Bigiel et al. (2008) and Leroy et al. (2008) showed that the KS-law also holds on these scales, with increasing scatter to smaller scales. That is an important realization, because it provides information on the physical processes that underly star formation. The KS-relation as a *global* relation, only implies that star formation is governed by physical processes internal to a galaxy. Now, since the KS-relation also holds on (sub-)kpc scales, the physical processes related to star formation must be internal to these regions. The tight relation at (sub-)kpc scales still suggests that the observations average over several star forming regions. The current state of the field is now to connect the (sub-)kpc KS-relation to the scatter at smaller scales. The actual physics of star formation is contained within that scatter (Feldmann et al., 2011).

The amount of star formation with respect to the gas surface density can also be seen as an efficiency of star formation; i.e. the fraction of some fixed time it takes for gas to be converted into gas (dotted lines in Fig. 1.5). Looking at Fig. 1.5 again, it is
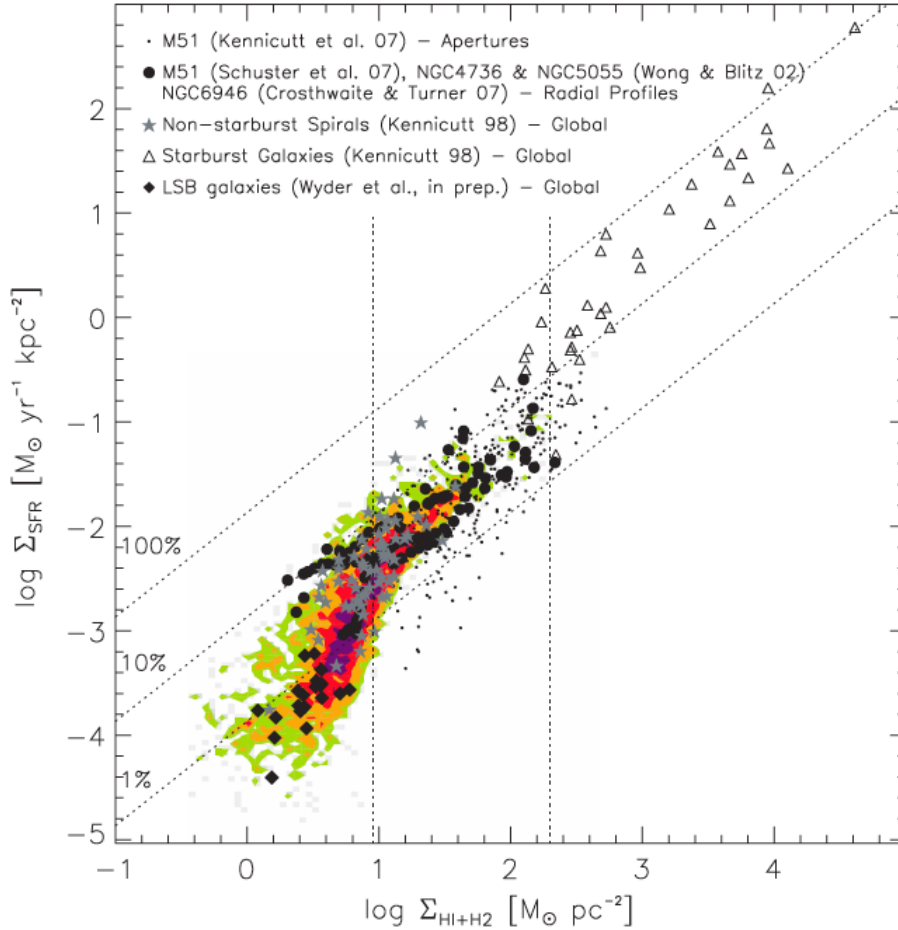
Figure 1.5: Example of the empirical Kennicutt-Schmidt relation, $\Sigma_{SFR} \propto (\Sigma_{gas})^n$. The surface density of the atomic + molecular gas is given on the horizontal axis, the surface density of the star formation rate is on the vertical axis. The data points belong to (sub-)kpc regions (colors and dots) and integrated galaxies (stars, triangles and diamonds). The positive (super-linear) power-law relation between both observables is clear. At a gas surface density of $8 M_\odot \, pc^{-2}$ the power-law breaks. Below this surface density the ISM is dominated by the atomic phase. Thus, star formation is predominantly related to the molecular gas phase. The three dotted lines, marked 1%, 10% and 100%, indicate lines of constant star formation efficiency; the star formation surface density needed to deplete 1%, 10% or 100% of the gas in $10^8$ yr. Figure adapted from Bigiel et al. (2008)
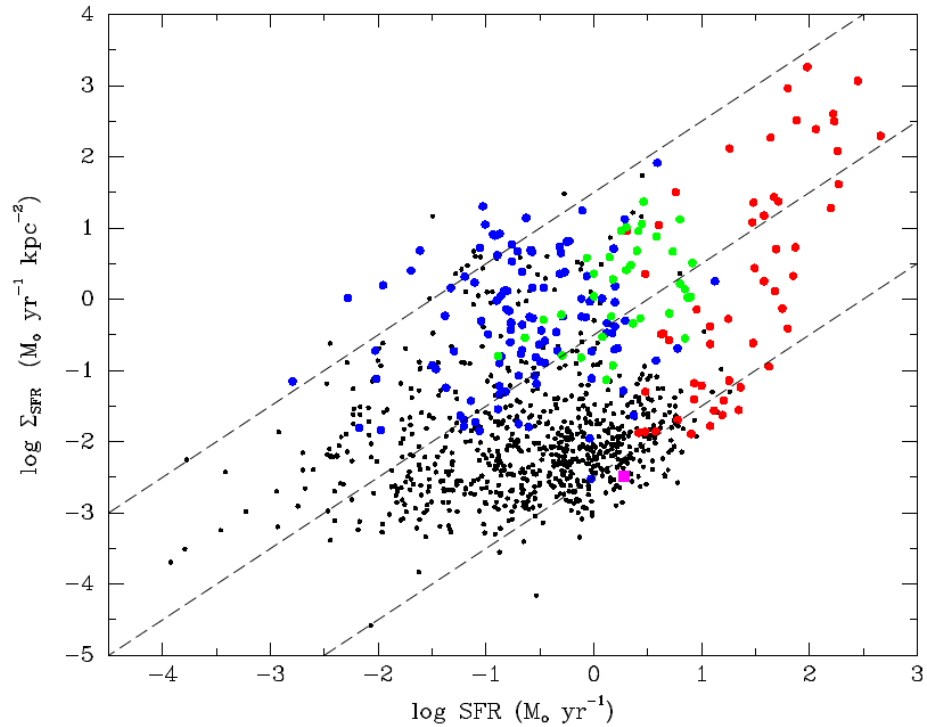
Figure 1.6: Comparison between the star formation rate *surface density* and the star formation rate. Each point is an individual galaxy or starburst region. The three dashed lines show loci of equal star formation area; star formation clustered within 0.1 kpc (top), 1 kpc or 10 kpc (bottom). This figure shows the difference between 'normal' star forming galaxies (black points) and 'starburst' systems, such as (ultra) luminous star formation dominated infrared galaxies (ULIRGS/LIRGS) (red dots), compact starburst galaxies (blue dots) and circumnuclear star forming rings (green dots). 'Starburst' regions produce the same amounts of stars in a smaller area than 'normal' star forming regions. Figure adapted from Kennicutt & Evans (2012)

clear that the time it takes to use up gas by star formation is high. For most galaxies and (sub-)kpc star forming regions the depletion time scale is of the order 1-2 Gyr. There is, however, a subset of galaxies and regions where the depletion time scales are much lower. These galaxies and regions are said to be starbursting. The term 'starburst' was first introduced by Weedman et al. (1981). Kennicutt & Evans (2012) define a starburst as: "a current SFR that is much higher than the long-term average SFR of the system". In other words more stars are formed per unit area than average (Fig. 1.6). The high rates of star formation seen in a starburst cannot be sustained over a long period of time, due to a lack of sufficient gas for fuel.

Of the three categories of starburst region shown in Fig. 1.6, only circumnuclear rings are readily present in the nearby Universe. (Ultra-)luminous infrared galaxies (ULIRGs/LIRGs) and compact starburst galaxies are predominantly found at redshifts z>0.1. Circumnuclear star forming rings are thus special regions in nearby galaxies, also when it comes to star formation (Kormendy & Kennicutt, 2004). Their starburst nature, which can be studied in great detail at these distances, can yield crucial insights relevant for their more distant cousins.

## 1.3 How to observationally study circumnuclear rings

The galaxies that are studied in this thesis where carefully selected to reach the goals set forth at the beginning of this chapter. NGC 5248 and NGC 6951 are similar in many of their global aspects; disk size, mass, metallicity, large scale stellar bar parameters, but their circumnuclear regions are very different. NGC 5248 has two circumnuclear star forming rings, one very close to the quiescent nucleus (r≈100 pc), while NGC 6951 has one circumnuclear star forming ring (r≈600 pc) and a low-luminosity AGN. Both galaxies also have low inclination ($i \sim 43°$), which permits a clear view of the disk. Studying the gas dynamics and stellar content in both these galaxies' circumnuclear regions will give insight why these two, otherwise similar galaxies, have such different circumnuclear regions, and what we can learn from this with regard to nuclear feeding and star formation in high gas density environments.

To reach these goals, I observed both gaseous and stellar tracers. I made the following considerations and choices in the selection of the telescopes and instruments. At a distance of 20 Mpc an angular resolution of $1''$ is equal to $\sim$100 pc. The radius of circumnuclear rings varies between 100 pc and 600 pc for the circumnuclear rings in NGC 5248 (D=12.7 Mpc) and NGC 6951 (D=24.1 Mpc). High, (sub-)arcsecond, resolution observations are therefore necessary to resolve these rings.

The dominant cold neutral gas phase in the centers of galaxies is usually the molecular phase (Sakamoto et al., 1999; Sheth et al., 2005). The most abundant molecular species by far is $H_2$. But, observations of $H_2$ are severely hampered by the fact that $H_2$ does not have a permanent dipole moment, as already mentioned. The CO rotational lines $^{12}CO(1-0)$ and $^{12}CO(2-1)$ are used as tracers, because CO is abundant and is easily excited. For that reason I chose CO observations to trace the molecular gas. These two CO lines emit at 2.6 mm and 1.3 mm, respectively. To reach sufficient spatial resolution with mm receivers an interferometer needs to be used. There are several mm-interferometers in the world sufficient for my use; PdBI, SMA and CARMA on the

northern hemisphere[1] and now also ALMA on the southern hemisphere. I have used the PdBI, since my targets are in the northern hemisphere. PdBI has a better sensitivity compared to CARMA, and observations of both transitions can be made, unlike with SMA.

Radio/mm-interferometers observe visibilities between two detectors and reconstruct the intensity via Fourier transformations. This implies that depending on the length of the distance between each pair of receivers in the array, the resulting data will be sensitive only to spatial scales related to those baselines. That is why most interferometer arrays can be put into multiple configurations. Some observations need larger baselines (to probe smaller spatial scales), other observations need shorter baselines (to observe larger spatial scales). Observations obtained with different array configurations can be combined to increase the spatial sampling[2]. However if only interferometric data are combined, the full flux in the field of view will never be fully recovered. For this reason, additional single dish observations are required. Single dish observations give a measure of the total flux in the FoV, which can be used to scale the interferometric data. Inclusion of single dish data improves detection of low-brightness diffuse emission. For all my CO molecular gas observations, I have included single dish observations from the IRAM 30m telescope.

I use atomic gas data in this thesis, to connect the (central) molecular gas distribution with the gas distribution in the larger disk. HI observations were obtained with the radio-interferometer Very Large Array (VLA) which operates in the cm-regime and are presented in Haan et al. (2008). HI is detected by means of the 21 cm line; when the electron spin flips while HI is in the ground state, a photon is emitted with a wavelength of 21 cm. While this flip does not happen often, the sheer number of hydrogen atoms in a galaxy makes this line very strong.

Two methods are available to observe the stellar content in nearby galaxies. At 20 Mpc distances it is impossible to resolve stellar populations into individual stars. So, either I have to target star clusters or obtain spectra of the integrated light of many stars to study stellar ages. I have obtained data that allows me to do both.

Star clusters have a spatial extent of several pc, equivalent, at a distance of 20 Mpc, to only ~0.05″. This implies that to detect and to be able to separate them from the background the PSF and the pixel scale of the observations cannot far exceed that number. Therefore the Hubble Space Telescope instruments are ideally suited for such work. Indeed, *HST* observes at that resolution because it is not hampered by turbulence in the atmosphere, commonly called "seeing". *HST*'s discrete broad band filters span the near-ultraviolet to near-infrared range, with additional narrow-band filters centered on key Hydrogen lines. Combining the different filters enables me to construct low resolution spectral energy distributions (SEDs), which can be used to characterize the star clusters.

In order to study the 'full' stellar content of a particular region in a nearby galaxy, I turn to integral field spectroscopy. Integral field units (IFUs) record spectra for each 'spaxel' in the detector. A spaxel is a 'spectral-pixel'; each pixel is now a spectrum,

---

[1] At this time the Nobeyama array is no longer being operated.

[2] see for example the following presentation from the 6th IRAM summerschool (2010), http://www.iram.fr/IRAMFR/IS/IS2010/presentations/pety-basics-101004.pdf

instead of a single intensity. IFUs generally cover either optical or near-infrared windows of the spectral range, with (sub)arcsecond size spaxels and a spectral resolution of several Å. The two IFUs whose data is used for this thesis are the SAURON (Bacon et al., 2001) and OASIS (McDermid et al., 2004) instruments. SAURON has spaxels of 0.8″, with a large FoV (42″× 33″), OASIS has spaxels of 0.2″, but has only a small FoV (10.3″× 7.4″) as a trade off. Both are optical IFUs and cover two key stellar absorption lines (H$\beta$ and Mg$\beta$) that vary significantly with stellar age. By means of fitting the observed spectra with combinations of spectra from single stellar population (SSP) libraries, these observations can be used to separate stellar populations of different ages without resolving individual stars.

# 2

# Molecular gas kinematics in the inner 3 kpc of NGC 6951

**Motivation:** In this chapter I present the molecular gas distribution and dynamics of the nearby galaxy NGC 6951. NGC 6951 has a large scale stellar bar that has shaped the gas distribution in the circumnuclear region. The gas in the circumnuclear region is almost exclusively distributed in two gas lanes and a circumnuclear ring at 580 pc radius from the nucleus (near the ILR).

NGC 6951 also hosts an AGN at its nucleus. The goal in this chapter is to determine the gravitational torque distribution in the circumnuclear region and understand how much (if any) gas can flow inward past the circumnuclear ring to be available as possible fuel for the AGN phase.

The circumnuclear region of this galaxy is HI depleted (Haan et al., 2008). All gas in the inner 3 kpc is in the molecular phase. The molecular gas distribution has been studied before using interferometric CO observations (García-Burillo et al., 2005; Haan et al., 2009), but I include for the first time single dish observations, which will finally give the complete gas distribution at these radii.

To determine the gravitational torque at each position and its influence on the gas, I model the observed CO distribution with an analytical large scale stellar bar potential. Primarily, to obtain an independent gravitational torque distribution in the central 3 kpc. I also compare my result against previous more direct observation based methods (García-Burillo et al., 2005; Haan et al., 2009) to measure the gravitational torques, as a mutual test of robustness.

## 2.1 Introduction

Gas accretion onto supermassive black holes (SMBHs) is believed to be the cause of nuclear activity in galaxies. SMBHs are accepted as a common component in most galaxies with a significant massive bulge (e.g. Ferrarese & Ford, 2005, and references therein). However, only about half (43%) of the local galaxies host active galactic nuclei (AGN) in the Seyfert, LINER or transition-object categories (Ho et al., 1997). This discrepancy between the presence of SMBHs and nuclear activity must therefore be sought in the possibility and efficiency of gas transportation to the central regions.

## CHAPTER 2. MOLECULAR GAS KINEMATICS IN THE INNER 3 KPC OF NGC 6951

Gas transport toward the centers of galaxies can only happen when the gas is able to lose its angular momentum. Two categories of dynamical mechanisms can cause inflow. Gravitational mechanisms such as galaxy-galaxy interactions on large scales or non-axisymmetries (i.e. spiral density waves, large-scale stellar bars or nuclear ovals) within the galaxy potential. Both exert gravitational torques. Viscosity torques and shocks caused by turbulence in the interstellar medium (ISM) are a hydrodynamical mechanism for losing angular momentum. When present, gravitational torques are more efficient (e.g. Combes, 2004).

Observations of the inner regions of galaxies are necessary to understand how the interplay of mechanisms results in gas transportation all the way down to the nucleus. The dynamic timescales in the central region of galaxies are short. Therefore, the gas distribution in these regions needs to be mapped with high angular resolution. The NUclei of GAlaxies (NUGA) project (García-Burillo et al., 2003b) has been obtaining high-resolution ($0.5'' - 1''$) detailed mapping of the molecular gas kinematics in 12 nearby ($D = 4 - 40$ Mpc) low luminosity active galactic nuclei (LLAGN) with the IRAM PdBI (Plateau de Bure Interferometer) and 30m telescope. This sample spans the whole sequence of nuclear activity types. In the central kiloparsec most of the gas is in the molecular phase, making CO lines optimal tracers of the gas dynamics. The spatial resolution ($< 100$ pc) of this survey allows one to observe the gaseous distribution over an impressive spatial range. This has already led to the identification of a wide range of morphologies in the nuclear regions of these galaxies, including lopsided disks (NGC 4826: García-Burillo et al. (2003a), NGC 3718: Krips et al. (2005), NGC 5953: Casasola et al. (2010)), bars and spirals (NGC 4569: Boone et al. (2007), NGC 2782: Hunt et al. (2008), NGC 6574: Lindt-Krieg et al. (2008), NGC 4579 García-Burillo et al. (2009)) and rings (NGC 7217: Combes et al. (2004), NGC 3147: Casasola et al. (2008), NGC 1961: Combes et al. (2009)).

Large-scale stellar bars are believed to be efficient in driving gas towards the inner Lindblad resonance (ILR) (i.e. Regan & Teuben, 2004; Sakamoto et al., 1999; Sheth et al., 2005). There they induce the formation of spiral or ring structures (Prendergast, 1983; Athanassoula, 1992a,b; Englmaier & Shlosman, 2000; Maciejewski, 2004b; Combes, 2004). Martini & Pogge (1999) and Regan & Mulchaey (1999) have proposed that spiral shocks induced by the large-scale stellar bar can generate further gas inflow across the ILR. Numerical simulations have shown that spiral structure can extend across the ILR into the nuclear region, if the sound speed is high enough (Englmaier & Shlosman, 2000) or if the velocity dispersion in the ISM is large enough (Maciejewski, 2004b).

Alternatively, other mechanisms on smaller scales could take over gas transportation towards the nucleus, i.e. the bars-within-bars scenario (Shlosman et al., 1989). Viscosity torques can only become the dominant mechanism for inflow in the innermost regions (<200 pc: Combes (2004)).

In this chapter I study the nearby spiral galaxy NGC 6951. Its distance of 24.1 Mpc allows for high spatial resolution ($1'' = 117$ pc). There are several arguments that gas inflow is currently occurring in this galaxy. A large-scale stellar bar has been detected in the near-infrared (Buta et al., 2003; Block et al., 2004) with a bar radius of $26''$ ($\approx 3.0$ kpc) and a position angle of $84°$ (Mulchaey et al., 1997). This galaxy also shows a pronounced starburst (SB) ring at $5''$ (=580 pc) radius in H$\alpha$ (Pérez et al., 2000; Rozas

et al., 2002) and radio (Saikia et al., 2002) emission. Haan et al. (2009) have shown that the inner region of NGC 6951 is HI depleted, implying the ISM must be dominated by its molecular phase. $^{12}$CO(1-0) and $^{12}$CO(2-1) emission associated with the SB ring has been found (Kohno et al., 1999; García-Burillo et al., 2005), as well as HCN(1-0) emission (Krips et al., 2007). NGC 6951 has also been classified as 'a high excitation LINER and a possibly high nitrogen abundant Seyfert 2' galaxy (Pérez et al., 2000). In the central 1″ of NGC 6951 Krips et al. (2007) and García-Burillo et al. (2005) have detected HCN(1-0) and $^{12}$CO(2-1) emission, respectively, indicating that further inflow of gas beyond the SB ring must be or has been occuring recently.

I present $^{12}$CO(1-0) and $^{12}$CO(2-1) observations made with the IRAM PdBI and 30m telescope. Previous papers by García-Burillo et al. (2005) and Haan et al. (2009) presented the PdBI-only data. Here the $^{12}$CO(1-0) and $^{12}$CO(2-1) data cubes have been combined with the 30m observations. The addition of the 30m observations provides the full CO emission present, sampled on all scales in the inner 3 kpc of NGC 6951.

This chapter has three aims. The first is to investigate how the addition of the 30m data changes the maps and the gravitational torque results derived by García-Burillo et al. (2005) and Haan et al. (2009) and to perform a more detailed investigation of the kinematics of the molecular CO gas than has been done before. The second is to quantify the influence of the large-scale stellar bar within the inner 3 kpc using a parametric kinematic model. The third is to study the impact of the nuclear stellar oval on the gas flow inside the circumnuclear gas ring.

In §2.2 I present the observations from the IRAM PdBI and 30m telescope and their reduction. §2.3 contains a discussion of the changes due to the addition of the 30m data and a presentation of the spatial and kinematic properties of the CO emitting gas as seen in the PdBI+30m data cubes. In §2.4 I detail the large-scale stellar bar model, with the results that follow from the model being presented in §2.5. Finally, in §2.6 I compare the result here with previous gravitational torque studies of NGC 6951 and discuss observational evidence for inflow to the nucleus. I summarize in §2.7.

## 2.2 Observations and data reduction

### 2.2.1 IRAM PdBI observations

The IRAM PdBI observations in ABCD configuration were carried out between June 2001 and March 2003 using the 6-antenna array in dual-frequency mode. Only the D-configuration observations were executed with 5 antennas. The correlator was centered at 114.726 GHz and 229.448 GHz at 3mm and 1mm, respectively, corresponding to a heliocentric velocity of 1425 km s$^{-1}$. The bandwidth covered changed between the CD and AB configurations, although all four configurations covered at least the central ±200 km s$^{-1}$. The flux calibration used CRL618, 0932+392, 3C273 and/or 3C345. Bandpass correction was derived from observations of a strong quasar at the beginning of the track. 1928+738 and 2010+723 served as the phase calibrators, allowing for correction of atmospheric effects. Phase corrections derived for the 3mm receiver were applied to the 1mm band resulting in a better phase correction at 1mm. The data were

reduced using standard routines in the GILDAS software package[1].

For both data sets CLEANed data cubes were produced with natural and robust[2] weighting. Cleaning was done down to the $2\sigma$ noise level within a fixed polygonal area that was defined based on the zeroth moment map for all channels with line emission. The r.m.s. noise for these data cubes is listed in Table 2.1.

## 2.2.2   IRAM 30m observation

30 m observations of the central $132''$ by $66''$ were obtained on December 24 and 25, 1997. The 3mm and 1mm receivers were tuned to 114.730 GHz and 229.460 GHz. A bandwidth of about 1200 km/s [600 km/s] was covered by 512 channels with a width of 2.6 km/s [1.6 km/s] at 3mm [1mm]. The spacing between individual grid points was $11''$, i.e. half the size of the 3mm beam. The integration time per scan was usually 4 min, and both polarizations were simultaneously observed for each frequency. Typical system temperatures during the observations were 350 K and 630 K for the 3mm and 1mm receivers. The data reduction was done using the GILDAS/CLASS software package. Each scan was inspected and those few with extremely high system temperatures or other instrumental effects were discarded. The baseline was corrected in the individual spectra by fitting a first order polynomial through channels outside the expected line emission. After this correction all spectra for an individual position were averaged together using a noise weight.

## 2.2.3   Short spacing correction

The 30 m observations were used to compute the short spacing correction (SSC) and recover the large-scale low-level flux. The 30m observations were reprojected to the field center and frequency of the PdBI observations. The bandwidth coverage of the 30m observations was resampled to match the velocity axis of the interferometric observations. A combined data cube was produced using the task 'UV-short' in GILDAS. The single dish weight scaling factor was $6.55\times10^{-3}$ for $^{12}CO$(1-0) and $7.74\times10^{-4}$ for $^{12}CO$(2-1).

Two sets of final CLEANed data cubes were produced using natural and robust weighting. The resolution of the natural [robust] weighted $^{12}CO$(1-0) and $^{12}CO$(2-1) data is given in Table 2.2. The data cubes have 512 x 512 pixels, with a pixel scale of $0.25''$/pixel [$0.10''$/pixel] and velocity bins of 10 [5] km s$^{-1}$ for the $^{12}CO$(1-0) [$^{12}CO$(2-1)] data. The r.m.s. noise per channel in the SSC $^{12}CO$(1-0) observations is 2.5 mJy/beam and 2.2 mJy/beam with natural and robust weighting, respectively. For the SSC $^{12}CO$(2-1) observations these values are both 7.8 mJy/beam. CLEANing was done down to the $2\sigma$ noise level with the assistance of individual polygons defined for each channel with line emission present.

The noise values of the SSC data cubes are, with the exception of the $^{12}CO$(2-1) natural weighted data cube, below the noise levels of the PdBI only data. The beam sizes increase slightly ($\sim 8\%$) due to the added short spacings.

---

[1]http://www.iram.fr/IRAMFR/GILDAS
[2]Robust weighting here means the weighting function $W(u, v)$ in a *uv* cell is set to a constant if the natural weight is larger than a given threshold, and $W = 1$ otherwise.

Table 2.1: Overview of PdBI data

| Emission Line | Weighting | Beam Size (″ x ″) | PA (°) | r.m.s. (mJy/beam) |
|---|---|---|---|---|
| $^{12}CO$(1-0) | natural | 2.56x1.70 | 108 | 2.8 |
| | robust | 1.37x1.08 | 114 | 2.3 |
| $^{12}CO$(2-1) | natural | 1.58x1.37 | 87 | 7.8 |
| | robust | 0.64x0.50 | 111 | 8.0 |

**Notes:** The beam sizes and PAs of the CLEAN beams for the PdBI data. The right most column gives the r.m.s. noise of the CLEANed PdBI-only data cubes. The data cubes are specified according to emission line and weighting.

Table 2.2: Overview of PdBI+30m data

| Emission Line | Weighting | Beam Size (″ x ″) | PA (°) | r.m.s. (mJy/beam) |
|---|---|---|---|---|
| $^{12}CO$(1-0) | natural | 3.11x2.59 | 94 | 2.5 |
| | robust | 1.57x1.22 | 112 | 2.2 |
| $^{12}CO$(2-1) | natural | 1.72x1.56 | 81 | 7.8 |
| | robust | 0.69x0.55 | 113 | 7.8 |

**Notes:** The beam sizes and PAs of the CLEAN beams for SSC (PdBI + 30m) data. The right most column gives the r.m.s. noise of the CLEANed SSC (PdBI + 30m) data cubes. The data cubes are specified according to emission line and weighting.

### 2.2.4 *HST* NICMOS observations

We retrieved from the *HST* archive the NICMOS F110W and F160W images of NGC 6951. The reduction was carried out using the "best" calibration files, and the van der Marel algorithm (e.g. Böker et al., 1999) to reduce the "pedestal" effect. Sky values were assumed to be zero, which is generally a good assumption for these kinds of NICMOS images (Hunt & Malkan, 2004). The images were calibrated, converted to magnitude scale, and subtracted to obtain a [F110W]-[F160W]$\approx J - H$ color map. This color image and the starburst ring it reveals will be discussed in Sect. 2.3.1.

## 2.3 Properties of the CO-emitting gas

### 2.3.1 Morphology and $H_2$ masses

The intensity maps of the CO(1-0) and CO(2-1) observations presented in Fig. 2.1 have been constructed from the CLEANed data cubes using the software GIPSY[3] (Van der Hulst et al., 1992). These zeroth moment maps are computed as the pixel-wise sum of emission above a fixed threshold. Here I chose the $3\sigma$ noise level. Spurious signals are filtered out by imposing the constraint that the emission be above this threshold in at least two consecutive velocity channels. All signals that satisfy these requirements

---

[3]Groningen Image Processing SYstem
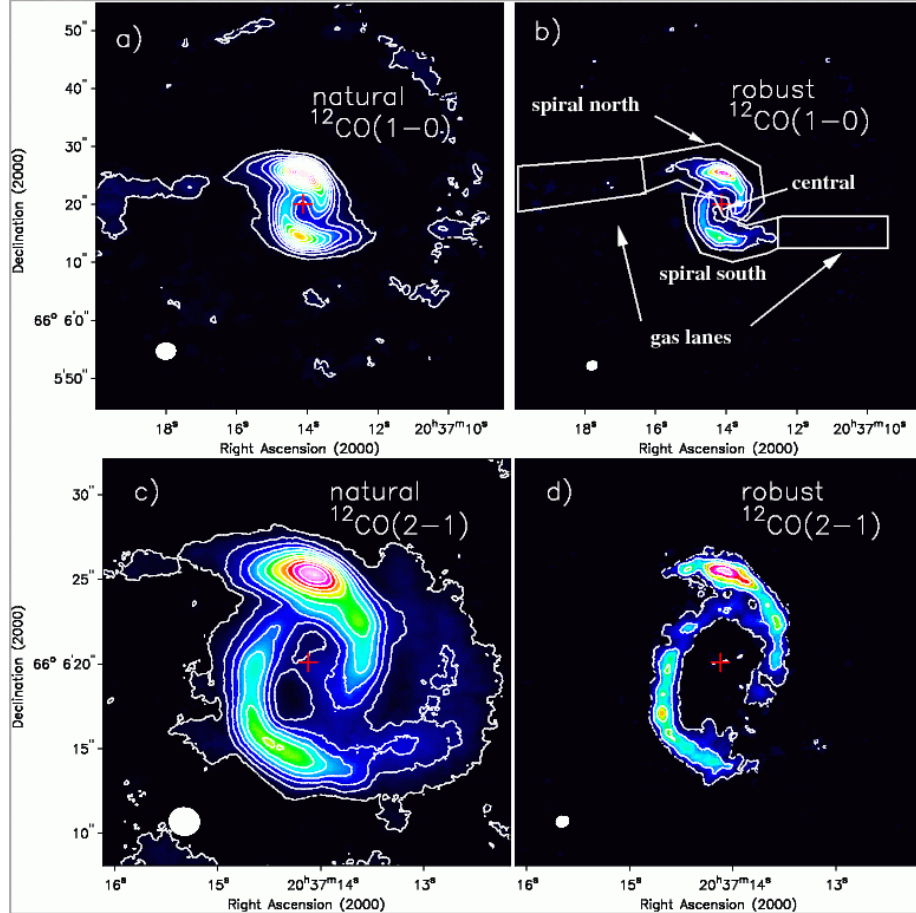
Figure 2.1: *Top:* Integrated $^{12}$CO(1-0) emission in natural (**a**) and robust (**b**) weighting for the SSC data. The zeroth moment maps have been primary beam corrected. The $^{12}$CO(1-0) emission has been integrated from -220 km s$^{-1}$ to 250 km s$^{-1}$. Contours run from $5\sigma$ in steps of $10\sigma$. The r.m.s. value is: **a)** $1\sigma = 0.025$ Jy beam$^{-1}$ km s$^{-1}$ and **b)** $1\sigma = 0.022$ Jy beam$^{-1}$ km s$^{-1}$. *Bottom:* Integrated $^{12}$CO(2-1) emission in natural (**c**) and robust (**d**) weighting for the SSC data. The $^{12}$CO(2-1) emission has been integrated from -200 km s$^{-1}$ to 200 km s$^{-1}$. Contours run from **c)** $5\sigma$ in steps of $20\sigma$, **d)** $3\sigma$ in steps of $10\sigma$. The r.m.s. value is: $1\sigma = 0.039$ Jy beam$^{-1}$ km s$^{-1}$ for both maps. The red cross indicates the position of the dynamical center in all panels (Table 2.3). The beam sizes are shown in the lower left corners and correspond to the values listed in Table 2.2.

Table 2.3: Global properties of NGC 6951

| Parameter | Value | Reference |
|---|---|---|
| Type | SAB(rs)bc | (1) |
| Nuclear Activity | LINER/Seyfert 2 | (2) |
| Dynamical Center (Locus Radio Continuum) | | |
|   RA (J2000) | $20^h37^m14.123^s$ | (3,4) |
|   Dec (J2000) | $66°06'20.09''$ | (3,4) |
| Inclination Angle | 46° | (5) |
| Position Angle | 138° | (5) |
| Adopted Distance | 24.1 Mpc | (6) |

**References**: (1) de Vaucouleurs et al. (1991), (2) Pérez et al. (2000), (3) LEDA, (4) Saikia et al. (2002), (5) Haan et al. (2009), (6) Tully (1988)

Table 2.4: CO line fluxes

| Component | CO(1-0) | | CO(2-1) | |
|---|---|---|---|---|
| | natural | robust | natural | robust |
| | $S_{CO}$ | $S_{CO}$ | $S_{CO}$ | $S_{CO}$ |
| gas lane N | 23.3 | 2.3 | | |
| gas lane S | 10.3 | | | |
| spiral north | 142.4 | 123.9 | 280.3 | 151.8 |
| spiral south | 109.9 | 94.2 | 202.8 | 123.3 |
| central | 10.3 | 6.1 | 22.8 | 0.9 |
| total | 296.2 | 226.5 | 505.9 | 276.0 |

**Notes**: Integrated line fluxes ($S_{CO}$) for different components of the observed CO morphology. CO fluxes are given in Jy km s$^{-1}$.

Table 2.5: $M_{H_2}$ masses

| Component | CO(1-0) | | CO(2-1) | |
|---|---|---|---|---|
| | natural | robust | natural | robust |
| | $M_{H_2}$ | $M_{H_2}$ | $M_{H_2}$ | $M_{H_2}$ |
| gas lane N | 1.6 | 0.15 | | |
| gas lane S | 0.7 | | | |
| spiral north | 9.7 | 8.4 | 3.8 | 2.0 |
| spiral south | 7.5 | 6.4 | 2.7 | 1.6 |
| central | 0.7 | 0.4 | 0.3 | 0.01 |
| total | 20.6 | 15.8 | 6.8 | 3.7 |

**Notes**: H$_2$ masses ($M_{H_2}$) for different components of the observed CO morphology. H$_2$ masses in $10^8$ M$_\odot$. For the CO(2-1) derived masses, we assume $I_{CO(2-1)}/I_{CO(1-0)} = 0.8$.

are added to the intensity map. To the CO(1-0) emission zeroth moment maps I have applied a primary beam correction.

The intensity distribution of the observed CO(1-0) and CO(2-1) emitting gas has all the components we would expect from a gas distribution driven by a large-scale stellar bar. The morphology of the CO(1-0) emission map (Fig. 2.1, *top, left*) from larger radii inward is comprised of the following components. At the edge of our field we see a spatially unresolved resonance ring at a radius of $\sim 30''$ (=3.5 kpc). This is most likely at the location of the ultra harmonic 4:1 resonance inside corotation (e.g. Sakamoto et al., 2000). This ring is connected to straight gas lanes, with an approximately horizontal (east-west) orientation. Their position corresponds well to the orientation of the large-scale stellar bar, which has a position angle of $84°$ (Mulchaey et al., 1997). The gas lanes also coincide with the dust lanes at the leading edges of the stellar bar (Pérez et al., 2000, Fig. 4a of their paper). In the robust weighted map of the CO(1-0) emission (Fig. 2.1, *top, right*), which is more sensitive to emission on smaller scales, the straight gas lanes are no longer detectable. This indicates that the straight gas lanes consist of more diffuse, low intensity gas.

Going further inward, we find the straight gas lanes connect to a 'twin peaks' morphology and a spiral pattern. This was also observed by Kohno et al. (1999). It is likely that the 'twin peaks' are due to the crowding of gas streamlines in a barred potential (Kenney et al., 1992). The orbit crowding leads to a buildup of gas at those locations where orbits change from $x_1$ to $x_2$, i.e. with orientation along the bar major axis changing to orientation along the bar minor axis for elliptical orbits. The peaks inside the spiral arms have a distance of $\sim 6''$ (= 700 pc) from the nucleus. Slightly within that radius ($\sim 5''$, 580 pc) a circumnuclear SB ring has been detected in H$\alpha$ (Pérez et al., 2000; Rozas et al., 2002) and radio emission (Saikia et al., 2002).

The natural and robust weighted intensity CO(2-1) maps (Fig. 2.1, *bottom*) show a distribution very similar to the one seen in the CO(1-0) maps. Some of the differences, however, stem from the smaller field-of-view (FOV) of the CO(2-1) data. The outer ring at the edge of the CO(1-0) FOV is not visible, nor are the straight gas lanes. Due to the higher resolution, the two prominent peaks seen in the CO(1-0) maps now break up into multiple maxima. In the natural weighted map the northern peak is now joined by a second one slightly ($\phi \sim 30°$) offset to the west. The southern spiral structure shows an elongated ridge with a far less distinct center. In the natural weighted CO(2-1) map the peaks and ridge are still unresolved structures.

We start to resolve two tightly wound gas spiral arms, as well as peaks of dense gas within the ring only in the highest resolution robust weighted CO(2-1) maps. In the higher density tracer HCN(1-0) a similar effect is seen (Krips et al., 2007). The peaks found in that high resolution image, although barely resolved, sit almost $90°$ down the spiral arms. This seems to indicate some density gradient in the gas ring, starting at the northern and southern peaks and going downstream. Fig. 2.2 shows the CO(2-1) integrated intensity map as contours superimposed on the NICMOS $J - H$ color map (Sect. 2.2.4). The figure shows that the CO spiral arms coincides nicely with the dust ring seen in the grey $J - H$ color. The extinction, $A_V$, can be derived from this color image assuming a $J - H$ color of ~0.7 for a normal (unreddened) composite stellar population, and $(A_J - A_H)/A_V = 0.092$ (as in Cardelli et al. (1989), with $R_V = 3.1$). The $A_V$'s so derived for the SB ring are quite red, ranging from $\lesssim 1$ to more than 6 in the
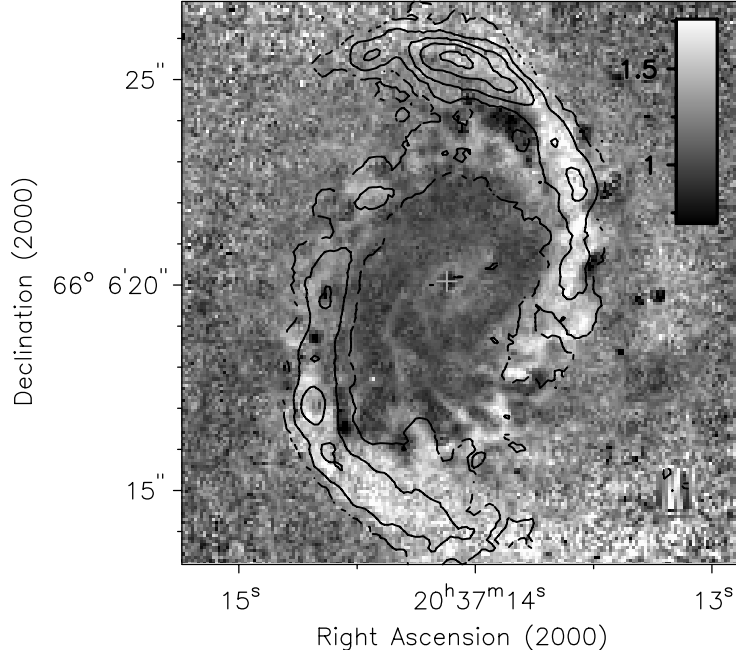
Figure 2.2: $^{12}$CO(2-1) robust weighted intensity map (contours from $3\sigma$ in steps of $10\sigma$ steps, $1\sigma = 0.039$ Jy beam$^{-1}$ km s$^{-1}$); overlayed on a J-H color map (greyscale) from *HST*. The J-H color is a proxy for the amount of extinction/dust. The highest extinction is found in the spiral arms at the intersection with the circumnuclear ring (White corresponds to higher extinction).

dustiest, most compact regions.

Finally, at the dynamical center (Table 2.3) we find barely resolved molecular gas emission (M$\approx 10^6$ M$_\odot$) at the $3\sigma$ level, as already reported by García-Burillo et al. (2005). Central molecular gas emission has also been detected in HCN at a much more prominent level (Krips et al., 2007). The gas bridge between the ring and the nucleus, identified by García-Burillo et al. (2005) as lying at P.A. 134°, is also observed in our data cubes. Here we find the bridge to be present between PAs of 78° and 158°, but the most intense emission is along a PA 113°, as shown in the position-velocity diagram in Fig. 2.3.

The morphology discussed here was for the most part also observed in the previously published PdBI-only maps. The exception is the spatially unresolved resonance ring at the edge of our field, which was not seen at all. The straight gas lanes are more prominent in the SSC maps presented here. The consequences for the gravitational torques will be discussed in Section 2.6.1.

In Tables 2.4 and 2.5 I list the integrated CO line fluxes and the derived H$_2$ masses for the different components described above. The regions over which the flux has been measured are indicated in Fig. 2.1b. These values have been derived with a CO-to-H$_2$ conversion factor X$_{CO}$ of $2.2 \times 10^{20}$ cm$^{-2}$ [K km s$^{-1}$]$^{-1}$ (Solomon & Barrett, 1991) and
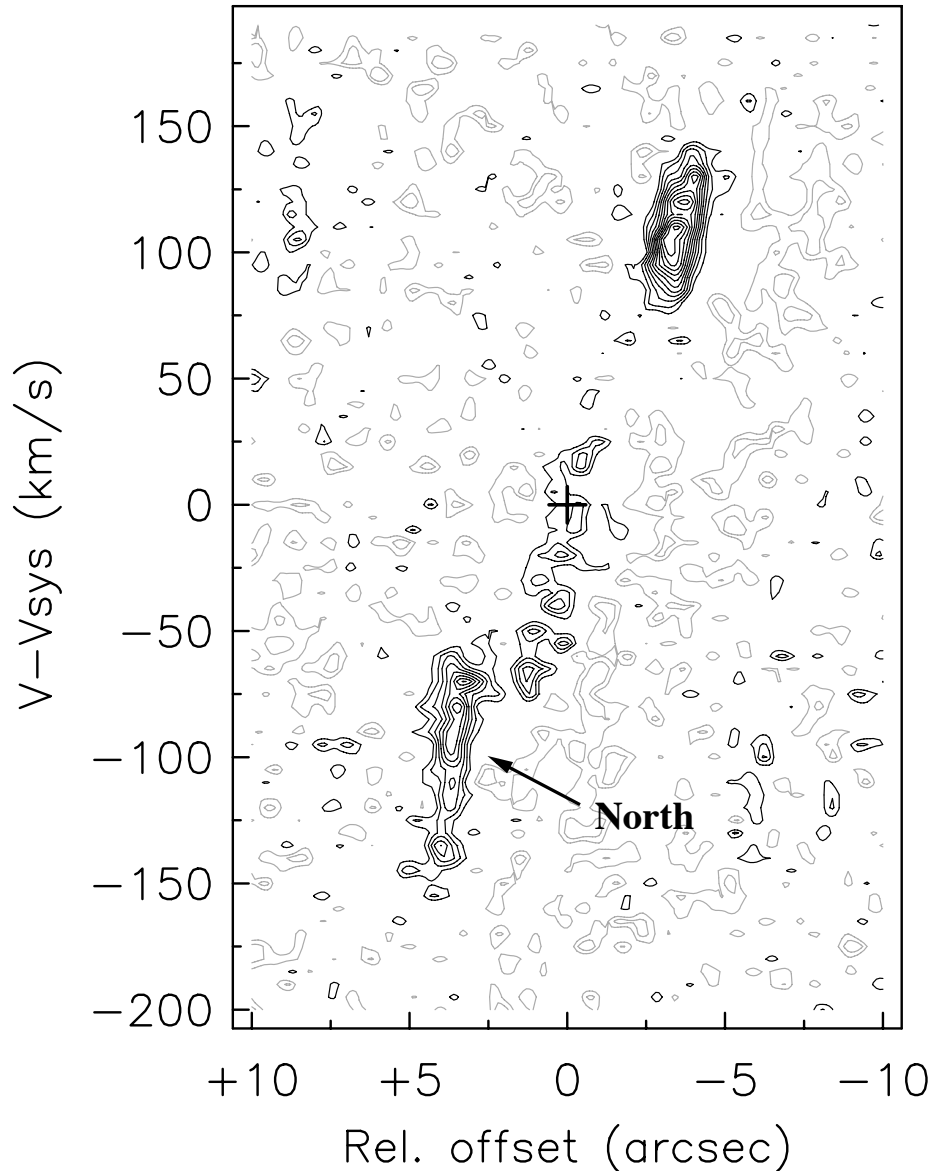
Figure 2.3: Position-velocity diagram along a PA of 113° through the dynamical center. Contours are at $2\sigma$, in $1\sigma$ steps, with the $-2\sigma$ and $-1\sigma$ contours given in grey. A gas bridge is visible between the northern part of the ring (lower left here) and the nucleus (denoted with a cross).
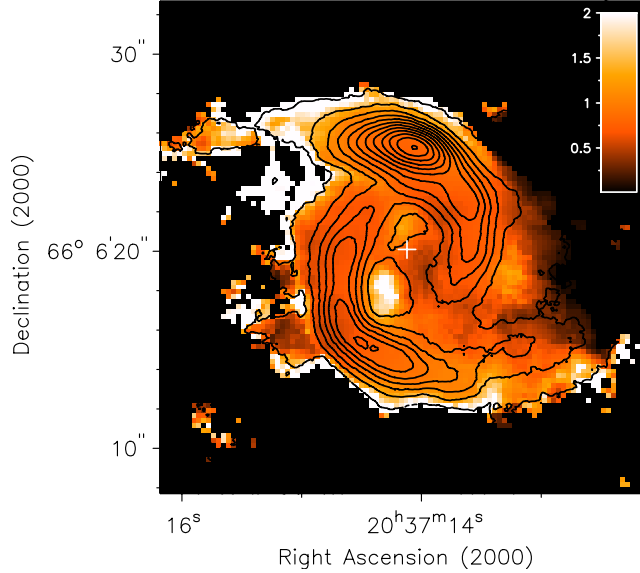
Figure 2.4: Observed emission line ratio CO(2-1)/CO(1-0) map in temperature units. This ratio was computed using the natural weighted CO(2-1) and the robust weighted CO(1-0) data cubes, smoothed to the resolution of the former. The average CO(2-1)/CO(1-0) ratio in the ring is 0.8. The high ratio south-east of the nucleus inside the ring is not significant.

have been corrected for helium abundance (1.36). As the CO line ratio (Sect. 2.3.2) is fairly constant in the center, the assumption of a single conversion factor seems valid for our purpose. There are claims that the CO-to-$H_2$ conversion factor is a factor 3-4 lower in gas-rich centres of spiral galaxies (e.g. Weiß et al., 2001). A lower conversion factor would lower my mass estimates correspondingly. However, for consistency with other papers, I use the Galactic value. The total integrated $^{12}$CO(1-0) flux within a 40″ field of view is 314 ± 55 Jy km s$^{-1}$. The $^{12}$CO(1-0) flux I find, is similar to the measurements of 334 ± 12 Jy km s$^{-1}$ within 65″ by Kohno et al. (1999, obtained with the Nobeyama Millimeter Array and the 45m telescope) and 350 ± 41 Jy km s$^{-1}$ within 45″ by Young et al. (1995, with the FCRAO single dish telescope). The corresponding $H_2$ mass is $2.2 \times 10^9$ M$_\odot$. For the $^{12}$CO(2-1) emission I measure an integrated flux of 452 ± 65 Jy km s$^{-1}$ within a field of view of 14″, which corresponds to an $M_{H_2}$ of $6.3 \times 10^8$ M$_\odot$ if we assume $I_{CO(2-1)}/I_{CO(1-0)} = 0.8$ (see Sect. 2.3.2). As can be seen from Table 2.5 the total measured mass in CO is completely contained in the components mentioned. The areas within which flux is measured are the same for natural and robust weighted maps. In both CO(1-0) and CO(2-1) lines we see that the natural weighted maps are more sensitive to low-level diffuse components of the CO gas. The areas over which the flux of the components has been measured, are marked in Fig. 2.1.

31

## 2.3.2 Line ratio

The CO(2-1)/CO(1-0) line ratio has been used to convert the observed CO(2-1) flux into equivalent CO masses in Section 2.3.1. I have derived the line ratio (Fig. 2.4) in the following manner. Both maps, CO(1-0) and CO(2-1), have been short-spacing corrected and sample down to the same minimum *uv* radius. The robust weighted CO(1-0) data cube was smoothed to the resolution of the CO(2-1) natural weighted cube. Then the zeroth moment map of this smoothed CO(1-0) cube was constructed as before. The CO(2-1) zeroth moment map was regridded to the pixel scale of the CO(1-0) map (from $0.10''$ to $0.25''$). The fluxes of both maps were converted into temperature and the ratio taken.

The ratio is almost constant along the spiral arms, with the map displaying an average ratio of 0.8. The high ratios found at the edges of the ring are insignificant due to low S/N in the CO maps.

## 2.3.3 Kinematics

Evidence of the dominant influence of the large-scale stellar bar is visible in the velocity field. CO(1-0) line emission has been detected in the velocity range of $-220$ km $s^{-1}$ to 250 km $s^{-1}$ relative to the heliocentric velocity of 1425 km $s^{-1}$ in the natural weighted data cube. For the CO(2-1) emission, the velocity range is slightly smaller; from -200 km $s^{-1}$ to 195 km $s^{-1}$. That is in part due to the higher rms noise in this data cube, which affects detection of the signal in the channel maps at the highest relative velocity offsets. All channel maps with significant emission are shown in Figs. 2.5 and 2.6. As the velocity increases, the line emission shifts from the north-west to the south-east. This is consistent with the major kinematic axis of this galaxy, measured by Haan et al. (2009) as 138°using HI data (Table 2.3). The channels close to systemic velocity ($-50$ to 100 km $s^{-1}$) show two maxima, from both sides of the CO ring, as well as extended arms from the bar-driven straight gas lanes.

The CO(1-0) velocity map is shown in the top left panel of Fig. 2.7. The iso-velocity contours in the center are almost perpendicular to the major kinematic axis. As the radius increases the iso-velocity contours bend, forming the 'S'-shape distinctive of velocity fields dominated by large-scale bars.

The dispersion (see the velocity dispersion map in the right panel of Fig. 2.7) reaches values of up to 70 km $s^{-1}$. These values are high for a gas disk and have led me to further investigate the kinematics of the CO. The data cubes show that the observed CO line emission at several positions arises from two distinct components in velocity space, most prominently where the dispersion maps show high values. This complex velocity structure means that we are not seeing a truly high *local* velocity dispersion in a single component, but rather the projection of two velocity components within the same beam. The assumption of a single component when I determine the velocity dispersion is clearly wrong for some positions. We see these double peaks in both CO(1-0) cubes and the natural weighted CO(2-1) cube.

In order to quantify the double emission peaks in detail, I fitted double Gaussians along the spectral axis at each spatial pixel of the CO(2-1) natural weighted data cube (Fig. 2.8). The choice of this cube was made based on the higher spectral resolution of

the (2-1) cube with respect to the CO(1-0) cubes. I used the function 'XGAUFIT' from GIPSY for the fitting. At the spatial pixels where we have a double peak, I separate the two components based on the large-scale bar model I derive in Sect. 2.4.2. In Fig. 2.7 (*middle, left*) I show the central value of the fitted Gaussian for pixels requiring only a single Gaussian fit, and the central value of the Gaussian fit closest to the bar model for the pixels with a double Gaussian fit (component 'V1'). This results in a good representation of the velocity field of the disk of the galaxy. In Fig. 2.7 (*bottom, left*) I present the central values of the second Gaussian (component 'V2'). For the most part, the double peaks are present in the northern spiral arm/ring region, and there is a complex in the south-south-west close to the nucleus. The velocity difference, $\Delta v$, between the two components is between 40 km s$^{-1}$ and 120 km s$^{-1}$.

Most of the two components might be interpreted in terms of the transition from $x_1$ to $x_2$ orbits. $x_1$ orbits are parallel to the large-scale bar (building up the straight gas lanes), and $x_2$ orbits are perpendicular to the bar (supporting the ring). At the resolution of the data cube (beam size 1.72" by 1.56"), the two orbit families might blend together. I find double emission peaks in the CO(1-0) cubes and the natural weighted CO(2-1) cube, where we are unable to resolve the end of the one spiral arm from the other spiral arm. Double velocity components would be the natural consequence of the emission of CO gas on the two orbits families being blended together spatially in the data cubes. In comparison, in the robust weighted CO(2-1) cube I do not find evidence of double peaks in velocity. I find little difference in the width (velocity dispersion) of the Gaussians (Fig. 2.7 *middle/bottom, right*), except in the northern region. There we see a narrower component, connected to 'V1', with a dispersion of about 30 km s$^{-1}$, and a wider component, connected to 'V2', with a value of around 40-50 km s$^{-1}$. This region is where we have the northern peak of the 'twin peaks' morphology, which persists even in the high resolution CO(2-1) intensity map (in the south we see a ridge). The high dispersion here might be explained by the gas being shocked, which leads to more real, local turbulence/dispersion.

The resolution argument does not explain the double emission peaks found inside the spiral arms, south-south-west of the nucleus. In this region, based on the CO(2-1) map, I expect very little emission, let alone emission arising from two distinct ($\Delta v \sim$ 80 km s$^{-1}$) components. The velocity of the first component agrees well with what is expected from the large-scale bar velocity field. The second component's central velocity ($\sim$ 70-90 km s$^{-1}$) seems to connect it with the southeastern part of the ring. There is little difference in dispersion between the two components. The strength of the second Gaussian is nearly equal to the first component. This double emission region is not spatially coincident with the gas bridge mentioned earlier. In Section 2.6.2 I will discuss the significance of both the bridge and this second kinematic component in the nuclear region for nuclear fueling.
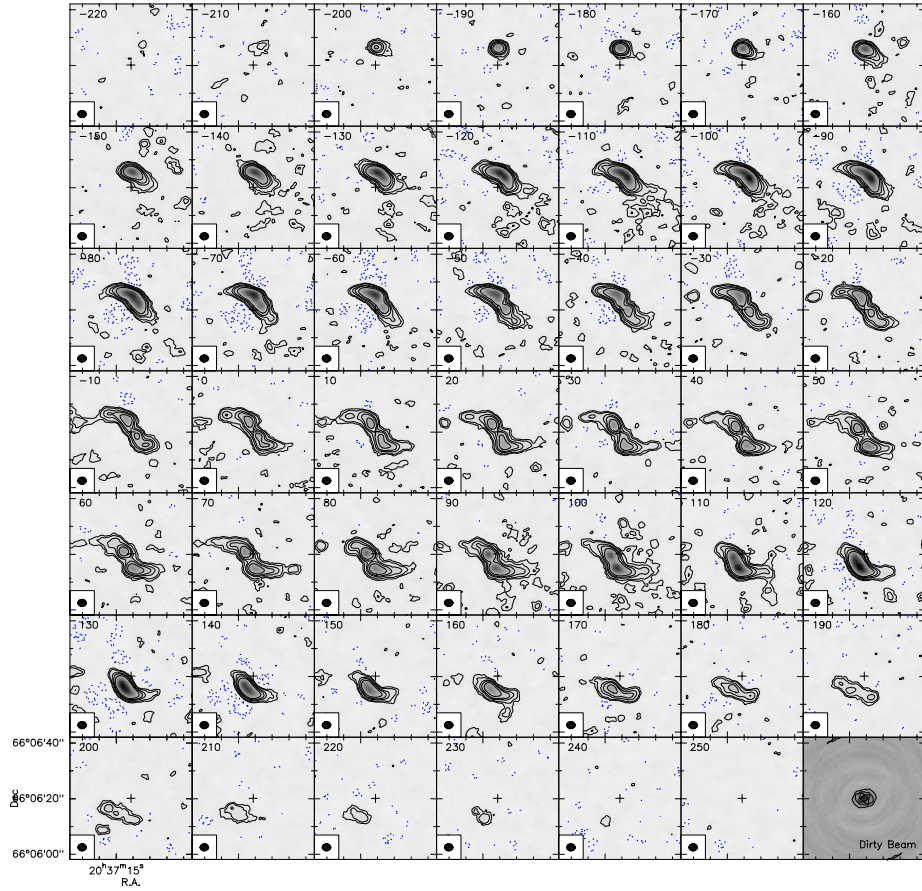
Figure 2.5: Channel maps of the naturally weighted $^{12}$CO(1-0) data cube. The size of each channel map is 44″ by 44″. The contours are at $-3\sigma$, $-2\sigma$, $3\sigma$, $5\sigma$, $10\sigma$, $15\sigma$ and $25\sigma$, with $1\sigma = 2.5$ mJy/beam. The velocity relative to systemic velocity of the galaxy ($v_{sys} = 1425$ km s$^{-1}$) is indicated in the upper left corner. The dynamical center is indicated by a cross in each channel map. The synthesized beam ($3.11″ \times 2.59″$) is given in the lower left corner of each channel and the dirty beam is shown in the lower right panel.
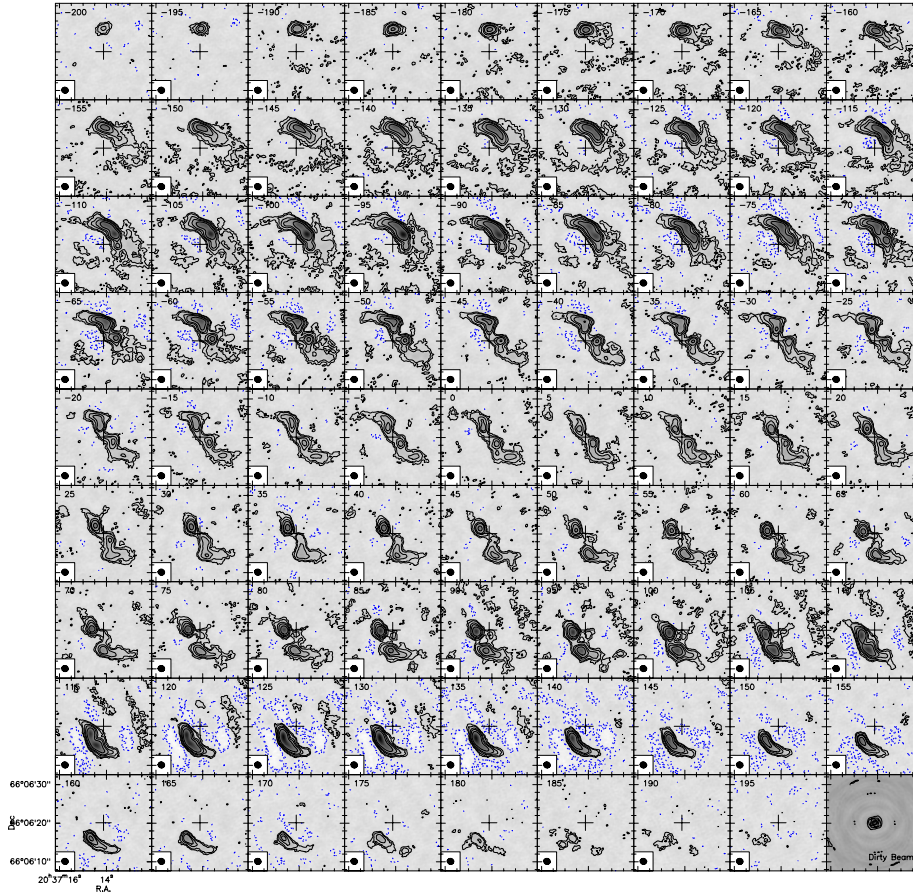
Figure 2.6: Channel maps of the naturally weighted $^{12}$CO(2-1) data cube. The size of each channel map is 25″ by 25″. The contours are at $-3\sigma$, $-2\sigma$, $3\sigma$, $5\sigma$, $10\sigma$, $15\sigma$ and $25\sigma$, with $1\sigma$ = 7.8 mJy/beam. The synthesized beam size is 1.72″ × 1.56″ . All other notation is as in Fig. 2.5.
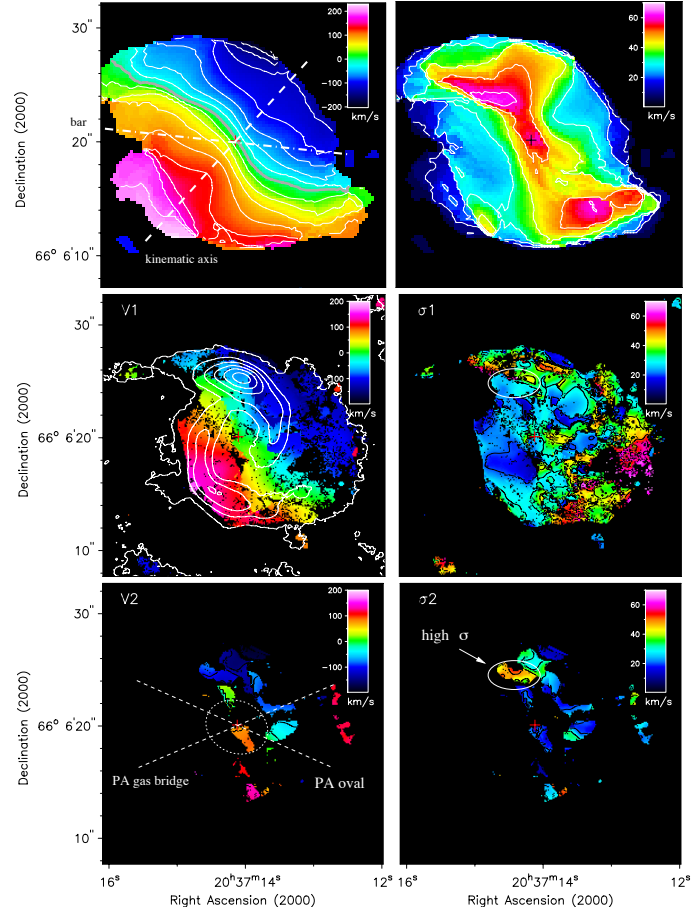
Figure 2.7: *Top left:* First moment map of the CO(1-0) emission. Contours: -200 to 175 km s$^{-1}$ with 25 km s$^{-1}$ steps, 0 km s$^{-1}$ thick gray contour. Kinematic major axis (white dashed line at PA = 138°), orientation of the large-scale bar (dashed-dotted line, PA = 84°). *Top right:* Second moment map of the $^{12}$CO(1-0) emission. Contours: 0 to 70 km s$^{-1}$ in 10 km s$^{-1}$ steps. The dynamical center is marked by a black cross. *Middle/Bottom panels:* Decomposed velocity field of the CO(2-1) natural weighted line emission. Black spots correspond to blanks due to bad fits at some spatial pixels. *Middle left:* The central value of the Gaussian fitted for each spatial pixel. If two Gaussians where fitted, the value of the Gaussian closest to the large-scale bar model velocity is given. The white contours represent the CO(2-1) intensity map ($5\sigma$ in $40\sigma$ steps). *Bottom left:* For the spatial pixels where a double Gaussian was fitted, we plot the central value of that second Gaussian here, i.e. the value further away from the bar model velocity. The size and PA of the nuclear stellar oval and PA of the gasbridge, that will be discussed in Sect. 2.6.2, are highlighted with a white ellipse and dashed lines. *Middle/Bottom right:* Velocity dispersion corresponding to respective velocity components. The dispersion is the Gaussian fitted $\sigma$ at each position. Contours from 0 to 70 km s$^{-1}$. The region with significant differences in velocity dispersion (discussed in Sect. 2.3.3) is highlighted with a white ellipse.

Figure 2.8: Six example spectra from the natural weighted CO(2-1) data cube where we fitted a double Gaussian to the velocity axis. The location of each spectrum is indicated with red lines in the intensity map (middle; same area as Fig. 2.1 bottom, left panel).

## 2.4 Kinematic modeling of the CO observations

### 2.4.1 Motivation

NGC 6951 has a prominent large-scale stellar bar with a radius of 3.0 kpc at a position angle of 84° (Mulchaey et al., 1997). I suggested in Sect. 2.3 that the gas morphology and kinematics in NGC 6951 can be well explained in terms of this barred potential. The spiral pattern and the high intensity twin peak morphology are both consistent with gas streamlines under the influence of a large-scale bar.

To further investigate this claim, I model my CO observations with a gravitational potential where the only non-axisymmetric component is a large-scale bar. This cannot be done from observations directly since this would assume exact prior knowledge of the non-axisymmetric components of the gravitational potential. At the same time this modeling will also allow me to derive gravitational torques in this region for an independent comparison with the gravitational torque results of García-Burillo et al. (2005) and Haan et al. (2009) (Sect. 2.6.1).

### 2.4.2 Description of the model

I modeled the inner 5 kpc (diameter) of the observed CO(1-0) gas distribution and its underlying gravitational potential using the DALIA modeling software (Boone et al., 2006) that was already used to model the NUGA target NGC 4569 by Boone et al.

(2007).

The tool constructs a kinematic model of gas particles in the presence of a barred
potential. The potential is built up from two components, an axisymmetric component
representing the disk, and a weak m=2 perturbation: the 'bar'. The axisymmetric
component has a logarithmic shape and is defined by a characteristic length ($r_p$) and
velocity ($v_p$).

$$\Phi_0(r) = \frac{1}{2}v_p^2 ln(1 + \frac{r^2}{r_p^2})$$

<div align="right">(2.1)</div>

The bar has the same radial profile as the axisymmetric component, but is tapered by
a sine in azimuth and can be oriented in any preferred direction relative to the galaxy's
kinematic major axis (Table 2.6: perturbation azimuth). It is further defined by the
relative amplitude of the perturbation with respect to the axisymmetric component (i.e.
the bar strength, $\epsilon$), and its pattern speed.

$$\Phi_b(r, \phi) = \epsilon\Phi_0 cos(2\phi)$$

<div align="right">(2.2)</div>

The total kinematic model potential can therefore be described as follows:

$$\Phi_{total}(r, \phi) = \Phi_0(r) + \Phi_b(r, \phi) = (1 + \epsilon\cos(2\phi))\Phi_0$$

<div align="right">(2.3)</div>

The model is populated with a distribution of gas particles, described in terms of the
radially varying parameters column density, velocity dispersion and scale height. Two
dissipation terms, one acting radially and one acting azimuthally, are set to reproduce
the dissipative behavior of the gas particles. Finally the model can be inclined and
positioned corresponding to the observations, and a rotation sense is set.

This model has several limitations as discussed by Boone et al. (2007). First, it is
singular at corotation. Buta et al. (2003) and Block et al. (2004) place NGC 6951's
bar radius at 3.0 kpc and indeed, as can be seen from Fig. 2.9 (*top, right*), our model
does not extend to corotation. Second, closed orbits are computed, which are not self-
consistent with the inclusion of two dissipative terms. Therefore, the locations of reso-
nances obtained from this model should be taken as a first-order estimate only.

All parameters in the model can in principle be freely chosen. My interest here is in
obtaining a good set of parameters that reproduces well the observed CO gas distribu-
tion. For this reason, I adopted first guesses for the model parameters based on known
values of the system and subsequently slightly varied them so that the model better fits
our observations. The radial gas mass distribution (Table 2.7) was deduced from the
CO(1-0) emission maps (Fig. 2.1, *top*) and can be scaled with the total observed $H_2$
mass. For the velocity dispersion I take a single value, 30 km s$^{-1}$, which is reasonable
for these radii and the assumption of a pressure supported gas disk (Jogee et al., 2005).
The rotation sense is set to clockwise, as the dust lanes along the bar are assumed to
be leading. The dissipation rates were initially left at default values and only changed
after the other parameters had been fixed. Table 2.6 lists the values of the potential
parameters with which the model best reproduces the observations. The best fit was
estimated by comparing the modeled channel maps (Fig. 2.10) and intensity map (Fig.
2.9 *bottom, left*) against their observed counterparts by eye.

### 2.4.3  Best fit model

Figure 2.9 shows the orbits (*top, left*) and rotation curve (*top, right*) for my best model. The orbit pattern shows the change from $x_1$ to $x_2$ orbits, the main periodic orbits in a bar potential, starting at r=1.5 kpc. The existence of two ILRs, denoted iILR (inner) and oILR (outer) in our model, can be seen from the double intersection of the $\Omega - \frac{\kappa}{2}$ curve with the pattern speed. Corotation is beyond 2.5 kpc, which means the model does not diverge in the range I am studying here.

The presence of two ILRs in NGC 6951 has also been found by both Rozas et al. (2002) and Pérez et al. (2000), who put them at 180 pc and 900 pc, and 180 pc and 1100 pc, respectively. The CO observations cannot be fit by the model without 2 ILRs. Their locations are determined by the free parameters of the model; the pattern speed and the shape of the potential (defined by its characteristic length and velocity). From the resonance diagram in Fig. 2.9 I find the ILRs to be at 160 pc and 1150 pc. These radii are close to the estimates reported by the earlier papers. The orientation of the bar perturbation (130°) in the model is also close to the value for the bar reported by Mulchaey et al. (1997). This degree of consistency shows that the model is a good representation of the observations, and thus I conclude that the CO gas kinematics are indeed dominated by the large-scale stellar bar.

The final model moment maps and channel maps are presented in Figs. 2.9 (*bottom*) and 2.10. The model has been computed at the resolution of the CO(1-0) data. A comparison of Fig. 2.10 with the observations (Fig. 2.5) shows good agreement. The model reproduces the straight gas lanes as well as the two peaks of emission in the ring in the individual channels from $-30$ km s$^{-1}$ to 40 km s$^{-1}$. The channels with emission in the model are only slightly fewer in number than in the observed channel maps. In the integrated emission map of Fig. 2.9 (*bottom, left*), the two spiral arms and the twin peaks are also well reproduced in this model. It is very encouraging that this bar potential model with its simple kinematics and intrinsic limitations fits the observations so well. Therefore, I am confident when I use the model velocity field to separate the two velocity components I detected in the data cubes.

In the channels, -30 km s$^{-1}$ to 40 km s$^{-1}$, the orientation of the two emission peaks is slightly more north-south in the model channel maps than in the observed one. From Fig. 2.7 we already saw that when I decompose the velocity field with two Gaussian fits, the velocity contours of the 'bar'-component also become more north-south oriented.

In Sect. 2.3.1 I reported the location of higher density gas traced by CO(2-1) and HCN further downstream in the spiral arms than what is seen in the CO(1-0) line, which is mainly tracing lower-density gas. High emission peaks in both the CO(2-1) and HCN gas distribution occur away from the 'twin peaks' that dominate the CO(1-0) distribution. I attempted to reproduce this pattern by also computing a best model at the resolution of the CO(2-1) data. The model gas distribution still agrees with the observations in its main characteristics; spiral arms and the twin peaks. However, the details, such as the southern intensity ridge and the second peak in the northern spiral, are no longer well reproduced. I point out that this model therefore reproduces a morphology closer to the CO(1-0) emission than either of the higher gas density maps mentioned above. A plausible explanation could be that the CO(2-1) and HCN

distributions reflect the evolution of the molecular gas inside the circumnuclear ring itself, after the large-scale bar has brought the molecular gas there. As the molecular gas streams within the ring, cloud collapse can occur and/or continue, leading to higher molecular gas densities away from the contact points between ring and gas lanes.

Table 2.6: Bar potential model global parameters

| Parameter | Value | Initial Guess from data |
|---|---|---|
| Inclination (deg) | 46 | 46 |
| Position Angle asc. node (deg) | 318 | 318 |
| Char. Length (pc) [$\mathbf{r}_p$] | 230 | |
| Char. Velocity (km s$^{-1}$) [$\mathbf{v}_p$] | 200 | |
| Perturbation Azimuth (deg) | 130 | 84 |
| Sense of Rotation | Clockwise | Clockwise |
| Bar Strength [$\epsilon$] | −0.035 | |
| Pattern Speed (km s$^{-1}$ kpc$^{-1}$) | 50 | |
| Rad. Diss. Rate (km s$^{-1}$ pc$^{-1}$) | 0.000 | 0.005 |
| Az. Diss. Rate (km s$^{-1}$ pc$^{-1}$) | 0.020 | 0.002 |

**Notes:** The effect of errors in these parameters on our results is discussed at the end of Sect. 2.5.

Table 2.7: Bar potential model radial density parameters

| Radius (pc) | 20 | 450 | 500 | 600 | 700 | 800 | 900 | 1200 | 1500 | 2500 |
|---|---|---|---|---|---|---|---|---|---|---|
| Col. Dens. (rel. scaling) | 0.25 | 0.2 | 0.6 | 0.7 | 0.6 | 0.6 | 0.3 | 0.1 | 0.1 | 0.02 |
| Velocity Disp. (km s$^{-1}$) | 30 | 30 | 30 | 30 | 30 | 30 | 30 | 30 | 30 | 30 |
| Scale Height (pc) | 10 | 10 | 10 | 10 | 10 | 10 | 10 | 10 | 10 | 10 |

## 2.5  Model derived results

The model described in Sect. 2.4.2 can also be used as the basis for a gravitational torque computation. The model's large-scale bar potential is known at each position, since the model is purely analytical. This makes it easy to derive the gravitational torque $\bar{T}(r, \phi)$ on the gas particles at each point, following the equation from Boone et al. (2007):

$$\bar{T}(r, \phi) = -\epsilon\, v_p^2 ln(1 + \frac{r^2}{r_p^2}) sin(2\phi) \tag{2.4}$$

Here $\epsilon$ is the bar strength, $v_p$ the characteristic velocity and $r_p$ the characteristic length as set in the model. $\phi$ is the azimuthal angle with respect to the bar position angle.

Since the orbits for the gas particles are known, I define the net torque at a given radius as the time-average integrated torque over the orbit with this characteristic radius. We recall that the characteristic radius of an orbit is the radius this orbit would have without a bar (the orbit would then be circular). As mentioned in Sect. 2.4.2, this

Figure 2.9: *Top, left*: Deprojected orbit pattern in the inner 3.0 kpc of the bar model. *Top, right*: Resonance diagram showing the rotation frequency $\Omega$ (red), $\Omega - \frac{\kappa}{2}$ (blue), $\Omega + \frac{\kappa}{2}$ (cyan) and the bar pattern speed (yellow dashed). The iILR at 160 pc, oILR at 1150 pc and CR at 4000 pc (outside the displayed range) are indicated with black dots. Overlayed is the rotation curve, which approaches 200 km s$^{-1}$. The vertical dashed line indicates the outer edge of the models radial mass distribution. *Bottom, left*: Integrated emission of the bar model with contours of CO(1-0) intensity map overlaid. The model emission has been computed at the CO(1-0) resolution. Contours run from $5\sigma$ in steps of $20\sigma$ ($1\sigma = 0.025$ Jy beam$^{-1}$ km s$^{-1}$). The red cross indicates the position of the center. *Bottom, right*: Velocity field of the bar potential model with contours of the CO(1-0) velocity field. Contours run from -200 to 200 km s$^{-1}$ in 25 km s$^{-1}$ steps.

approach is not completely self-consistent because when there is angular momentum change the orbits cannot be perfectly closed. Therefore, the gravitational torques computed here should be considered as a first-order approximation to the case in which the orbits are nearly closed. This is a valid approximation if the angular momentum loss is small. Using the simple argument that $\frac{dL}{L}$ is of order $\frac{T}{v^2}$, where $v$ is the characteristic velocity of the potential v=200 km s$^{-1}$, we can see that the relative amplitude of the angular momentum loss per orbit is of order $\sim 0.0125 - 0.05$. Therefore, it takes at least 20 orbital times for the gas to fully lose its angular momentum.

Figure 2.11 (*left*) shows the net gravity torque for each orbit in the model. On the horizontal axis I plot the characteristic radius of each orbit. The net gravity torque is negative over the entire radial range studied here. From 1.9 kpc down to 1.0 kpc the torque stays somewhat constant at values of $-2000$(km/s)$^2$. There is a slight upturn at larger radii. This is the region of the straight gas lanes. The large value indicates that the bar is easily able to transport gas inward to the gas spiral arms. The torques then increase at an almost constant rate down to a radius of 400 pc. We can understand this from Fig. 2.9 (*top, left*): the orbit position angle with respect to the bar stays almost constant (at its maximum value) and the orbit elongation decreases with decreasing radius. A second, smaller, minimum is present at r=150 pc, at the iILR. The net gravity torque becomes zero within the 50 pc radius. A close inspection at the model orbits in the inner 300 pc shows that the orbit orientation changes again from $x_2$ to $x_1$.

The mass accumulation rate that I can calculate from the gravitational torques also depends, in contrast to the gravitational torque per se, no longer solely on the analytical potential, but also on the radial gas mass distribution in the model. Fig. 2.11 (*right*) shows the mass accumulation rate for this model. The variation in the mass accumulation rate indicates that gas must accumulate on some orbits and be depleted from others. That the gravitational torques drive the gas inward is also evident from this curve. At radii larger than 800 pc gas is being depleted and the accumulation rate is negative. These are the radii where the gas is located in the straight gas lanes. From 400 pc to 800 pc radius, the accumulation rate becomes positive. These are the radii at which we find the gas spiral arms and the gas ring, which are separated into two peaks in the figure. In the radius range 400-1000 pc we already saw from the torque plot that the torques decrease with decreasing radius. As the radius decreases the torques are less strong, so less gas is being moved inwards at each radial bin and the gas can accumulate. Inside 400 pc we see a sharp positive peak, at 150 pc. This is the radius at which we found a local minimum in the gravitational torques. The feature is confined to only a very limited radial range, but indicates that some accumulation may still happening inside the ring.

Mass accumulation within 1.5 kpc in radius, i.e. integrated over this radial range, is occurring at a rate of $\sim$+2.0 M$_\odot$yr$^{-1}$ and mostly in the two spiral arms. From the observations I know that the total amount of molecular gas within this radius is about $2.2\times10^9 M_\odot$. Therefore, at the derived accumulation rate, all matter in the spiral arms must have been brought there within the last 1.1 Gyr. However this is a lower limit to the age of the ring, since it assumes that no gas has been turned into stars and that there is always enough gas available at larger radii to be driven inward.

Errors in the gravitational torque computation can come from six model parame-

ters; the characteristic length and velocity of the potential, the bar pattern speed, the bar strength and the dissipation factors. The first three influence the locations of the resonances as well as the values of the net gravity torques. A 10% difference in either of these parameters can cause up to a ~20% difference in the locations of the gravitational torque minima. The change in value is 5% for the characteristic length and 20% for the characteristic velocity and pattern speed. The net gravity torque scales linearly with bar strength. The dissipation factors only influence the strength of the gravitational torques. A 10% difference in these factors leads to a decrease of $\approx 25\%$ in the net gravity torques. However, such changes to the model parameters lead to significantly worse models. Therefore, the uncertainties in the results I derive here for the net gravity torque and the mass accumulation rate are within the relative errors given here.
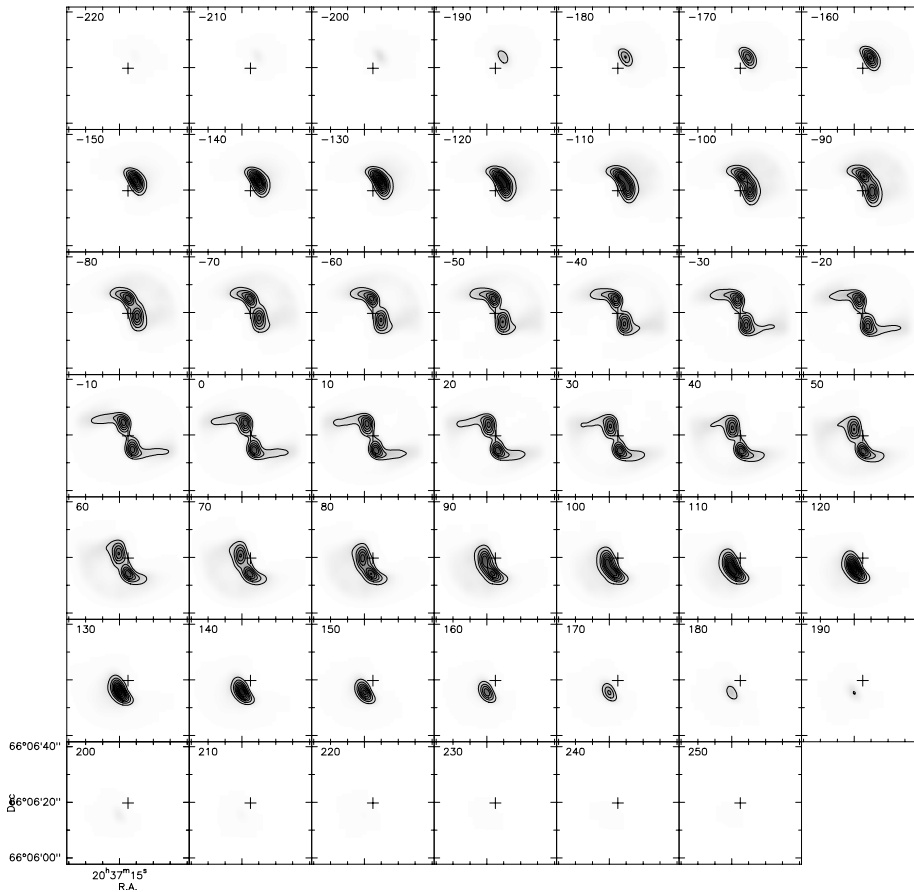


Figure 2.10: Channel maps of our best model fit at the resolution of the CO(1-0) data. The FOV of each channel map is 44″ by 44″. The velocity indicated in the upper left corner is relative to the central channel (0 km s$^{-1}$).
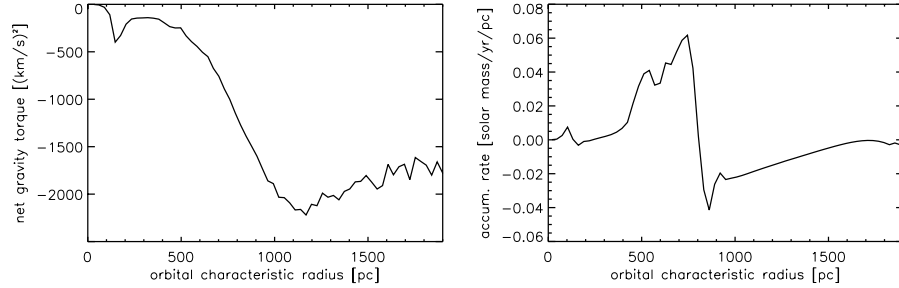
Figure 2.11: *Left*: Net gravity torque derived from the best fit model. *Right*: Gas accumulation rate as a function of radius. The orbital characteristic radius corresponds to the radius of circular orbits that a given gas particle would maintain if unperturbed by the model's large-scale bar.

## 2.6   Discussion

### 2.6.1   Gravitational torques

I can now compare different gravitational torque measurements I obtain using either the 'torque map' method introduced by García-Burillo et al. (2005, ; hereafter: GB05) (see also Haan et al., 2009, ; hereafter: H09), and the analytical computation possible for the large-scale bar model following Boone et al. (2007).

First, I investigate how the inclusion of the 30m data changes the results obtained with the 'torque map' method. Using the code PyPot of H09 we have derived the gravitational torques for the PdBI+30m data cube. PyPot uses NIR high-resolution images to evaluate the stellar potential. The gravitational torque curves for PdBI-only (*dashed line*) and PdBI+30m (*solid line*) data are shown in Fig. 2.12. As can be seen from the figure, the inclusion of the 30m data leads to a change in the gravitational torque budget, especially in the region inside 500 pc. The high positive torques derived at 400 pc in the PdBI-only maps disappear in the PdBI+30m result. This can be explained by the larger amount of diffuse molecular gas that is recovered in the PdBI+30m data, which lowers the high torque barrier at ~200 pc found by GB05 (see their Fig. 12) and H09. The spiral arms become more prominent with the inclusion of the 30m data, so they contribute more to the torque budget at larger radii, shifting the minimum to larger radii. This test shows that sampling the line emission on all spatial scales is important when computing gravitational torques from observations as the absolute values can vary significantly while the overall shape is preserved.

Now, I turn to the comparison of the 'torque map' result with the analytical computation. I am interested in the torques as I want to compute the angular momentum change in the gas (whether the gas is in- or outflowing). In the analytical case, we can simply integrate the net torque over gas orbits from the bar model potential (which is a simplification of the true underlying potential). This integration gives the angular momentum loss of a gas particle in one orbit. In the case of 'torque maps' it is often

argued that it is impossible to know the exact orbits from observations. So, a statistical argument is used in the 'torque map' method. The assumption is that the observed gas distribution can be linked to the time spent by the gas along the orbits. The resulting torque is the gas column density weighted average of the local torques averaged per radial bin.
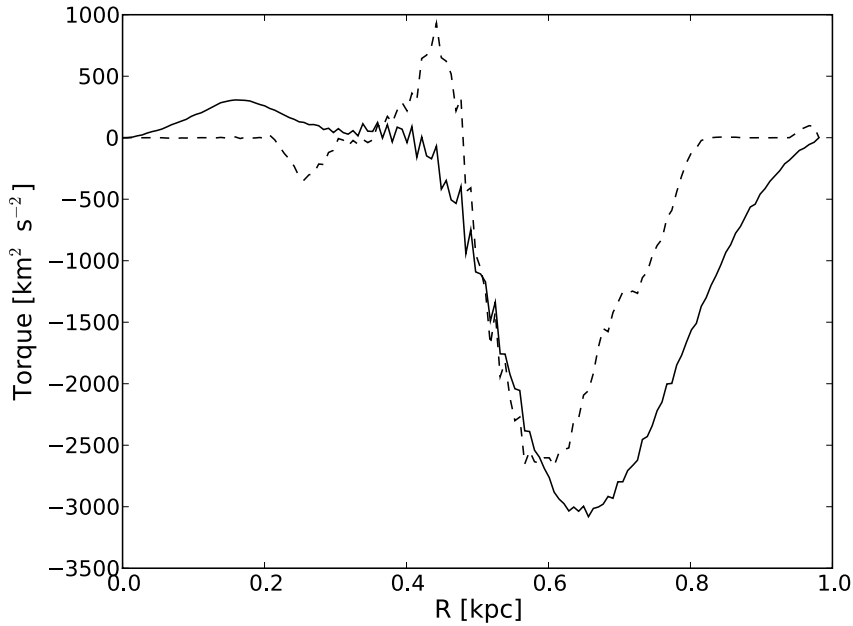


Figure 2.12: Gravitational torque curve derived from the PdBI-only data ((*dashed line*) reproduced from Haan et al. (2009)). Gravitational torque curve derived from the PdBI+30m data (*solid line*) using the same method. The addition of the 30m data has a large influence on the torque values, especially inside 500 pc.

There seem to be significant differences between the results form both methods. In the 'torque map' result I find the strongest (negative) torques at a radius of ~650 pc. For the analytical computation the most negative torques are approximately at a radius of r~1200 pc. As we saw from the intensity maps (Fig. 2.1), we observe very little gas in the straight gas lanes (r$\gtrsim$1.0 kpc). I know, however, that the large-scale stellar bar has a radius of 3.0 kpc (Mulchaey et al., 1997). At 1 kpc the large-scale bar still exerts significant torques on the gas, but the 'torque map' method being very sensitive to the actual observed gas distribution would not show that since there is so little gas, hence the earlier upturn. There is also a difference in the absolute values of the strongest negative torques between the 'torque map' method and the analytical computation. This inequality is due to the difference between computing the net torque (model) and averaging the torques (maps).

In the inner 300 pc, another difference is seen between the 'torque map' method and the analytic computation. In my analytical computation we see a second small dip in the torques, while in the 'torque map' result we find positive torques. By construction, it is impossible in my model for the torques to change sign. Further, GB05 have found that there is a secondary gravitational component, a nuclear stellar oval, that plays a role in the torque budget here. No such secondary component has been included in our model.

Despite these differences, the comparison between my mass accumulation rate in Fig. 2.11 and the mass accumulation rate found by H09 (see their Fig. 12) shows little difference. I find values not more than a factor 2 larger than theirs. This agreement shows that the large-scale bar potential model and the subsequent analytical computation give a good representation of the true gas transportation in this region, at least from the outer disk down to the circumnuclear ring.

### 2.6.2   CO gas flow inside the ring

Another aim of this chapter is to see if a large-scale bar can explain the gas distribution and kinematics over the entire 1.5 kpc radial range. For all radii down to the ring the model represents the observations very well. Inside the ring we found negative torques in the model, but positive torques based on H09's 'torque map' method. Does the influence of the large-scale stellar bar extend further in? As a first test I looked for evidence of gas spiral arms inside the ring, as predicted by the model of Englmaier & Shlosman (2000) and Maciejewski (2004b). In Fig. 2.2 we see some indication of spiral structure in the dust. In the observed CO morphology we do not, nor do we find such evidence when I decompose the velocity field (Fathi et al., 2005; Van de Ven & Fathi, 2010). The latter method is sensitive to even a small arm/inter-arm density contrast. Based on this outcome, it seems that the CO gas is mainly on stable orbits in this region, which implies that it is not inflowing. However, I did find other evidence of CO gas that is potentially not on stable $x_2$ orbits; the gas-bridge and the double CO emission peaks in the line profiles (Figs. 2.3 and 2.7, Sect. 2.3.3).

The primary component of the double peak emission inside the ring (Fig. 2.7, middle right) shows velocities indicative of stable orbits. The line-of-sight velocity of the 'second peak' CO component (located within the white ellipse in the bottom right panel of Fig. 2.7) is 70-90 km s$^{-1}$, which corresponds to a velocity difference from the primary CO component at these coordinates of $\Delta v \sim 80$ km s$^{-1}$. It is unlikely that we have a simple superposition of two gas clouds, both on stable orbits. After separating the flux in this area into the two velocity components, I derive an H$_2$ mass for this 'second peak' CO component of $2.4 \times 10^6 M_\odot$.

To understand if this CO component might still be related to gas spiral arms induced by the large-scale bar, the gas flow direction of the 'second peak' component and whether it is located in the disk of the galaxy must be ascertained. The first issue is straightforward. As Storchi-Bergmann et al. (2007) have concluded the near side of the galaxy is to the southwest and the far side to the northeast. Thus, the positive velocity of this CO component, which is south-south-west of the nucleus, indicates streaming toward the nucleus if the component is in or in front of the disk, and outflow if it is behind the disk. Outflows are usually biconical. If this component is part of an out-

flow, seen behind the disk, we would expect to see a second blue-shifted component from the outflow in front of the disk, which is not the case. Nor do we really expect an outflow, since this galaxy does not have a strong AGN or starburst near its nucleus. It is thus unlikely that this CO component is located behind the disk and outflowing.

If the component is inflowing, it is very unlikely that it has any significant scale height above the disk. NGC 6951 is an isolated galaxy that has been dynamically undisturbed for at least 1 Gyr. This history means that the origin of the CO component has to be internal. It could be that some intense star formation in the ring expelled CO from the ring. We do see a gap in the CO ring close to the component. However, the low velocity dispersion of the CO gas in the component makes it unlikely that the CO component was heated due to star formation, became unbound and was pushed high above the disk and is now falling back. Nor do we see evidence of a recent star forming event at that location.

Thus, it seems most likely that the CO component is inflowing and located in the disk, bringing us back to the question of whether the component's motion can be explained by large-scale bar induced gas spiral arms, even though our initial tests were negative. Storchi-Bergmann et al. (2007) claim to see evidence of two such spiral arms in Hα line emission. The location of their Hα spiral arms does not match the location of our CO component however. Their derived velocity of ± 20 km s$^{-1}$ is also at least a factor 3 smaller than that of this CO component. If there are really gas spiral arms in NGC 6951, this discrepancy is very unexpected. CO should be a better tracer of such gas spiral arms, since it is the dominant gas tracer in this region. So it seems that the large-scale bar does not induce further gas inflow in this galaxy and that this CO component is inflowing due to some other reason.

The CO component might be connected to the stellar oval found by García-Burillo et al. (2005) inside the circumnuclear ring. The position angle of this oval is ~ 66°. Unlike the Hα spiral arms, its orientation matches well with the location of the CO component. If I draw a line through the dynamical center with the oval's PA, the CO component lies almost completely at the southern leading side of the oval (Fig. 2.7, *bottom left*). A stellar oval is in essence a 'fat' bar and can drive gas inward similar to the large-scale stellar bar on larger scales (i.e. the bars-within-bars scenario). The location of the CO component with respect to the oval is correct for this scenario, although we cannot conclude inflow from our gravitational torque results. The reason why the influence of the stellar oval is not more prominent in the gas might be that its bar strength and thus the torque it exerts on the gas is low (García-Burillo et al., 2005, ; their Fig. 8b) and the amount of gas reaching the influence radius of the oval is limited by the circumnuclear ring and its associated star formation. The CO gas we detected in the gas bridge lies in the region where it would feel positive torques due to the nuclear oval; in the averaged torque budget, as shown in Fig. 2.12 this gas can dominate and mask the smaller amount of inflowing gas at these radii. Alternatively, viscosity torques may play a more significant role here, as was also dicussed by García-Burillo et al. (2005).

This CO component could be one of the last links in the chain of gas inflow down to the center. The large-scale bar drives most gas down to the ring. Based on the gravitational torques, this is not the smallest possible radius– only the mass accumulation rate becomes small. So, it is possible for gas to move further in, reach the sphere of influ-

ence of the stellar oval or experience viscosity torques, which brings it further toward
the nucleus. The CO component we observe does not completely reach the dynamical
center. However, spatially and kinematically, it connects to the central HCN detection
of Krips et al. (2007). The HCN extends over ~0.5″ around the dynamical center, and
our CO component extends to about this radius from the center. The detected HCN
also has a detected velocity range of ± 70 km s$^{-1}$, with the positive side where the CO
component is, which also has a velocity of 70 km s$^{-1}$. This concentration potentially
completes the chain of gas inflow.

## 2.7  Summary

I have presented high-resolution $^{12}$CO(1-0) and $^{12}$CO(2-1) maps of the central region of
NGC 6951 using the IRAM PdBI and 30m telescopes. This galaxy exhibits significant
indirect evidence for recent gas inflow. It has a large-scale bar, a circumnuclear SB
ring, and an AGN. Molecular gas, as traced by CO, is the dominant phase of the ISM
in these regions.

Investigation of the CO data cubes shows that the gas distribution can be well ex-
plained by gas response to a large-scale stellar bar. I further quantify this scenario by
reproducing the observations using a model where the gas is solely responding to a
large-scale stellar bar. The model used here has the advantage that it provides direct
predictions for the radial motions of the gas. My best model is able to reproduce the
main characteristics of the observed CO morphology and kinematics.

Gravity torques and gas mass accumulation rates that follow from this model were
computed and compared to previous gravity torque maps by García-Burillo et al. (2005)
and Haan et al. (2009). Their method is complementary to the one used here and I
explain the differences between the two results. As expected, I find that the large-
scale bar effectively transports gas inward to r~400 pc, but it no longer dominates the
gravitational torque budget on smaller radii.

The stellar oval reported by García-Burillo et al. (2005) is a likely candidate to
take over gas transport inside the circumnuclear ring. Detailed investigation of the data
cubes revealed double-peaked CO profiles at several positions inside the gas ring. Most
notably, I detect a second CO complex near the dynamical center, with a velocity offset
of $\Delta v \sim 80$ km s$^{-1}$, which is not on a stable orbit. From simple geometric and physical
arguments, I conclude that this cloud is in the disk of the galaxy, is inflowing toward
the nucleus, is likely driven by the stellar oval, and is indeed the last step in bringing
gas close to the nucleus.

# 3

# How does star formation proceed in the circumnuclear ring of 6951?

**Motivation:** In the previous chapter I studied the gas (flow) in the central 3 kpc in NGC 6951, and confirmed that the circumnuclear ring is an effective barrier against inflow. To understand the true effectiveness of the circumnuclear ring as a gas barrier, I need to determine the age and expected life time of the ring. In chapter 2 I determined that the current rate of inflow of molecular gas onto the ring was $2M_\odot$/yr. The inflow rate in combination with the gas mass currently in the ring already gave an estimate for the minimum age of the circumnuclear ring of 1.1 Gyr.

In this chapter I explore the star formation and stellar ages in the ring. By understanding the stellar ages and the star formation history in the ring I can test the assumptions on inflow rate and available gas mass that led to the minimum age for the ring of 1.1 Gyr. At the same time I can also estimate the projected life time of the ring.

As a second goal in this chapter, I test which of two star formation scenarios proposed in the literature describes best the manner in which star formation proceeds in circumnuclear star forming rings. These two scenarios predict very different spatial age distributions of the stellar populations in the ring. Understanding which one holds true, provides further clues to the age of the ring and the time scales that are required before inflowing gas starts forming stars.

## 3.1 Introduction

Secular evolution comprises all agents of change in a galaxy that are independent of the external environment of the galaxy. Secular evolution, unlike hierarchical clustering and mergers, takes place over long timescales, near-equal to the lifetime of galaxies, and is important for a galaxy's evolution in the current epoch. A large part of secular evolution takes place due to asymmetries in the gravitational potential of a galaxy. All asymmetries assist in the inward and outward motion of gas across parts of the disk. One of the asymmetries that acts the fastest and most severely is a large scale bar: an elongated concentration of stars and/or gas centered on the nucleus, usually of several kpc size. Depending on the strength of the bar, the sound speed in the gas, and the central mass concentration, a circumnuclear ring will form near the inner Lindblad

resonance at a radius defined by the bar (e.g. Athanassoula, 1992a; Regan & Teuben, 2003; Mazzuca et al., 2008; Kim et al., 2012).

A ring directly hinders further inflow towards the nucleus, i.e. nuclear feeding (e.g. Maciejewski, 2004b; García-Burillo et al., 2005). A circumnuclear ring is in effect the gas reservoir for the gas moving inward. Determination of the life times of circumnuclear rings is therefore of paramount importance to understand the influence they have on the evolution of their host galaxies. The high gas densities reached in circumnuclear rings naturally lead to star formation. The ages of the stellar population(s) in circumnuclear rings may be a good indicator of the overall age of the ring, and thus the stellar bar itself. A caveat naturally follows; how does star formation proceed in circumnuclear rings? Is there a time scale that can be related to the onset of star formation in the ring (and that should be added to determine the ring's age)?

Much theoretical and modeling work has been done on the formation of circumnuclear rings (e.g. Athanassoula, 1992b; Englmaier & Shlosman, 2000; Maciejewski, 2004b). Circumnuclear gas rings are closely related to the more generic nuclear spirals; asymmetries in the gravitational potential induce a wave perturbation in the gas. All gas has angular momentum and it needs to lose this momentum before it can move towards the center. This loss is what happens in the dust lanes and nuclear spirals.They are the locations where gas is shocked and loses angular momentum, allowing gas to migrate to smaller orbits.

As has been shown by Athanassoula (1992a); Regan & Teuben (2003) and others, the existence of a circumnuclear ring inside a large scale bar depends, among other factors, on the orbit families that make up the circumnuclear region. $x_1$ orbits are elongated along the asymmetric potential and are the main orbits that make up the large scale bar. $x_2$ orbits on the other hand, are oriented perpendicular to the bar. Gas orbits slowly turn from one to the other in a bar potential. That $x_2$ orbits are again symmetric to the large scale stellar bar potential, which is important, because there should not be *net* gravitational torques over the orbits (i.e. no further shocks in the gas). $x_2$ orbits are therefore able to serve as repositories for gas. If there is a significant portion of $x_2$ orbits present in the circumnuclear region, gas can settle on them and build up a circumnuclear gas ring.

The connection between dust lanes, the nuclear spirals and the circumnuclear rings is very clear observationally. The dust/gas lanes of the bar do not extend to the nucleus in the case of a ring and actually end at the ring radius. Two points can often be seen in the gaseous ring, offset by 180°, where the lanes connect to the ring. They are called 'contact points', following Böker et al. (2008). So, after being shocked and having lost most angular momentum, infalling gas enters the circumnuclear ring at the contact points and will stay on the $x_2$ orbits. The immediate result of this situation is that the gas density in the ring will increase with continued inflow, with star formation as the natural consequence.

The most straight-forward star formation model for circumnuclear rings has been proposed by Elmegreen (1994). The gas density will build up until it reaches a critical density for star formation. The entire ring will become unstable and star formation will proceed throughout the ring. The time scale of the onset of star formation is then directly related to the inflow rate onto the ring. This scenario was called 'popcorn' by Böker et al. (2008), who themselves proposed another scenario.

Table 3.1: Characteristics of the SAURON and OASIS datasets.

| IFU | Mode | # Expo | Exp. Time | Spectral Sampling | Spatial Sampling | Expo FoV | Total FoV |
|---|---|---|---|---|---|---|---|
| OASIS | MR 516 | 5 | 30 min | 2.15 Å | 0.2″ | 10.3″ × 7.4″ | |
| OASIS | MR 661 | 4 | 30 min | 2.14 Å | 0.2″ | 10.3″ × 7.4″ | |
| SAURON | LR | 26 | 30 min | 1.15 Å | 0.8″ | 42″ × 33″ | 135″ × 90″ |

This second scenario proposes an azimuthal age gradient for the recently formed stars, starting at the contact points. Since gas enters the ring at two distinct positions, it stands to reason that the gas density in the ring is higher at the contact points (termed 'overdensity regions', or 'ODR' by the authors) than elsewhere in the ring. The critical density for star formation will be reached first at (or close to) those positions. By overall rotation of the system these newly formed star clusters will be azimuthally distributed in the ring, while star formation continues at the contact points, like 'pearls-on-a-string'.

NGC 6951 is a good candidate to investigate which of these two scenarios holds true and estimate the life time of the circumnuclear ring. NGC 6951 is a nearby (24.1 Mpc, Tully, 1988) SAB(rs)bc galaxy. It has a circumnuclear ring at a radius of 5″ or 580 pc. It has a low inclination (42.6°, Haan et al., 2009), which provides a clear view of the entire ring. Its molecular gas dynamics in and around the ring have already been studied in detail in the previous chapter (Van der Laan et al., 2011), as well as by others, (Kohno et al., 1999; Krips et al., 2007; Storchi-Bergmann et al., 2007). The gravitational torques acting on the cold molecular gas were also analyzed (Haan et al., 2009; Van der Laan et al., 2011). Mazzuca et al. (2008) have investigated the Hα regions in the ring, and found young stellar ages (<10 Myr). No other determination of the ages of the stellar populations of the ring has been published to date.

New observations and archival data retrieved for this study will be presented in §3.2. In §3.3 the known relevant properties of the ring are summarized. In §3.4 the extinction in the ring is derived, before detailing the detection of star clusters in §3.5. §3.6 contains the determination of the ages of the star clusters and determination of the ages of the overall stellar content based on SAURON data. A discussion with respect to star formation scenarios and ring life time is given in §3.7. A summary follows in §3.8.

## 3.2 Observations and Archival Data

### 3.2.1 OASIS data

The OASIS Integral-Field Unit (McDermid et al., 2004) is installed at the William Herschel Telescope (WHT) in La Palma (Canary Islands). Two individual OASIS configurations were used, namely the MR 516 and MR 661, which, respectively, cover the spectral range around the Hβ, Mg lines ([4760 − 5560Å]) and around Hα, [NII], [SII] lines ([6210 − 7010Å]) at a resolution of $R \sim 1500$, and a sampling of about 2.15Å per pixel (see the OASIS/WHT page for further details). For both configurations, the 22 mm enlarger was used, providing a field of view of approximately 10″3 × 7″4 (see Fig. 3.1) with original spaxels of 0″26.
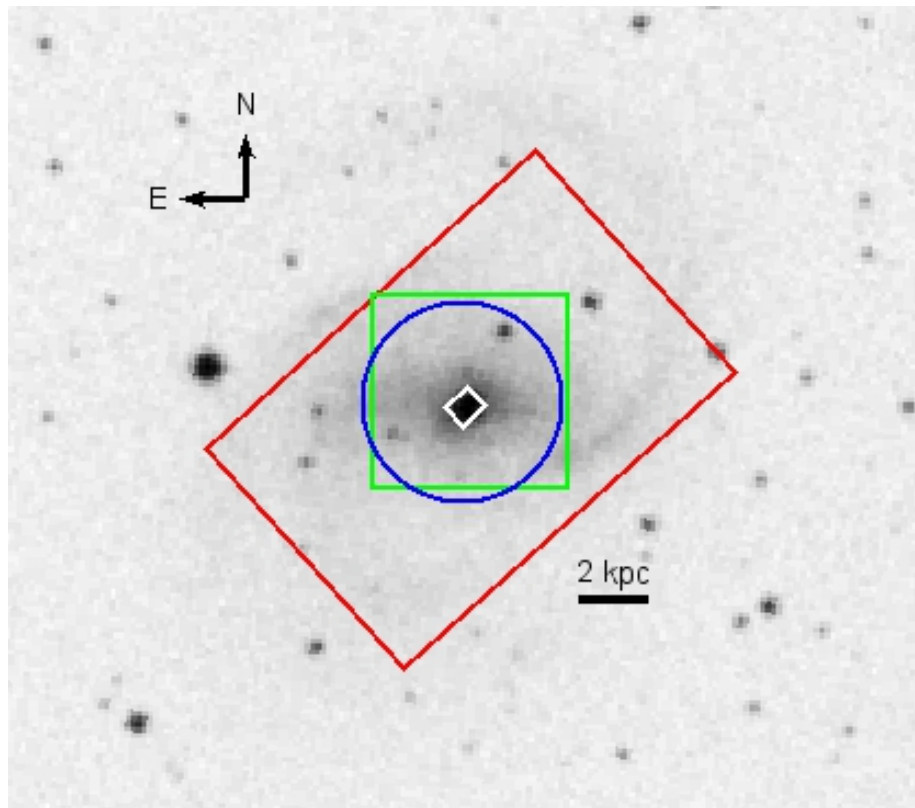
Figure 3.1: Overlay of the Field-of-View of various datasets presented in this chapter.
From small to large: OASIS (white), *HST* (green), PdBI (blue), SAURON (red).

NGC 6951 was targeted during a run in July 2006, and we obtained five and four 30 min exposures, with the MR 516 and MR 661 configurations, respectively, centered on the galaxy nucleus. Slight dithering between consecutive exposures was applied to allow for a better rejection of bad pixels or faulty spectra. Details are provided in Table 3.1.

All the OASIS data were reduced using the XOasis data reduction software[1], developed by CRAL (Arlette Pécontal and coll.), and adapted to the above-mentioned setups. This requires the creation of a spectral mask, following a detailed model of the optical path for the instrument, which allows an accurate optimal extraction of the signal from the raw exposures. The detailed reduction pipeline includes CCD corrections (bias, fringing, removal of the overscans), wavelength calibration, flat-fielding (using both lamp calibrations and sky exposures), and flux calibration. Each individual exposure is then truncated to a common wavelength domain (from 4770Å to 5530Å for MR 516, and from 6620Å to 6990Å for MR 661). We then reconstruct images by fully integrating over the spectral direction, and recenter each individual data cube so that the center of NGC 6951 corresponds to $(0,0)$. The individual exposures are then merged, taking into account the effect of differential refraction, by re-projecting the cubes onto a common spatial grid centered at $(0,0)$ with spaxels of $0''2^2$. The final merged cubes have a spectral sampling of 2.15 Å for the MR 516 configuration, and 2.14 Å for the MR 661.

### 3.2.2 SAURON data

NGC 6951 was observed with SAURON at the WHT (Bacon et al., 2001) during a run in August 2003. Individual exposures cover a field of view of about $41'' \times 33''$, with spaxels of $0''94$, a spectral resolution of 4.2 Å and spectral sampling of 1.15 Å over the range 4780 Å up to 5350Å. The spectral coverage of the SAURON datacubes overlaps with the OASIS MR 516, though it is significantly shorter in wavelength coverage. The coarser spatial sampling allows for a much larger spatial coverage of the disk of NGC 6951 than with OASIS, see also Table 3.1. We obtained a total of twenty-six 30 min exposures, the goal being to cover as much of the stellar bar as possible. The total time spent on each pointing was adopted according to the average surface brightness, and included some slight dithering for each pointing to prevent systematics. The final area covered by the complete mosaic is $135'' \times 90''$ (see Fig. 3.1). The data from the single, central exposure has been presented previously by Dumas et al. (2007).

The data reduction of all SAURON exposures was performed using a pipeline based on XSauron which is similar to the XOasis version, but adapted to the different optics and setup. The reduction steps are thus very similar to the ones described in the previous Section for OASIS. The biggest differences lie in the characteristics of the spectral mask, and the existence, for SAURON of about 150 dedicated sky lenses which allow for an accurate sky subtraction for each exposure.

The fully calibrated individual exposures were then recentered (using a direct image of the galaxy as a reference) and merged, by projecting each data cube on a common grid with $0''8^2$ spaxels.

---

[1]http://www-obs.univ-lyon1.fr/labo/oasis/download/

### 3.2.3   Spectral fitting of the IFU datasets

We applied standard routines to extract the kinematics: the stellar kinematics (velocity, velocity dispersion and Gauss-Hermite $h_3$ and $h_4$ values) with pPXF (Cappellari
& Emsellem, 2004; Emsellem et al., 2004) using a set of stellar templates extracted
from the MILES library (Sánchez-Blázquez et al., 2006; Falcón-Barroso et al., 2011)
and the IDL implementation available from Michele Cappellari's web page[2], and the
gas kinematics via a version of GANDALF (kindly adapted for our purpose by Marc
Sarzi, Sarzi et al., 2006). Fitted emission lines include H$\beta$, the doublets [OIII] ($\lambda$
(4959,5007) Å), [NI] ($\lambda$ (5200,5202) Å), in both SAURON, and OASIS MR 516, and
[OI] ($\lambda$ (6300,6364) Å), H$\alpha$ ($\lambda$ 6562.8 Å), and the doublets [NII] ($\lambda$ (6548,6583) Å)
and [SII] ($\lambda$ (6717,6731) Å) for the OASIS MR 661 data cube. We emphasize that H$\beta$
and H$\alpha$ are present both in emission and absorption, however the combined use of
pPXF and GANDALF does take this into account.

The resulting emission line maps from the spectral fitting for OASIS are shown in
Fig. 3.2. It can be seen that the OASIS FoV just covers the circumnuclear ring. The H$\alpha$
and H$\beta$ emission is mostly concentrated in the ring, while the [OI] and [OIII] emission
is limited to the nucleus. The [NII] and [SII] emitting gas is present in both the nucleus
and ring. There are bright hot-spots in the ring that are seen in H$\alpha$, H$\beta$, [NII] and [SII].
The velocity field and dispersion are only shown for H$\alpha$, but are very similar for the
other emission lines. The increase in the velocity dispersion in the western half of the
ring was also seen in the SAURON maps by Dumas et al. (2007) and seems to coincide
with the lowest intensities of H$\alpha$ and H$\beta$ flux emission in the ring.

The spectral fitting results from the SAURON mosaic are presented in Fig. 3.3. In the
top-left panel of Fig. 3.3 we show the total intensity over the FoV of the mosaic. The
peak intensity of the central region has been saturated to show the details of the entire
stellar bar region. The stellar bar is orientated approximately east-west on the sky. The
few high-intensity peaks are foreground stars. The stellar velocity field and dispersion
are also shown in the top row.

In the bottom row of Fig. 3.3 the H$\beta$, [NI] and [OIII] emission line maps are
presented. It is clear that their emission is concentrated in the circumnuclear region. In
the case of H$\beta$, a keen eye can make out the ring shape of the emission in this figure
(exactly as was seen from the OASIS map).

### 3.2.4   *HST* images

I retrieved F547M, F606W, F658N, F814W and F330W images of NGC 6951 from the
MAST *HST* archive. I extracted them from the archive calibrated with the "best" reference files. I also utilize NICMOS F110W and F160W images from the *HST* archive
already used in the previous chapter (original: Hunt & Malkan, 2004). Finally, we
obtained a Pa$\alpha$ image, which was observed during the same campaign and reduced
using the same approach as for NGC 1097 in Hsieh et al. (2011). The full sample and
detailed data reduction for the Pa$\alpha$ image are presented in Liu et al. (in prep.). A list
of all images used is given in Table 3.2.

---

[2] http://www-astro.physics.ox.ac.uk/~mxc/idl/
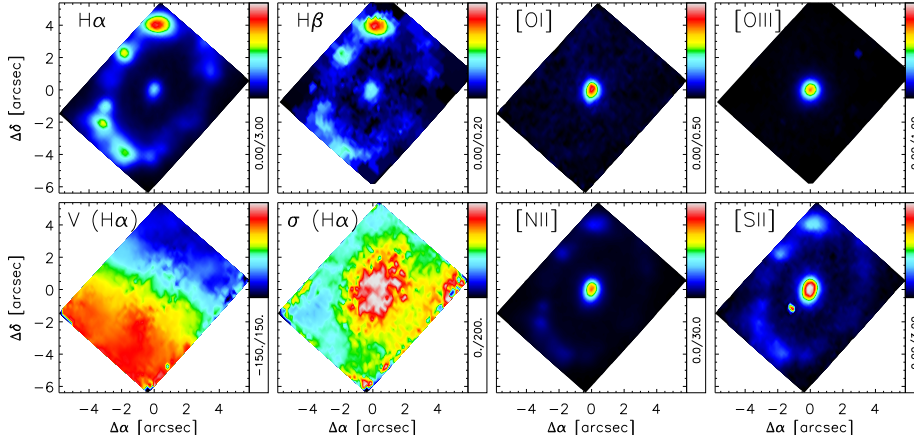
Figure 3.2: OASIS intensity maps of the emission lines Hα, Hβ, [OI], [OIII], [NII] and [SII], as well as the velocity and velocity dispersion map of Hα. The color scale in each panel indicates the intensity or velocity, the range of which is given below the color bar. The orientation of the maps is north up, east left. All positions are relative to the nucleus. The velocity range in the bottom-left panel is [-150, 150] km s$^{-1}$, with an assumed systemic velocity of NGC 6951 is 1425 km/s. The velocity dispersion range in the adjacent panel is [0, 200] km/s.
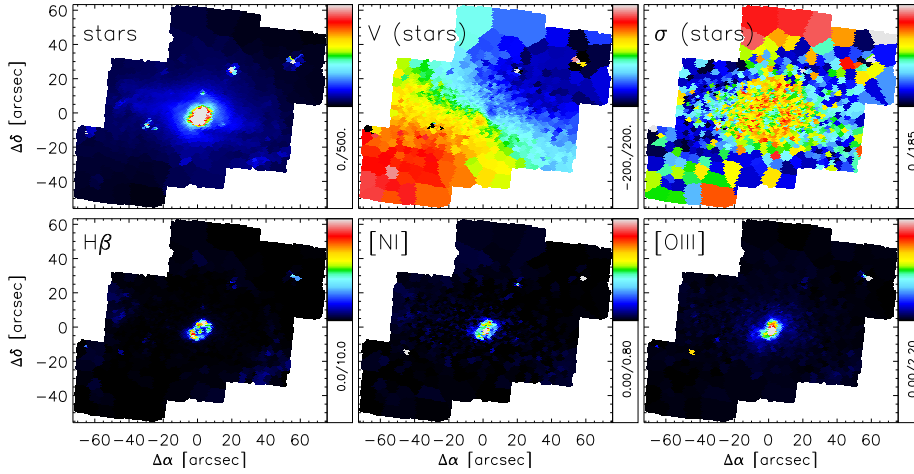


Figure 3.3: SAURON intensity maps of the stellar light, Hβ, [NI] and [OIII] emission lines, as well as the stellar velocity and velocity dispersion map. The color scale in each panel indicates the intensity or velocity, the range of which is given below the color bar. The orientation of the maps is north up, east left. All positions are relative to the nucleus. The velocity range in the top-middle panel is [-200, 200] km s$^{-1}$, the assumed systemic velocity of NGC 6951 is 1425 km/s. The velocity dispersion range in the top-right panel is [0, 185] km/s.

Table 3.2: *HST* archival data

| Filter | Program ID | Exposure [s] | Obs. Date | PHOTFLAM | Instrument | Scale [″/pixel] |
|--------|-----------|-------------|-----------|----------|-----------|----------------|
| F187N* | 11080 | 1151.767 | 13-02-2007 | $3.6837500\times10^{-18}$ | NICMOS NIC3 | 0.10 |
| F160W | 7331 | 255.923 | 16-12-1997 | $2.3600094\times10^{-19}$ | NICMOS NIC2 | 0.076 |
| F110W | 7331 | 255.923 | 16-12-1997 | $4.3320170\times10^{-19}$ | NICMOS NIC2 | 0.076 |
| F547M | 5419 | 300 | 16-07-1994 | $7.691168\times10^{-18}$ | WFPC2/PC | 0.046 |
| F606W | 8597 | 160 | 18-11-2000 | $1.899711\times10^{-18}$ | WFPC2/PC | 0.046 |
| F658N | 9788 | 700 | 24-10-2003 | $1.9597158\times10^{-18}$ | ACS WFC1 | 0.05 |
| F814W | 9788 | 120 | 24-10-2003 | $6.9255574\times10^{-20}$ | ACS WFC1 | 0.05 |
| F330W | 9379 | 1200 | 17-08-2002 | $2.2688470\times10^{-18}$ | ACS HRC-FIX | 0.025 |

**Notes:** List of the observations extracted from the *HST* archive. *The Pa$\alpha$ image has been corrected for continuum flux with a F190N-filter image taken at the same time.

The H$\alpha$ image was carefully continuum subtracted with the F606W image, as was the Pa$\alpha$ (F190N) image using the F187N image. The F658N filter passband includes emission from the [NII] double line emission. From spectra presented in Storchi-Bergmann et al. (2007) the ratio [NII]6583 Å /H$\alpha$ is known to be $\sim 0.3$ throughout the ring, implying a 37% contribution to the observed flux from [NII]6548 Å and [NII]6583 Å in the *HST* F658N filter for a V$_{sys}$ of 1425 km/s, for which we correct.

## 3.3  NGC 6951's circumnuclear ring so far...

Before we start with the analysis of the stellar properties of NGC 6951's circumnuclear ring, a brief summary of the gaseous properties of the circumnuclear region that are known to date is presented. For clarity later on, all numbers pertinent to the discussion later are also listed in Table 3.3. The large scale stellar bar in NGC 6951 has a PA of 84° on sky (Mulchaey & Regan, 1997). Its semi-major axis is 3.0 kpc. The dust lanes of the bar are thus orientated almost horizontally on the sky. The contact points in the ring are in the north and south of the ring.

$^{12}$CO(1-0) and $^{12}$CO(2-1) observations, taken with the PdBI and IRAM 30m telescope, of the circumnuclear region of NGC 6951 were presented in the previous chapter (Sect. 2.2). The resolution of the CO(1-0) observations is 3.11″ by 2.59″, the CO(2-1) observations are 1.72″ by 1.56″. The FoV of the CO(1-0) observations is shown in Fig. 3.1, the FoV of the CO(2-1) data is about half that size. Both completely cover the ring. Their r.m.s. noise corresponds to M$_{H_2} \sim 10^5$ M$_\odot$/beam. A total H$_2$ mass of $2.2 \times 10^9$ M$_\odot$ was derived from the CO(1-0) observations, assuming a Galactic conversion factor. An HCN(1-0) intensity map obtained with PdBI was presented by Krips et al. (2007). A map with slightly different *uv*-weighting from that dataset was kindly provided by M. Krips (priv. comm.), with a beam size of 1.89″ by 1.83″(PA 78.7°).

The key points for the molecular gas morphology are prominent gas spiral arms, that are co-spatial with the dust lanes along the large-scale stellar bar and end at the radius of the circumnuclear ring. The CO(2-1) observations, which have a higher spatial resolution, show that the spiral arms continue into a ring. The HCN(1-0) traces higher density molecular gas than CO, and the HCN intensity distribution shows a similar morphology to the CO(2-1) molecular gas. However, the intensity maxima are
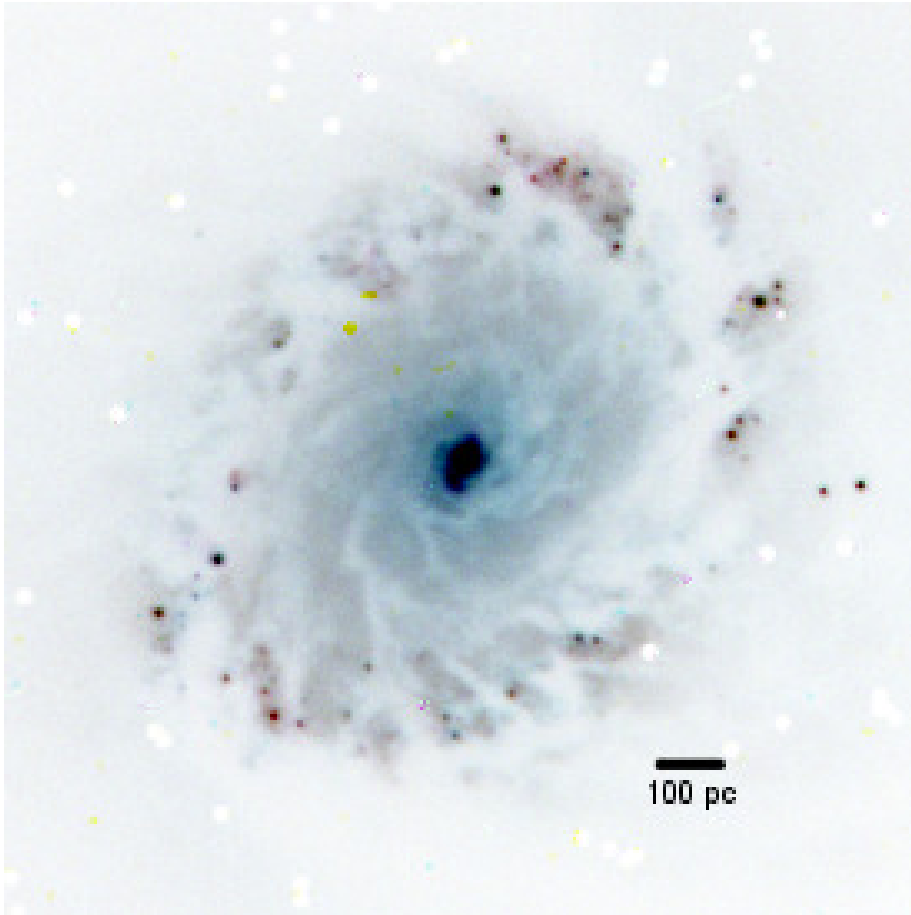
Figure 3.4: False color image of the circumnuclear ring in NGC 6951, based on the F814W (red), F606W (green) and F547M (blue) broad band filters. The image (~ 14″× ~ 14″) is orientated with north pointing up and east to the left. The center has been saturated for better visibility of the ring, and bad pixels have been removed.

Table 3.3: Properties of NGC 6951

| Parameter | Value | Reference |
|---|---|---|
| Type | SAB(rs)bc | (1) |
| Nuclear Activity | LINER/Seyfert 2 | (2) |
| Dynamical Center (Locus Radio Continuum) | | |
|   RA (J2000) | $20^h 37^m 14.123^s$ | (3,4) |
|   Dec (J2000) | $66°06'20.09''$ | (3,4) |
| Inclination Angle | $42.6°$ | (5) |
| Position Angle | $138°$ | (5) |
| Adopted Distance | 24.1 Mpc | (6) |
| Stellar bar PA | $84°$ | (7) |
| Mass $H_2$ (r<3 kpc) | $1.6 \times 10^9$ $M_\odot$ | (8) |
| Mol. gas inflow rate onto ring | $2.0 M_\odot$/yr | (8) |
| Large scale bar pattern speed | $28.9 \pm 1.2$ km/s/kpc | (9) |
| $V_{sys}$ | 1425 km/s | (5) |
| Period pattern speed | 213 Myr | (9) |
| 1 rotation for a ring orbit | 24 Myr | (9) |

**References:** (1) de Vaucouleurs et al. (1991), (2) Pérez et al. (2000), (3) LEDA, Krips et al. (2007), (4) Saikia et al. (2002), (5) Haan et al. (2009), (6) Tully (1988), (7) Mulchaey & Regan (1997), (8) Van der Laan et al. (2011), (9) this work

at slightly different positions in the ring. In the previous chapter I derived, from modeling the orbits in the circumnuclear region, that the inflow rate of gas onto the ring is $\sim$2.0 $M_\odot$ per year.

The HI distribution, presented in Haan et al. (2009), shows that the circumnuclear region of NGC 6951 is HI-deficient. The neutral ISM in the circumnuclear region is thus molecular gas dominated. Given an estimate for the dynamical mass at 1 kpc, ($M_{dyn} = \frac{rv^2}{G} \approx 8 \times 10^9 M_\odot$, with v=200km/s), atomic and molecular gas makes up approximately 25% of the dynamical mass within this radius.

Two determinations of the large scale bar pattern speed of the stellar bar in NGC 6951 exist in the literature. Aguerri et al. (1998) obtained a value of $\Omega_p$ = 30.3 km/s/kpc (when compensating for the difference in adopted distance) based on the rotation curve and location of the corotation radius and Haan et al. (2009) derived a value of $\Omega_p$ = 23 km/s/kpc based on an analysis of dynamic resonances. The SAURON IFU mosaic covers most of the large scale stellar bar of NGC 6951, and is ideally suited to measure the pattern speed using the model-free Tremaine-Weinberg method (Tremaine & Weinberg, 1984). Using the SAURON mosaic gives a value of 28.9±1.2 km/s/kpc, corrected for inclination (42.6°) and at a distance of 24.1 Mpc.

With a patternspeed of 28.9 km/s/kpc, the pattern will take 213 Myr to complete one rotation. The gas and stars rotate with a velocity of $\sim$150 km/s at the ring radius. They will thus complete a rotation in the ring in 24 Myr.

## 3.4   Extinction in the ring

From the three Hydrogen lines (H$\alpha$, H$\beta$ and Pa$\alpha$) in our data sets I can compute a spatial distribution of the extinction in the ring. While determining the extinction is not directly crucial to the overarching goal in this thesis, it provides a consistency cross-check on the derived color excesses of the star cluster fitting. I use two different ratios to compute the extinction, the H$\alpha$/H$\beta$ ratio (as derived from the OASIS data) and the H$\alpha$/Pa$\alpha$ ratio (as derived from the *HST* data).

Both the H$\alpha$ and H$\beta$ maps are obtained during the spectral fitting of the OASIS data cubes. The fitting takes H$\alpha$ and H$\beta$ stellar absorption into account as explained in Sect. 3.2.3. In the case of case B recombination, the ratio H$\alpha$/H$\beta$ will be 2.86 (Osterbrock, 1989). Extinction will increase the value. In individual pixels, I find ratios as high as ~4, which is equal to an extinction of ~1 magnitude. Inside the ring, the surface brightness of especially H$\beta$ is so low, that no reliable H$\alpha$/H$\beta$ ratio can be computed. Where that is the case, the position has been left blank. In Fig. 3.5 (*right*) the color excess, E(B-V), based on the H$\alpha$/H$\beta$ ratio is plotted. Color excess is a wavelength independent measure of extinction, and is related to extinction via E(B-V) = $A_V$/$R_V$, where $R_V$ gives the total-to-selective extinction, which we assume to be 4.05 (starburst value of Calzetti et al., 2000).

The FoV of OASIS only barely covers the entire ring. Nevertheless, it is possible to see some trends in the H$\alpha$/H$\beta$ map. The extinction is clearly higher near and 'down-stream' from the contact points between ring and bar-induced gas lanes (galaxy rotation is clockwise).

The ratio of the *HST* H$\alpha$ and Pa$\alpha$ observations provides another measure of the extinction. The advantages of these observations are the complete view of the ring and higher spatial resolution (Fig. 3.5, *left*).

Without extinction the expected ratio H$\alpha$/Pa$\alpha$ is about 8.5 (Hummer & Storey, 1987, case B recombination). Inside the ring the intensity of both H$\alpha$ and Pa$\alpha$ is too low to obtain reliable ratios. Those positions have been left blank. Again we see the highest extinctions 'down-stream' from the contact points. In the western part of the ring we also find 'pockets' of higher extinction which can be related to the highest intensity CO and HCN peaks. These places are heavily obscured and dense, and thus are likely the sites of future star formation. Comparison with the H$\alpha$ distribution shows the brightest H$\alpha$ regions to be anti-correlated with extinction.

The H$\alpha$/H$\beta$ based color excess map (OASIS ) and the H$\alpha$/Pa$\alpha$ based color excess map (*HST*) show similar distributions, and have similar values in the range [0.2 - 0.5] mag.

## 3.5   Star clusters

Star clusters are a prime way to study the ages of stellar populations; all the stars within a cluster are coeval and clusters are bright and compact, thus easily observable even over large distances. At the distance of NGC 6951 star clusters are point sources and can easily be separated from the background light in the galaxy.
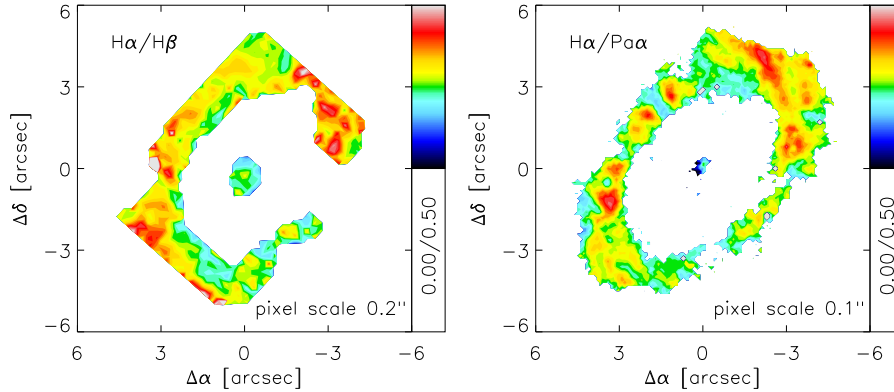
Figure 3.5: Left: Color excess E(B-V) in the ring as measured from the $H_\alpha/H_\beta$ line ratio using the OASIS line maps. Right: Color excess in the ring as measured from the $H\alpha/Pa\alpha$ line ratio using *HST* images. The pixel scales of each map are shown in the lower-right corner of each panel.

### 3.5.1   Identification

Two independent routines were used for the detection and photometry of the star clusters in the ring of NGC 6951. These routines are the DAOPHOT package (Stetson, 1987; Stetson et al., 1990; Stetson, 1992) in IRAF and SExtractor (Bertin & Arnouts, 1996). With this approach, the strengths of both methods can be exploited to obtain the most complete star cluster candidate list.

For the detection of the star clusters a composite optical image was created out of 4 individual optical bands; F547M, F606W, F814W and F330W. First, the F606W, F814W and F330W images were aligned with the F547M image using standard procedures in IRAF. For the F814W and F330W bands the images were resampled to the F547M pixel size while conserving the flux. The four resulting images were then normalized and added together.

Applying DAOFIND, 33 star clusters candidates were detected in the composite optical image (within r ~20″). The star cluster detection in the NIR images was done separately from the composite optical image, as the NIR images have a lower angular resolution. The F110W image was used to detect the NIR star clusters and the resulting positions were applied to the F160W image. Most of the NIR detections have a counterpart in the composite optical image, but several sources were detected without one. This leads to a total of 42 detected star clusters candidates using the DAOPHOT method.

Next, SExtractor was run. The strength of SExtractor is its ability to 'de-blend' crowded regions. As can be seen from the false color image (Fig. 3.4), especially the northern region of the ring is very crowded. For detection and the subsequent photometry of star cluster locations the same composite optical image from the DAOFIND analysis was used. SExtractor automatically determines apertures around the selected source. If the individual images were used independently, the selected apertures be-

tween the different wavelengths could vary, which would introduce systematic changes in our photometry. By using the composite optical image as the 'detection image' this is avoided and each source will have the same aperture at the different wavelengths.

The SExtractor output is filtered by discarding all detections flagged as 'bad' by SExtractor itself (e.g. likely to be cosmic rays or one or more pixels that are saturated). The likely candidates are further constrained by location (a rectangular area around the ring of $12'' \times 12''$) and by relative error in the measured flux ($<20\%$). 43 star cluster candidates are detected.

In total, 55 different star clusters candidates are detected (see Table 3.4), about half of which are detected by both DAOPHOT and SExtractor (28 out of 55 or 51%).

## 3.5.2 Properties

The 55 star cluster candidates can be compared with the work by Barth et al. (1995), who used a single F547M image (the same one I extracted from the archive). All 24 sources already presented in that work are also included in my list. The additional candidates lie in the northern region and several have lower surface brightnesses. Investigation of the F330W image, which has the finest native pixel scale, shows that some of my detections, particularly in the crowded northern region of the ring, are actually still composed of two or multiple point sources/star clusters.

SExtractor simultaneously detects the star cluster candidates and measures their flux. For the star clusters candidates identified with DAOFIND, their photometric fluxes were obtained using PHOT (also in the IRAF/DAOPHOT package). For the measurement the F330W and F814W images are used at the resolution of the F547M and F606W images. In PHOT the circular apertures for the optical images were chosen to have a radius of 2 pixels (0.09"). This radius contains most of the observed PSF (4 pixels $\approx$ FWHM $\sim 20$ pc), while minimizing the contamination from other sources (such as other close by star clusters). The sky subtraction was based on an annulus around each source with radii between 6 and 16 pixels. Flux outliers in this annulus (e.g. other clusters or cosmic-rays, which would over-estimate the sky-levels) were automatically excluded from the sky estimate. For the NIR images an photometry aperture radius of 1.2 pixels was used, which corresponds to a size equal to the optical aperture. The radii of the sky estimate annulus were again 6 and 16 pixels for the NIR images.

The TinyTim package[3] was used to obtain the necessary aperture corrections for each band. The aperture corrections are for the F330W band $1.16 \times f_{330}$, F547M band $1.29 \times f_{547}$, F606W band $1.31 \times f_{606}$, F658N band $1.40 \times f_{658}$, F814W band $1.36 \times f_{814}$, F110W band $1.38 \times f_{110}$ and F160W band $1.59 \times f_{160}$.

All measured photometric fluxes are converted into absolute magnitudes, using a distance modulus of 31.9 mag. Barth et al. (1995) used a distance modulus of 31.2, which corresponds to a distance of 17.4 Mpc. Assuming a distance of 24.1 Mpc to NGC 6951, as done in the previous chapter increases the distance modulus to 31.9, or correspondingly increases the magnitudes by -0.7 mag. The absolute magnitudes are given in Table 3.4.

---

[3]http://www.stsci.edu/software/tinytim/tinytim.html
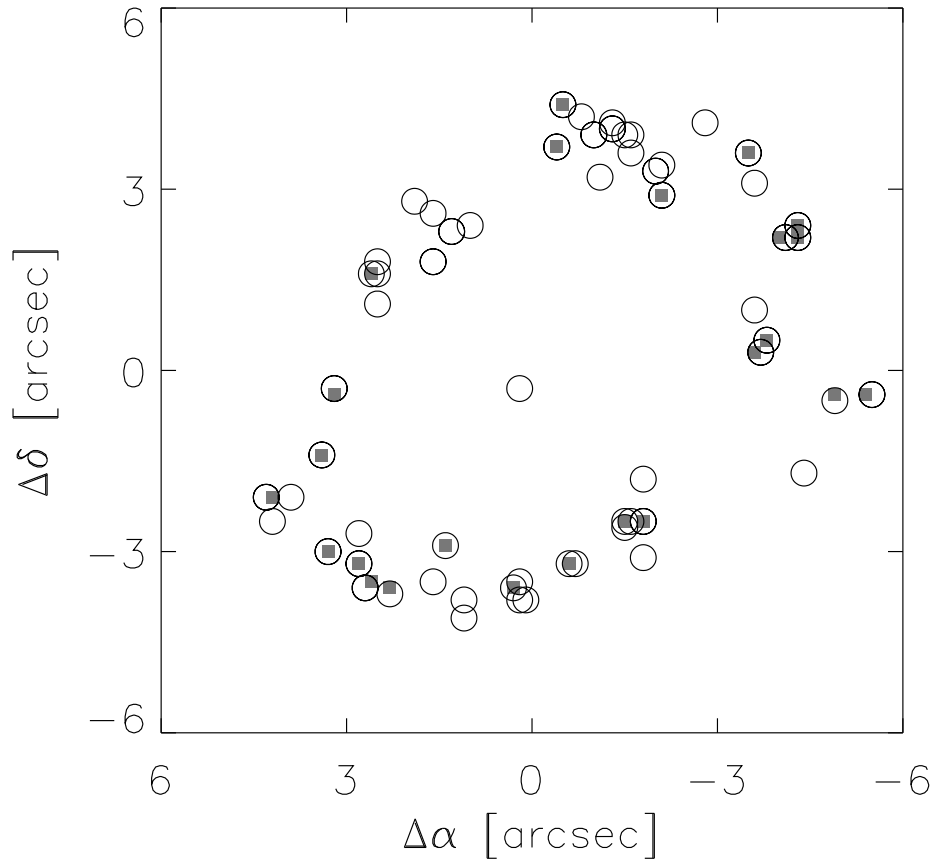
Figure 3.6: Locations of the candidate star clusters as detected with IRAF/DAOPHOT
and SExtractor (open circles). I have also indicated the locations of the star clusters
found by Barth et al. (1995) (grey squares). The axes denote the projected distances in
arcseconds from the photometric nucleus, see Table 3.3.

The absolute magnitudes from both methods are in good agreement with each other
and with Barth et al. (1995), with at most a 0.5 mag difference in the optical bands and
1 mag in the NIR bands, mostly due to the differences in sky subtraction. These values
have not (yet) been corrected for extinction. A measure for the intrinsic extinction is
derived during the star cluster fitting.

Table 3.4: Star clusters identified with IRAF/DAOPHOT and SExtractor

| ID | $\Delta\alpha$ ["] | $\Delta\delta$ ["] | $M_{330}$ | $\sigma_{330}$ | $M_{547}$ | $\sigma_{547}$ | $M_{606}$ | $\sigma_{606}$ | $M_{658}$ | $\sigma_{658}$ | $M_{814}$ | $\sigma_{814}$ | $M_{110}$ | $\sigma_{110}$ | $M_{160}$ | $\sigma_{160}$ |
|---|---|---|---|---|---|---|---|---|---|---|---|---|---|---|---|---|
| 1 | -0.5 | 4.4 | -10.2 | 0.03 | -10.4 | 0.06 | -10.3 | 0.04 | -10.5 | 0.48 | -10.0 | 0.11 | -9.2 | 0.41 | -8.6 | 0.40 |
|  | -0.5 | 4.4 | -10.3 | 0.03 | -10.6 | 0.07 | -10.5 | 0.05 | -11.0 | 0.46 | -10.3 | 0.12 | -9.8 | 0.38 | -9.5 | 0.34 |
| 2 | -0.8 | 4.2 | -10.0 | 0.03 | -9.4 | 0.10 | -9.0 | 0.08 | -9.7 | 0.68 | -8.5 | 0.23 | -8.3 | 0.62 | -7.4 | 0.71 |
| 3 | -2.8 | 4.1 | -5.6 | 1.49 | -11.4 | 0.04 | ... | ... | -6.8 | 3.28 | -5.0 | 2.20 | ... | ... | ... | ... |
| 4 | -1.3 | 4.1 | -11.0 | 0.03 | -10.7 | 0.07 | -10.5 | 0.08 | -11.0 | 0.47 | -10.0 | 0.16 | ... | ... | ... | ... |
| 5 | -1.3 | 4.0 | -11.4 | 0.02 | -10.7 | 0.05 | -10.7 | 0.04 | -11.3 | 0.33 | -10.1 | 0.11 | -8.5 | 0.56 | -7.9 | 0.55 |
|  | -1.3 | 4.0 | -11.1 | 0.02 | -10.9 | 0.06 | -10.8 | 0.05 | -11.5 | 0.37 | -10.4 | 0.12 | ... | ... | ... | ... |
| 6 | -1.0 | 3.9 | -10.6 | 0.02 | -10.0 | 0.07 | -9.9 | 0.05 | -11.7 | 0.28 | -8.9 | 0.19 | -7.5 | 0.90 | -6.6 | 1.03 |
|  | -1.0 | 3.9 | -10.7 | 0.03 | -10.3 | 0.09 | -10.4 | 0.07 | -12.0 | 0.28 | -9.5 | 0.20 | ... | ... | ... | ... |
| 7 | -1.6 | 3.9 | -10.0 | 0.03 | -10.0 | 0.07 | -10.1 | 0.05 | -10.8 | 0.42 | -10.0 | 0.11 | -8.4 | 0.61 | -7.1 | 0.80 |
|  | -1.5 | 3.9 | -10.5 | 0.05 | -10.5 | 0.09 | -10.5 | 0.08 | -11.0 | 0.46 | -10.1 | 0.16 | -9.8 | 0.41 | -9.0 | 0.54 |
| 8 | -0.4 | 3.7 | -10.5 | 0.03 | -11.0 | 0.04 | -11.0 | 0.03 | -11.0 | 0.39 | -10.9 | 0.08 | -10.2 | 0.26 | -9.8 | 0.23 |
|  | -0.4 | 3.7 | -10.5 | 0.03 | -11.1 | 0.05 | -11.0 | 0.04 | -11.2 | 0.42 | -10.8 | 0.09 | -10.2 | 0.33 | -9.9 | 0.32 |
| 9 | -1.6 | 3.6 | -10.5 | 0.02 | -9.4 | 0.09 | -9.3 | 0.07 | -10.6 | 0.47 | -8.4 | 0.24 | -7.4 | 0.95 | -6.2 | 1.21 |
| 10 | -3.5 | 3.6 | -10.7 | 0.02 | -10.1 | 0.07 | -10.1 | 0.04 | -10.5 | 0.48 | -10.4 | 0.10 | -9.8 | 0.31 | -9.1 | 0.32 |
|  | -3.5 | 3.6 | -10.5 | 0.02 | -10.2 | 0.08 | -10.3 | 0.05 | -11.1 | 0.44 | -10.5 | 0.11 | -10.0 | 0.33 | -9.6 | 0.33 |
| 11* | -2.1 | 3.4 | ... | ... | ... | ... | ... | ... | ... | ... | ... | ... | -10.3 | 0.36 | -10.0 | 0.32 |
| 12 | -2.0 | 3.3 | -10.5 | 0.03 | -10.6 | 0.05 | -10.5 | 0.04 | -10.2 | 0.56 | -10.2 | 0.10 | -9.7 | 0.32 | -9.4 | 0.27 |
|  | -2.0 | 3.3 | -10.4 | 0.03 | -10.6 | 0.06 | -10.6 | 0.06 | -10.8 | 0.50 | -10.4 | 0.12 | -10.0 | 0.36 | -9.7 | 0.34 |
| 13 | -1.1 | 3.2 | -8.8 | 0.12 | -9.9 | 0.08 | -10.0 | 0.05 | -10.3 | 0.52 | -10.1 | 0.11 | -9.6 | 0.34 | -9.1 | 0.32 |
| 14* | -3.6 | 3.1 | ... | ... | ... | ... | ... | ... | ... | ... | ... | ... | -10.5 | 0.33 | -10.3 | 0.27 |
| 15 | -2.1 | 2.9 | -10.7 | 0.02 | -10.5 | 0.05 | -10.6 | 0.04 | -10.8 | 0.42 | -10.3 | 0.10 | -9.7 | 0.33 | -9.1 | 0.31 |
|  | -2.1 | 2.9 | -10.6 | 0.02 | -10.5 | 0.07 | -10.5 | 0.05 | -10.7 | 0.53 | -10.3 | 0.12 | -9.6 | 0.45 | -9.3 | 0.43 |
| 16* | 1.9 | 2.8 | ... | ... | ... | ... | ... | ... | ... | ... | ... | ... | -9.1 | 0.65 | -8.6 | 0.64 |

− Continued on next page

Table 3.4 – continued from previous page

| ID | $\Delta\alpha$ ["] | $\Delta\delta$ ["] | $M_{330}$ | $\sigma_{330}$ | $M_{547}$ | $\sigma_{547}$ | $M_{606}$ | $\sigma_{606}$ | $M_{658}$ | $\sigma_{658}$ | $M_{814}$ | $\sigma_{814}$ | $M_{110}$ | $\sigma_{110}$ | $M_{160}$ | $\sigma_{160}$ |
|---|---|---|---|---|---|---|---|---|---|---|---|---|---|---|---|---|
| 17 | 1.6 | 2.6 | -9.8 | 0.05 | -9.7 | 0.09 | -9.8 | 0.05 | -10.5 | 0.47 | -8.9 | 0.19 | -7.5 | 0.92 | -7.1 | 0.80 |
| 18 | 1.0 | 2.4 | -9.8 | 0.05 | -9.7 | 0.08 | -9.4 | 0.07 | -10.5 | 0.49 | -9.0 | 0.18 | -8.4 | 0.59 | -8.2 | 0.49 |
| 19 | -4.3 | 2.4 | -10.4 | 0.02 | -10.2 | 0.07 | -10.0 | 0.05 | -9.9 | 0.63 | -9.7 | 0.13 | -9.3 | 0.38 | -9.2 | 0.31 |
|  | -4.3 | 2.4 | -10.7 | 0.02 | -10.5 | 0.06 | -10.4 | 0.05 | -10.5 | 0.56 | -10.3 | 0.12 | -10.0 | 0.34 | -9.9 | 0.28 |
| 20 | 1.3 | 2.3 | -9.3 | 0.06 | -11.2 | 0.04 | -8.8 | 0.09 | -9.9 | 0.62 | -7.5 | 0.36 | -7.0 | 1.14 | -4.7 | 2.42 |
|  | 1.3 | 2.3 | -9.2 | 0.08 | -11.4 | 0.05 | -8.8 | 0.26 | -10.4 | 0.60 | -7.7 | 0.70 | ... | ... | ... | ... |
| 21 | -4.3 | 2.2 | -10.0 | 0.03 | -9.7 | 0.08 | -9.8 | 0.05 | -10.0 | 0.60 | -9.1 | 0.17 | -8.8 | 0.49 | -8.3 | 0.47 |
|  | -4.3 | 2.2 | -10.4 | 0.03 | -10.3 | 0.07 | -10.3 | 0.05 | -10.6 | 0.54 | -10.1 | 0.13 | ... | ... | ... | ... |
| 22 | -4.1 | 2.2 | -11.6 | 0.01 | -11.4 | 0.04 | -11.3 | 0.03 | -11.4 | 0.32 | -10.9 | 0.07 | -10.2 | 0.26 | -9.7 | 0.24 |
|  | -4.1 | 2.2 | -11.7 | 0.01 | -11.7 | 0.04 | -11.5 | 0.03 | -11.6 | 0.34 | -11.2 | 0.08 | -10.5 | 0.26 | -10.3 | 0.24 |
| 23 | 2.5 | 1.8 | -9.6 | 0.05 | -9.5 | 0.09 | -9.6 | 0.06 | -9.4 | 0.81 | -9.4 | 0.15 | -9.0 | 0.46 | -8.3 | 0.47 |
| 24 | 1.6 | 1.8 | -6.7 | 0.29 | -13.3 | 0.01 | -7.0 | 0.21 | -7.0 | 2.37 | -5.4 | 0.97 | -3.3 | 6.31 | -4.9 | 2.23 |
|  | 1.6 | 1.8 | -7.0 | 0.48 | -13.7 | 0.01 | -7.2 | 1.32 | -8.5 | 1.46 | ... | ... | ... | ... | ... | ... |
| 25 | 2.5 | 1.6 | -10.3 | 0.03 | -10.4 | 0.06 | -10.3 | 0.04 | -10.5 | 0.47 | -10.0 | 0.11 | -9.9 | 0.30 | -9.2 | 0.30 |
|  | 2.6 | 1.6 | -9.9 | 0.04 | -10.2 | 0.08 | -10.1 | 0.07 | -10.4 | 0.60 | -10.0 | 0.14 | -9.7 | 0.40 | -9.4 | 0.38 |
| 26 | 2.5 | 1.1 | -9.4 | 0.06 | -9.9 | 0.07 | -9.8 | 0.05 | -10.2 | 0.56 | -9.7 | 0.13 | -9.2 | 0.41 | -8.5 | 0.42 |
| 27 | -3.6 | 1.0 | -8.8 | 10.00 | -9.4 | 0.11 | -9.4 | 0.09 | -10.6 | 0.55 | -8.9 | 0.23 | ... | ... | ... | ... |
| 28 | -3.8 | 0.5 | -9.9 | 0.04 | -10.4 | 0.06 | -10.3 | 0.04 | -10.9 | 0.40 | -10.2 | 0.10 | -9.2 | 0.41 | -8.5 | 0.42 |
|  | -3.8 | 0.5 | -9.7 | 0.05 | -10.5 | 0.07 | -10.5 | 0.05 | -11.0 | 0.46 | -10.3 | 0.12 | ... | ... | ... | ... |
| 29 | -3.7 | 0.3 | -11.1 | 0.02 | -10.9 | 0.05 | -10.7 | 0.03 | -10.8 | 0.42 | -10.4 | 0.10 | -8.8 | 0.49 | -7.6 | 0.62 |
|  | -3.7 | 0.3 | -11.2 | 0.02 | -11.1 | 0.05 | -11.0 | 0.04 | -11.3 | 0.39 | -10.6 | 0.10 | -9.6 | 0.40 | -9.0 | 0.45 |
| 30 | 3.2 | -0.3 | -10.7 | 0.02 | -10.6 | 0.05 | -10.7 | 0.03 | -12.4 | 0.21 | -10.1 | 0.11 | -8.9 | 0.48 | -8.0 | 0.54 |
|  | 3.2 | -0.3 | -10.2 | 0.03 | -10.1 | 0.08 | -10.2 | 0.06 | -11.9 | 0.29 | -9.8 | 0.15 | -9.1 | 0.52 | -8.3 | 0.68 |
| 31 | 0.2 | -0.3 | -9.6 | 0.06 | -10.9 | 0.05 | -11.5 | 0.02 | -13.2 | 0.14 | -11.3 | 0.06 | -11.4 | 0.15 | -11.2 | 0.12 |
| 32 | -5.5 | -0.4 | -9.3 | 0.04 | -10.4 | 0.06 | -10.4 | 0.04 | -10.4 | 0.50 | -10.2 | 0.10 | -8.9 | 0.46 | -7.9 | 0.55 |
|  | -5.5 | -0.4 | -9.5 | 0.04 | -10.7 | 0.06 | -10.7 | 0.04 | -10.8 | 0.50 | -10.5 | 0.10 | -9.4 | 0.43 | -8.7 | 0.48 |

– Continued on next page

Table 3.4 – continued from previous page

| ID | Δα ['] | Δδ ['] | M₃₃₀ | σ₃₃₀ | M₅₄₇ | σ₅₄₇ | M₆₀₆ | σ₆₀₆ | M₆₅₈ | σ₆₅₈ | M₈₁₄ | σ₈₁₄ | M₁₁₀ | σ₁₁₀ | M₁₆₀ | σ₁₆₀ |
|---|---|---|---|---|---|---|---|---|---|---|---|---|---|---|---|---|
| 33 | -4.9 | -0.5 | -9.2 | 0.06 | -10.2 | 0.08 | -10.2 | 0.05 | -10.2 | 0.66 | -9.9 | 0.14 | -9.0 | 0.54 | -8.5 | 0.54 |
| 34 | 3.4 | -1.4 | -10.0 | 0.03 | -10.9 | 0.05 | -11.1 | 0.03 | -12.0 | 0.24 | -10.9 | 0.08 | -10.0 | 0.29 | -8.7 | 0.37 |
| | 3.4 | -1.4 | -9.9 | 0.04 | -11.0 | 0.05 | -11.1 | 0.04 | -12.1 | 0.27 | -11.0 | 0.09 | -9.9 | 0.36 | -8.9 | 0.51 |
| 35* | -4.4 | -1.7 | ... | ... | ... | ... | ... | ... | ... | ... | ... | ... | -9.5 | 0.57 | -9.2 | 0.52 |
| 36* | -1.8 | -1.8 | ... | ... | ... | ... | ... | ... | ... | ... | ... | ... | -9.9 | 0.46 | -9.5 | 0.42 |
| 37* | 3.9 | -2.1 | ... | ... | ... | ... | ... | ... | ... | ... | ... | ... | -9.7 | 0.54 | -9.2 | 0.50 |
| 38 | 4.3 | -2.1 | -11.0 | 0.02 | -10.8 | 0.05 | -10.7 | 0.03 | -10.7 | 0.44 | -10.3 | 0.10 | -9.4 | 0.38 | -9.0 | 0.33 |
| | 4.3 | -2.1 | -11.0 | 0.02 | -11.0 | 0.05 | -10.9 | 0.04 | -11.1 | 0.44 | -10.6 | 0.10 | -10.1 | 0.32 | -9.9 | 0.28 |
| 39 | -1.5 | -2.5 | -9.6 | 0.05 | -9.8 | 0.08 | -9.7 | 0.06 | -10.1 | 0.57 | -10.2 | 0.10 | -10.0 | 0.28 | -10.0 | 0.21 |
| | -1.6 | -2.5 | -9.9 | 0.05 | -10.4 | 0.08 | -10.4 | 0.07 | -10.6 | 0.56 | -10.4 | 0.12 | -10.1 | 0.33 | -10.1 | 0.27 |
| 40 | 4.2 | -2.5 | -9.9 | 0.05 | -10.5 | 0.06 | -10.5 | 0.04 | -10.4 | 0.50 | -10.2 | 0.11 | -9.6 | 0.34 | -9.1 | 0.32 |
| 41 | -1.8 | -2.5 | -9.8 | 0.03 | -9.0 | 0.11 | -9.1 | 0.07 | -9.3 | 0.83 | -9.1 | 0.17 | -9.3 | 0.40 | -9.0 | 0.33 |
| | -1.8 | -2.5 | -10.2 | 0.04 | -10.3 | 0.09 | -10.2 | 0.08 | -10.2 | 0.65 | -10.0 | 0.15 | -9.9 | 0.36 | -9.8 | 0.32 |
| 42 | -1.5 | -2.6 | -9.6 | 0.04 | -9.5 | 0.09 | -9.3 | 0.07 | -10.0 | 0.60 | -8.7 | 0.21 | -8.8 | 0.48 | -8.4 | 0.43 |
| 43 | 2.8 | -2.7 | -10.3 | 0.03 | -10.4 | 0.06 | -10.3 | 0.04 | -10.2 | 0.56 | -9.9 | 0.12 | -8.6 | 0.54 | -7.8 | 0.59 |
| 44 | 1.4 | -2.9 | -9.5 | 0.06 | -9.6 | 0.14 | -9.4 | 0.14 | -9.4 | 0.94 | -9.3 | 0.22 | -8.8 | 0.65 | -8.4 | 0.64 |
| 45 | 3.3 | -3.0 | -10.1 | 0.03 | -9.9 | 0.07 | -9.8 | 0.05 | -10.1 | 0.59 | -9.6 | 0.13 | -8.9 | 0.47 | -8.5 | 0.43 |
| | 3.3 | -3.0 | -10.1 | 0.03 | -10.1 | 0.08 | -10.1 | 0.06 | -10.6 | 0.55 | -9.8 | 0.15 | ... | ... | ... | ... |
| 46 | -1.8 | -3.1 | -9.4 | 0.08 | -9.9 | 0.08 | -9.9 | 0.05 | -9.8 | 0.66 | -9.6 | 0.13 | -8.6 | 0.54 | -8.2 | 0.49 |
| 47 | 2.8 | -3.2 | -9.9 | 0.03 | -9.2 | 0.10 | -9.3 | 0.07 | -9.8 | 0.65 | -8.8 | 0.20 | -8.2 | 0.64 | -7.7 | 0.62 |
| | 2.8 | -3.2 | -10.5 | 0.03 | -10.2 | 0.09 | -10.1 | 0.09 | -11.0 | 0.46 | -9.6 | 0.20 | ... | ... | ... | ... |
| 48 | -0.6 | -3.2 | -10.1 | 0.03 | -10.3 | 0.09 | -10.1 | 0.09 | -10.2 | 0.66 | -9.6 | 0.20 | -9.2 | 0.57 | -9.0 | 0.52 |
| | -0.7 | -3.2 | -10.4 | 0.03 | -10.6 | 0.05 | -10.4 | 0.04 | -10.5 | 0.47 | -10.1 | 0.11 | -9.3 | 0.38 | -8.7 | 0.38 |
| 49 | 0.3 | -3.6 | -10.1 | 0.04 | -9.7 | 0.08 | -9.6 | 0.06 | -9.8 | 0.67 | -9.5 | 0.14 | -9.6 | 0.35 | -9.1 | 0.31 |
| | 0.2 | -3.5 | ... | ... | ... | ... | ... | ... | ... | ... | ... | ... | -10.2 | 0.37 | -9.1 | 0.57 |
| 50* | 1.6 | -3.5 | ... | ... | ... | ... | ... | ... | ... | ... | ... | ... | -10.5 | 0.35 | -10.1 | 0.32 |

– Continued on next page

Table 3.4 – continued from previous page

| ID | $\Delta\alpha$ ['] | $\Delta\delta$ ['] | $M_{330}$ | $\sigma_{330}$ | $M_{547}$ | $\sigma_{547}$ | $M_{606}$ | $\sigma_{606}$ | $M_{658}$ | $\sigma_{658}$ | $M_{814}$ | $\sigma_{814}$ | $M_{110}$ | $\sigma_{110}$ | $M_{160}$ | $\sigma_{160}$ |
|---|---|---|---|---|---|---|---|---|---|---|---|---|---|---|---|---|
| 51 | 2.7 | -3.6 | -11.6 | 0.01 | -11.2 | 0.04 | -11.0 | 0.03 | -11.2 | 0.35 | -10.6 | 0.09 | -9.3 | 0.39 | -8.1 | 0.51 |
|  | 2.7 | -3.6 | -11.4 | 0.01 | -11.2 | 0.05 | -11.1 | 0.04 | -11.4 | 0.38 | -10.5 | 0.11 | -9.9 | 0.37 | -8.9 | 0.57 |
| 52 | 2.3 | -3.7 | -9.7 | 0.07 | -10.1 | 0.12 | -10.1 | 0.12 | -10.9 | 0.49 | -9.7 | 0.21 | ... | ... | ... | ... |
| 53 | 0.2 | -3.8 | -9.3 | 0.06 | -10.0 | 0.07 | -9.9 | 0.05 | -10.0 | 0.60 | -10.1 | 0.11 | -9.9 | 0.30 | -9.6 | 0.26 |
|  | 0.1 | -3.8 | ... | ... | ... | ... | ... | ... | ... | ... | ... | ... | -11.4 | 0.20 | -10.9 | 0.19 |
| 54 | 1.1 | -3.8 | -9.6 | 0.06 | -9.9 | 0.08 | -9.8 | 0.05 | -10.1 | 0.57 | -9.9 | 0.12 | -9.1 | 0.43 | -8.6 | 0.40 |
| 55 | 1.1 | -4.1 | -9.6 | 0.07 | -9.9 | 0.08 | -9.9 | 0.05 | -11.1 | 0.37 | -9.5 | 0.15 | -8.8 | 0.49 | -8.2 | 0.49 |

**Notes:** Candidate star clusters detected with IRAF/DAOPHOT. Col (1) star cluster candidate ID; Col. (2)-(3) projected offset in arcseconds from the photometric nucleus (RA $20^h37^m14.123^s$, Dec $66°06'20.09''$); Col. (4)-(15) absolute magnitude (m-M=31.9), $M_x$, and error in magnitude, $\sigma_x$, in the F330W, F547M, F606W, F658N, F814W, F110W and F160W band *HST* images. The candidates with a star in column 1 could not be fitted with an acceptable star cluster model in (see §3.6).

## 3.6 Ages of the stellar populations in the ring

Determination the ages of the stars in the ring gives information on the age of the ring in NGC 6951 itself, since the star formation occurs in the circumnuclear ring.

### 3.6.1 Starclusters

The online Starburst99 (v6.0.2) code (Leitherer et al., 1999; Vázquez & Leitherer, 2005; Leitherer et al., 2010) was run to obtain model SEDs for star clusters of different ages. I assumed a fixed stellar mass of $10^5$ $M_\odot$, an instantaneous star formation event with a Kroupa IMF and Padova AGB solar metallicity stellar tracks. The model SEDs span the UV to the NIR in the time range of $10^4$ to $10^9$ years in steps of $2\times10^6$ years. I also include nebular emission in the model fluxes, which adds significant emission for young ages at, predominantly, the shorter wavelengths.

For comparison to our observed data points, these model spectra are weighted with a range of E(B-V) values ([0, 3] in 0.01 steps) and stellar masses ([$10^3$,$10^7$ $M_\odot$], in 0.2 dex steps). Mass scales linearly with luminosity and as such scales to the observed SED, independent of wavelength. A different distance modulus (31.2 instead of 31.9) would have a similar effect. To convert the color excess into an extinction curve the Calzetti extinction law (Calzetti et al., 2000) for starburst galaxies is used. The Starburst99 spectra so obtained are convolved with the different *HST* filter throughput curves, and converted to magnitudes. A $\chi^2$-fit is applied to each star cluster set of observed magnitudes. The lowest $\chi^2$ value is selected as the best fit to our data (Table 3.5).

Table 3.5 shows that the best fit ages for the star clusters span young (4 Myr) to intermediate (300 Myr) ages, with several older clusters present ($\geq$700 Myr). The stellar mass range of the star clusters is $\sim10^{4.0}$ to $\sim10^{6.8}$ $M_\odot$ and the E(B-V) color excess varies from 0 to 1.0 magnitudes, with most star clusters having a color excess of <0.6. The results of the star cluster fitting are also shown as a function of the azimuthal position in the ring in Figure 3.7. The four quadrants (SW, NW, NE and SE) should be visualized as overlaying compass points on the ring and are chosen with the contact points between gas/dust lanes of the large scale bar and the ring in mind. These points fall just inside the SW and NE quadrants. The rotation sense of the galaxy is clockwise, which corresponds to a decreasing angle. The results are averaged every 45° to detect any azimuthal trends in age, mass or color excess.

The star clusters have predominantly intermediate age and are massive, which explains why they are still detectable. From the left panel (age) in Fig. 3.7 it can be seen that the star cluster ages in the ring vary little, although they do drop in the SW and NE quadrant, before rising. It is not clear whether this trend could be a weak age gradient.

The color excess derived from the star cluster fitting (on average 0.4-0.6 mag) is somewhat larger than the color excess values obtained from the H$\alpha$/H$\beta$ and H$\alpha$/Pa$\alpha$ ratios presented in Sect. 3.4 (on average 0.4 mag). However, the Hydrogen emission and the star clusters do not come from the same physical locations. The extinction that is found for the star clusters is confined to the star cluster region, and can thus be higher than the more global extinction map derived from the Hydrogen lines.

Table 3.5: Star cluster ages, extinctions and masses

| ID | Age [Myr] | E(B-V) | log(Mass/M$_\odot$) | $\chi^2$/d.f. |
|----|-----------|--------|---------------------|---------------|
| 1  | 265 | 0.44 | 5.9 | 0.56 |
| 2  | 36  | 0.02 | 4.6 | 1.13 |
| 3  | 964 | 0.00 | 6.4 | 5.01 |
| 4  | 88  | 0.38 | 5.6 | 0.60 |
| 5  | 78  | 0.35 | 5.6 | 3.90 |
| 6  | 60  | 1.15 | 5.5 | 14.08 |
| 7  | 184 | 0.80 | 6.0 | 2.50 |
| 8  | 440 | 0.62 | 6.4 | 1.25 |
| 9  | 6   | 0.31 | 4.0 | 2.87 |
| 10 | 75  | 1.14 | 5.8 | 3.71 |
| 12 | 220 | 0.72 | 6.1 | 1.11 |
| 13 | 998 | 0.93 | 6.4 | 1.11 |
| 15 | 130 | 0.90 | 6.0 | 0.72 |
| 17 | 196 | 0.50 | 5.6 | 4.20 |
| 18 | 130 | 0.23 | 5.2 | 2.02 |
| 19 | 122 | 0.40 | 5.6 | 1.54 |
| 20 | 864 | 0.00 | 6.1 | 174.29 |
| 21 | 130 | 0.56 | 5.6 | 1.65 |
| 22 | 140 | 0.41 | 6.1 | 0.37 |
| 23 | 148 | 0.83 | 5.6 | 0.11 |
| 24 | 265 | 0.00 | 6.8 | 340.26 |
| 25 | 234 | 0.65 | 5.9 | 1.52 |
| 26 | 420 | 0.43 | 5.8 | 1.24 |
| 27 | 4   | 1.26 | 4.6 | 0.84 |
| 28 | 700 | 0.49 | 6.2 | 2.29 |
| 29 | 135 | 0.30 | 5.8 | 3.29 |
| 30 | 134 | 1.00 | 6.0 | 21.18 |
| 31 | 828 | 0.78 | 6.8 | 125.41 |
| 32 | 998 | 0.75 | 6.5 | 6.87 |
| 33 | 998 | 0.44 | 6.2 | 1.68 |
| 34 | 996 | 0.90 | 6.8 | 8.48 |
| 38 | 145 | 0.51 | 5.9 | 0.54 |
| 39 | 420 | 1.04 | 6.4 | 4.04 |
| 40 | 490 | 0.60 | 6.2 | 0.12 |
| 41 | 100 | 1.04 | 5.5 | 2.45 |
| 42 | 136 | 0.31 | 5.2 | 1.32 |
| 43 | 216 | 0.42 | 5.8 | 1.15 |
| 44 | 190 | 0.69 | 5.6 | 0.37 |
| 45 | 162 | 0.50 | 5.6 | 0.49 |
| 46 | 450 | 0.36 | 5.8 | 0.52 |
| 47 | 64  | 0.64 | 5.3 | 0.53 |
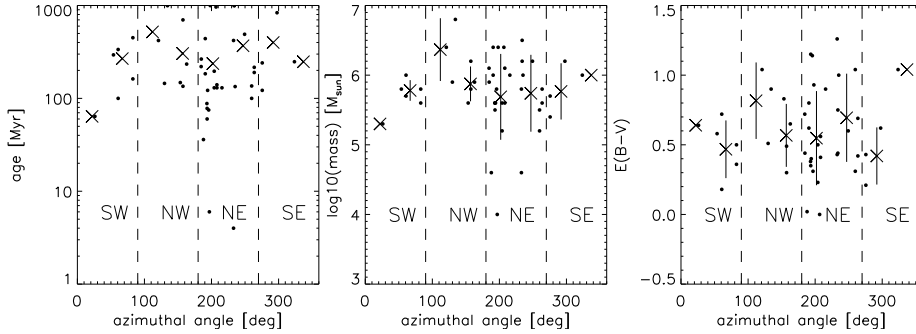
Figure 3.7: Results of the $\chi^2$ fitting. The four segments of the ring are indicated in the plots. From left to right are shown: stellar age, mass and color excess of the cluster. The individual results are averaged every 45°(crosses) and the variance is indicated with the error bars. The angle starts at the south point of the ring and is measured counter-clockwise.

Table 3.5 – continued from previous page

| ID | Age [Myr] | E(B-V) | log(Mass/M$_\odot$) | $\chi^2$/d.f. |
|----|-----------|--------|---------------------|---------------|
| 48 | 241 | 0.21 | 5.7 | 0.48 |
| 49 | 122 | 0.43 | 5.4 | 5.49 |
| 51 | 100 | 0.18 | 5.7 | 1.97 |
| 52 | 336 | 0.72 | 6.0 | 0.68 |
| 53 | 836 | 0.62 | 6.2 | 5.88 |
| 54 | 248 | 1.04 | 6.0 | 2.38 |
| 55 | 294 | 0.58 | 5.8 | 2.85 |

**Notes:** Results of the $\chi^2$ fitting of age (column 2), color excess (column 3) and mass (column 4) of the observed star clusters. Only those candidates which were successfully fitted are listed. The star cluster ID in column 1 is equal to that in Table 3.4.

## 3.6.2   Stellar populations from SAURON observations

The star clusters discussed above (§3.6.1) have ages of several hundred Myr and are visible due to their concentrated light. How do the star clusters relate to the underlying diffuse stellar populations in the ring? Does the ring have a different star formation history from the disk, or does the disk have similar stellar populations? With the SAURON IFU dataset these questions can be addressed.

Similar to the work by Stoklasová et al. (2009), a combination of 'young' and 'old' single stellar population (SSP) spectra is fit to each spaxel of the SAURON mosaic. The assumption here is that the stellar content in and around the ring can be approximated by a discrete combination of SSPs. Due to the continuous evolution of stars over time,

this assumption can usually be made, as long as the combination is chosen with care. SSP spectra were extracted from the MILES database (Sánchez-Blázquez et al., 2006; Falcón-Barroso et al., 2011) with a spectral resolution of $\sigma = 60$ km/s and spectral sampling of 1.15Å/pixel. Each spaxel was fit with a combination of 4 SSPs of different model ages (70.8Myr, 158.5Myr, 398.1Myr and 3.2Gyr). These 4 SSP spectra approximate well the full set (15 SSP spectra spanning 63 Myr to 13 Gyr) and were selected after minimization of results of mock data generated from the combination of the full set with added noise. In order to avoid an age-metallicity degeneracy, only solar metallicity SSP models were selected. The original fit of the SAURON data was more extensive, as a range of metallicities was used. The original fit shows that solar metallicity is a valid simplification.

The spectral fitting routine gives a (normalized) number weighted output of the SSPs used to fit the spectra at each spaxel. A 'bootstrap'-like method was used to obtain error estimates on the output. From the original fit of the data with a full set of SSP models, a measure for the fitting residual was obtained. This 'uncertainty', which is approximately 3% of the flux, was used to introduce random noise of this magnitude into the spectra. The fitting is iterated 30 times, each time introducing new random noise. Again based on mock data, the uncertainty of the number weighted fractional contribution by each SSP is estimated to be within 10%. We notice that if a large 'older' population is present, the fitting underestimates the 'young' fraction by several percent. The converse is not true. The results therefore remain sensitive to older populations also in regions dominated by 'young' stars. The normalized number weighted output is transformed into (again normalized) luminosity fractions, with the known luminosity of each SSP spectrum. The luminosity fractions can also be transformed into normalized stellar mass fractions, by use of the M/L ratio tabulated for each SSP spectrum. Finally, I multiply the normalized mass fractions with the stellar intensity at each spaxel (Fig. 3.3, top-left panel) to obtain an 'absolute' mass for each age bin. The resulting mass maps for different age bins are shown in Fig. 3.8.

As can be seen from Fig. 3.8 (results have been corrected for inclination), the ring is prominent in the 'young' bin, comprising about 30-40% of the mass at its galacto-centric distance. The contact-points between the large scale bar induced gas lanes and the ring stand out at the north and south positions in the ring. The mass of 'young' stars is highest at those positions. In the 'old' bin the opposite picture is observed; as good as no 'old' stellar population is present in the ring, the 'old' stars are distributed in a typical bulge-like profile. Significant mass in 'intermediate' age stellar populations is found at the inner edge of the ring.

## 3.7   Discussion

### 3.7.1   Star formation signatures in the ring

By combining the results from the star cluster analysis and the underlying stellar 'field' population through the IFU fitting, the stellar content in and around the circumnuclear ring has been fully constrained. What does it say about the manner in which star formation proceeds in this circumnuclear ring? Is there an azimuthal age gradient, as in
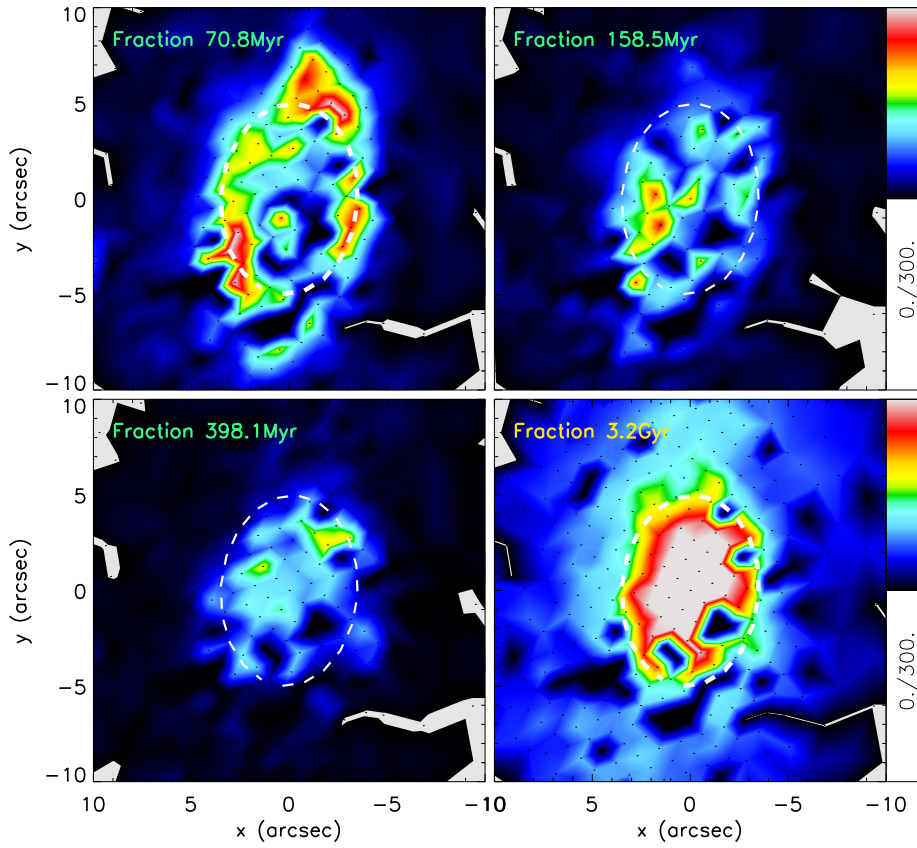
Figure 3.8: The stellar 'mass' maps by age bin obtained by fitting the SAURON IFU dataset with a combination of 4 SSP spectra. The age of each SSP is given above the panel. The maps are corrected for inclination. The approximate location (a∼ 5″, b∼ 3.5″) of the ring is indicated by the dashed ellipse. The 'mass' uncertainty is within 10%.
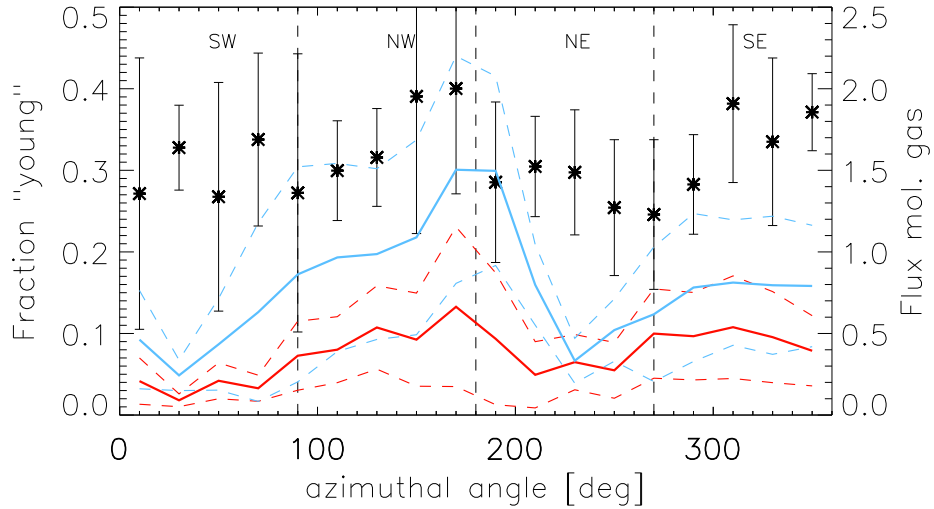
Figure 3.9: Azimuthal mass fraction of young stars (asterisk), combined with the azimuthal intensity distribution of CO(2-1) (red line, dashed ±1 standard deviation) and HCN(1-0) emission (blue line, dashed ±1 standard deviation). The angle 0 corresponds to the south, angle increases counter-clockwise.

the 'pearls-on-a-string' scenario proposed by Böker et al. (2008), or has star formation resulted in a homogeneous ('popcorn') stellar age distribution (Elmegreen, 1994)?

The recent star formation episodes are concentrated in the ring region (see Fig. 3.8). This is in accordance with my opening statement in this chapter that the circumnuclear ring is the gas reservoir for the circumnuclear region. Indeed, the average age of the star clusters in the ring is young; 200-300 Myr. The 'old' stellar bin in Fig. 3.8 mainly shows a bulge-like profile, with no additional mass at the ring radius itself.

The distribution of the 'young' stars is not uniform throughout the ring. The relation between the contact points and star formation is the main observable for the 'pearls-on-a-string' scenario for star formation. The locations with the highest mass in 'young' stars are close to the gas inflow points, the contact points. This is a point in favor of the 'pearls-on-a-string' scenario.

In Fig. 3.9 I further plot the intensity distributions of the molecular gas tracers CO(2-1) and HCN(1-0) as a function of azimuthal angle in the ring. The azimuthal distribution of the 'young' stellar mass fraction (in percentage of the total mass at each position) is also plotted there. The highest concentrations of molecular gas are close to the contact points in the north ($\phi \sim 180°$) and to a lesser extent in the south ($\phi \sim 350°$). The variations are especially pronounced in the HCN distribution. The fraction of the total mass in 'young' stars by comparison shows much less variation.

The highest concentrations of 'young' stars are found in the NW and SE segments of this figure. The wave pattern of the large scale stellar bar is slower (28.9 km/s/kpc pattern speed) than the stellar and gas velocity ($\sim 150$ km/s) at the circumnuclear ring radius (580 pc). This means that the overdensity points will move counter-clockwise in

the inertial frame of the galaxy (galaxy rotation is clockwise). If stars form preferentially at or near the overdensity points, the stars and gas will move faster and out of the overdensity region. The fraction of 'young' stellar mass must thus be higher in front of the overdensity region (in Fig. 3.9 'in front of' equals at *lower* azimuthal angle). The offset between the highest fractions of 'young' stars and the peak in HCN in the north is $\sim 20°$. Approximately 1.5 Myr would be needed to travel 20° at the ring radius.

A half (two-fold symmetry) orbit of the bar wave pattern in the ring takes approximately 100 Myr, and stars that have formed at those locations will make 5 full orbits around the ring before the pattern rotation is complete. Hence, any age signature will be severely smeared within that 100 Myr pattern time, and erase the 'pearls-on-a-string' scenario in favor of the 'popcorn' one. The small indications of young fractions I find are thus all we can detect.

## 3.7.2 Age of the circumnuclear ring

The stellar age content of the ring can assist in the determination of the age of the ring as a dynamical structure. Taking together the stellar ages, gas inflow rate and dynamical times allows both a minimum and maximum age to be constrained.

The lack of extra mass in the ring in the old stellar bin in Fig. 3.8 suggests that the ring cannot be older than 3 Gyr. The average age of the star clusters is 200-300 Myr with some older (up to 1 Gyr). In the previous chapter, I already inferred a minimum age of the large scale stellar bar and thus the ring of 1.1 Gyr, based on mass inflow and total molecular gas mass.

The inflow rate determined in the previous chapter (Van der Laan et al., 2011) was $2.0 M_\odot$/yr. The total mass in the star clusters I found is $\sim 6{\times}10^7 M_\odot$. A star (cluster) formation rate history, based on the star cluster results, is given in Fig. 3.10. The highest SFR was reached 800 Myr ago, after which the ring was quiescent for 300 Myr. Star formation has started again in the last 400 Myr. Over 1 Gyr (the oldest measured star cluster age), the average star formation rate was $\sim 0.06 M_\odot$/yr. A star formation efficiency of a few percent is entirely plausible. That implies that the current inflow rate is a good estimate of the average inflow rate over the last 1 Gyr, even though the star formation rate was variable, and that the previously inferred minimum age of 1.1 Gyr, based on that inflow rate, is still plausible. If the star formation efficiency is higher, a lower inflow rate would suffice and the minimum age would be higher.

The fraction of angular momentum lost in gas per orbit, dL/L, is 0.2-0.4 (Haan et al., 2009), which means gas needs at least 3-5 orbits to settle on the ring, which equals ~200 Myr (orbit times are larger at larger radii).

Like I said above, the oldest likely age for the ring is 3 Gyr, given the lack of a significant number of 'old' age stars from the analysis in Sect. 3.6.2. If the ring is 3 Gyr, that implies that the ring was quietly accumulating gas for up to 2 Gyr before star formation in the ring commenced. Assuming a constant mass inflow of $2.0 M_\odot$/yr and a ring of 600 pc (5″) radius and 100 pc (1″) width, that would imply an absurdly high molecular gas surface density of $11.000 \, M_\odot/pc^2$ at the onset of star formation. That is much higher than the average $100 \, M_\odot/pc^2$ value of most giant molecular clouds (e.g. Bigiel et al., 2008). To reach an average surface density of $100 \, M_\odot/pc^2$ would thus only take 19 Myr.
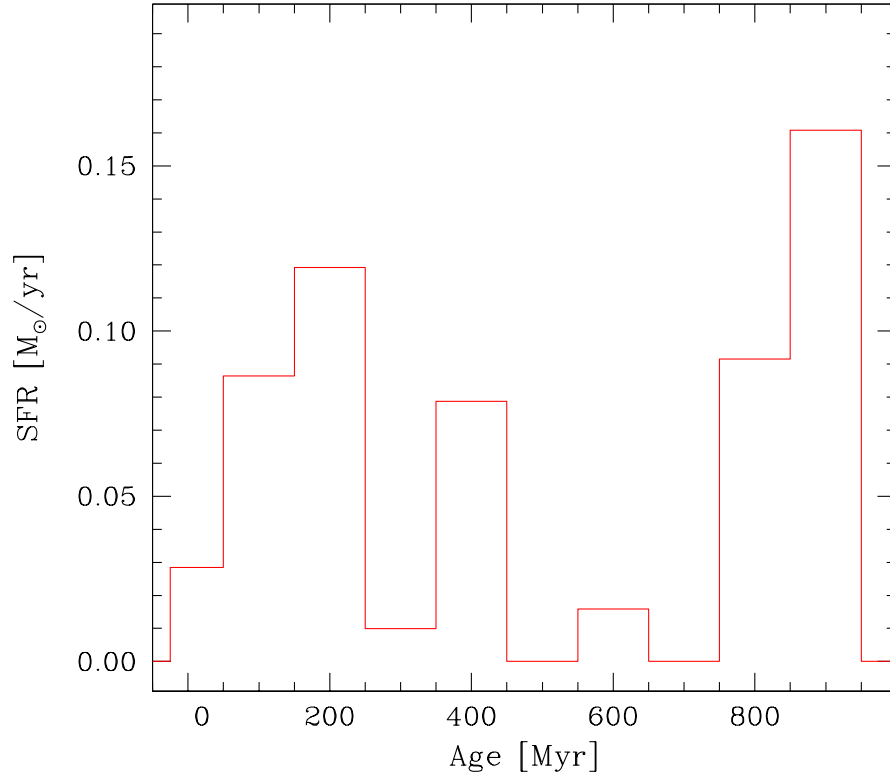
Figure 3.10: Star formation rate history in the circumnuclear ring. The masses of the star clusters are grouped in 100 Myr age bins and divided by the width of the age bin.

The current age of the circumnuclear ring is therefore most likely between 1.0 Gyr and 1.5 Gyr.

## 3.8  Summary

In this chapter the properties of the stellar populations of the circumnuclear ring in NGC 6951 were investigated. The goals were to estimate the age of the circumnuclear ring itself, to determine the age of the stellar population(s) present in the circumnuclear ring, and to determine whether the 'popcorn' or 'pearls-on-a-string' scenario holds true for the nature of star formation in the circumnuclear ring. The main results can be summarized as follows:

The ring is most likely between 1.0 Gyr and 1.5 Gyr old. it has a stellar population distinct from the rest of the circumnuclear region that was formed over that time frame. The maximum possible age for the ring is 3 Gyr. However, it is very unlikely that the ring has been in place for that long without forming stars for its first 1.5 Gyr.

Analysis of the general stellar content of the ring, by means of the SAURON mosaic, shows that 30-40% of the stellar mass in the ring is from 'young' (<100 Myr) stars. The largest fractions are found near the contact points that link the ring with the large-scale stellar bar induced gas lanes.

The majority of the star clusters in the circumnuclear ring have intermediate age. The youngest star clusters (~100 Myr), when the results are averaged over 45° intervals, are in the north and south, close to the contact points were gas flows onto the ring. Such a connection is indicative of the 'pearls-on-a-string' scenario for star formation in circumnuclear rings. However, the dynamical time of the ring is short; it takes only 24 Myr for a star cluster to completely one rotation of the ring, while the age gradient can only be renewed every 100 Myr. Therefore I do not find definite evidence of the 'pearls-on-a-string' scenario in the circumnuclear ring of NGC 6951.

# 4

# Double rings in NGC 5248

**Motivation:** In this chapter I turn my attention to another nearby barred galaxy; NGC 5248. Many of the global properties of this galaxy are similar to those of NGC 6951, but its circumnuclear region is very different. NGC 5248 has two circumnuclear star forming rings, one inside the other, at 100 pc and 370 pc radius from the nucleus, respectively. The stars in the inner ring are also believed to be younger (Maoz et al., 2001; Böker et al., 2008). Gas must thus be able to move inward past the outer circumnuclear ring. What does this imply for our understanding of circumnuclear rings as markers of effective gas barriers?

I present new CO(2-1) observations, from the PdBI and IRAM 30m telescope (providing short spacing corrections). These observations have subarcsecond resolution, and are the first observations of the molecular gas distribution in which the inner circumnuclear ring is resolved. The first goal in this chapter is to understand the gas dynamics in and around both circumnuclear rings. To this end I combine the new CO(2-1) data with archival CO(1-0) and HI observations and study the non-circular gas motions in the circumnuclear region.

The second goal in this chapter is to study the ages of the stellar populations in both rings in the same manner as I did for the circumnuclear star forming ring of NGC 6951 (Chapter 3). The results I obtain, suggest that the circumuclear gas distribution in the inner 300 pc of NGC 5248 is shaped by a dynamical component other than the large scale stellar bar.

## 4.1  Introduction

Gas inflow from kiloparsec scales all the way to the nucleus is very difficult to achieve in single bar galaxies (e.g. García-Burillo et al., 2005; Combes, 2008). Gravitational torques from a large scale stellar bar become much weaker due to the increased mass influence of the stellar bulge with decreasing radius. Englmaier & Shlosman (2000) investigated the conditions under which nuclear spirals, which are connected to the large scale spiral structure within a large scale bar region can exist to small radii and effect this inflow. This work and Maciejewski (2004b) showed that the extent of nuclear spirals mostly depends on the gravitational potential (i.e. the mass of the large scale bar compared to the mass of the stellar bulge) and the sound speed of the gas. When gas

is dynamically warm, the pitch angle of the large scale spiral will be large, resulting in a nuclear spiral which extents all the way towards the nucleus. When gas is cold, the pitch angle is small, and the large scale spiral will end in a ring. These circumnuclear rings act as gas reservoirs for the gas arriving from larger radii.

When a spiral cannot reach the nucleus, a nested bar system, where one bar exists within another, might help funnel gas further inward. This idea was first proposed by Shlosman et al. (1989), and was followed up by many numerical studies (e.g. Maciejewski et al., 2002; Englmaier & Shlosman, 2004; Maciejewski & Small, 2010). One of the constraints on a nested bar system being stable is that there must be overlap between the resonances of both bars. This overlap is achieved by decoupling the inner bar from the pattern speed of the large scale bar. However, gas flow into the region of influence of the inner bar is then not always possible and depends on the periodic alignment of the two bars. Actually, the overlap of resonances is mandatory for any system of co-existing non-axisymmetric patterns to be stable. Hopkins & Quataert (2010) have shown in simulations that m=1 modes in the central regions could also lead to nuclear feeding and that nested bars are not necessary.

Here I study the nearby barred galaxy NGC 5248, for which atomic and molecular gas has been detected at radii of less than 100 pc from the nucleus (Laine et al., 2001; Jogee et al., 2002b; Helfer et al., 2003). One large scale stellar bar has been confirmed in NGC 5248 by Jogee et al. (2002a), with a semi-major axis is 5.9 kpc (95″ ). However, this galaxy has 2 circumnuclear rings; at 100 pc (1.5″ ) and 370 pc (6″ ) radii. A single ring can easily be explained in the frame work of the large scale stellar bar. Two rings is more problematic. If the inner and the outer ring both harbor gas reservoirs filled by the large scale bar, why is there the gap between them?

Both rings show current star formation, with some indication that the inner ring hosts younger stars (Maoz et al., 2001; Böker et al., 2008). If the stars in the inner ring are younger, than gas is likely flowing from the outer to the inner ring. The dynamics of the gas in this region are therefore of particular interest to understand circumnuclear rings and gas flow in large scale stellar bars.

NGC 5248 is a nearby SAB(rs)bc galaxy at a distance of 12.7 Mpc (Tully et al., 2009). Its global properties are listed in Table 4.1. The two circumnuclear gas rings are at radii of 100 pc and 370 pc from the nucleus. Gas observations include HI observations of the full disk by Haan et al. (2008, 2009). Earlier work on the molecular gas distribution in NGC 5248 has been done by the BIMA SONG survey (Helfer et al., 2003) and by Jogee et al. (2002b). They both observed the CO(1-0) line transition. The BIMA SONG survey has a lower spatial resolution (6″), but covers a large extent of the galaxy (12 kpc by 12 kpc). Jogee et al. (2002b) cover the inner 4 kpc with the OVRO telescope, at higher resolution (1.9″× 1.4″). Whereas the outer ring is well resolved in this latter study, the inner one is not.

In this chapter new observations of the CO(2-1) line transition are presented (§4.2), which have subarcsecond spatial resolution and resolve the inner circumnuclear ring in molecular gas for the first time. In §4.3, morphology, non-circular motions in the gas, and resonance radii in the disk are determined using the HI (from Haan et al., 2008, 2009) and CO observations. In §4.4 I revisit the finding that the inner circumnuclear ring hosts younger stars, as well as make a thorough investigation of the stellar ages in both rings. Work by Maoz et al. (2001) has previously identified and age dated

Table 4.1: Properties of NGC 5248

| Parameter | Value | Reference |
|---|---|---|
| Type | SAB(rs)bc | (1) |
| Photometric Center | | |
|   RA (J2000) | $13^h37^m32.024^s$ | (2) |
|   Dec (J2000) | $08°53'06.64''$ | (2) |
| Inclination Angle | $43.1°$ | (3,4) |
| Position Angle | $115°$ | (3,4) |
| Adopted Distance | 12.7 Mpc | (5) |
| Stellar bar PA | $135°$ | (6) |
| Systemic velocity | $1153$ km s$^{-1}$ | (3,4) |
| Mass H$_2$ (r<1.2 kpc) | $4.7 \times 10^8$ M$_\odot$ | (4) |

**References:** (1) de Vaucouleurs et al. (1991), (2) NED (SDSS6), (3) Haan et al. (2008), (4) this work, (5) Tully et al. (2009), (6) Jogee et al. (2002a)

star clusters observed from *HST* optical images, however I repeat the age dating with updated stellar evolution models. I add SAURON IFU data to analyze the overall contribution of different stellar populations. The gas dynamics and the star formation (history) in and between these two rings point towards a second dynamical component in NGC 5248. I discuss this scenario and the evidence for it in §4.5. A summary is presented in §4.6.

## 4.2 Observations and data reduction

### 4.2.1 IRAM PdBI + 30M CO(2-1) data

IRAM PdBI observations in ABCD configuration were carried out between January 2009 and December 2010 using the full 6-antenna array. The correlator was centered at 229.6547GHz, corresponding to a redshifted CO(2-1) line at heliocentric velocity of 1153 km s$^{-1}$. The flux calibration used quasars 1354+195, 0923+392 and/or MWC349. During the observations in D-array, the WIDEX correlator was working in parallel with the 'narrow-band' correlator, and simultaneously recorded the full 4GHz bandwidth. All data were reduced using standard routines in the GILDAS/CLIC software package[1].

30m observations for the central 44″ by 44″ were obtained with the IRAM 30m telescope on July 13 and 14, 2011. The 1 mm receivers were tuned to 229.6553GHz. A bandwidth of 640 MHz was covered by 512 channels with a width of 1.25 MHz (2.6 km s$^{-1}$ at 1 mm). The spacing between individual grid points was 4″. Typical system temperatures during the observations were 360 K for the 1mm receivers. The data reduction was done using the GILDAS/CLASS software package.

The 30m observations were used to compute the short spacing correction (SSC) and recover the large-scale low-level flux. The 30m observations were reprojected to the field center and central frequency of the PdBI observations. The bandwidth coverage

---

[1]http://www.iram.fr/IRAMFR/GILDAS
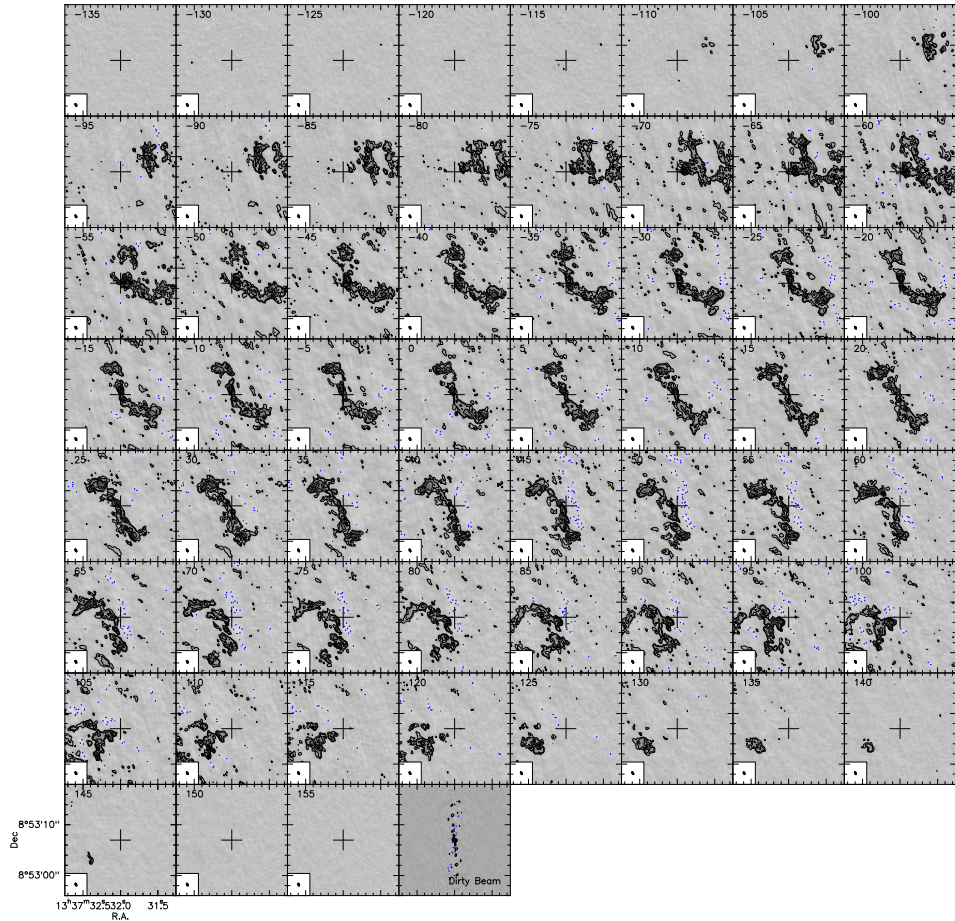
Figure 4.1: Channel maps of the uniform weighted $^{12}$CO(2-1) SSC data cube. The size of the channel maps is 22″ by 22″, the size of the primary beam of the PdBI observations. The contours are -3$\sigma$, 3$\sigma$, 5$\sigma$, 10$\sigma$, 15$\sigma$ and 25$\sigma$, with 1$\sigma$ = 2.8 mJy beam$^{-1}$. The velocity relative to systemic velocity of the galaxy ($v_{sys}$=1153 km s$^{-1}$) is indicated in the upper left corner. The phase center of the observations is indicated by a cross in each channel map. The synthesized beam (0.62″ by 0.34″) is given in the lower left corner of each channel and the dirty beam is shown in the last lower right panel.

Table 4.2: Overview of PdBI+30m CO(2-1) and 1mm continuum data

| Weighting | Beam size ($'' \times ''$) | PA (°) | rms (mJy/beam) |
|---|---|---|---|
| CO(2-1) uniform | 0.62×0.34 | 27.3 | 2.8 |
| 1mm cont. | 2.4×1.32 | 18.8 | 1.8 |

**Notes:** The CO(2-1) cube was short-spacing corrected. The 1 mm cube was not.

of the 30m data was resampled to match the velocity axis of the interferometric observations. A combined data cube was produced using the task 'UV-short' in GILDAS. The dirty beam is extended north-south due to the low declination of the source, which prevents a more circular population of the $(u, v)$-plane. The final clean beam size is $0.62'' \times 0.34''$, with a PA of $27.3°$.

A cleaned data cube was produced using uniform weighting with the GILDAS/ MAPPING software package. The beam size/resolution of the uniform CO(2-1) data is given in Table 4.2, as well as the rms noise per channel. The data cube has 1024 by 1024 pixels, with a pixel scale of $0.1''$/pixel and velocity bins of $5\,\mathrm{km\,s^{-1}}$. CLEANing was done down to the $2\sigma$ noise level with the assistance of individual polygons defined for each channel with line emission present.

The channel maps for the uniform weighting are presented in Fig. 4.1. CO(2-1) emission is seen in the channels [-130:145] $\mathrm{km\,s^{-1}}$ relative to the 1153 $\mathrm{km\,s^{-1}}$ systemic velocity. In the individual channels the emission is extended from north-east to south-west, in accordance with the position angle of 115° for this galaxy (see Table 4.1).

The new WIDEX correlator at the PdBI allows for 1 mm continuum observation as a free addition to the CO observations. The WIDEX data were collapsed over their full spectral range, excluding the CO(2-1) emission line region. The resulting 1 mm continuum map has 128x128 pixels, with a pixel scale of $0.3''$/pixel. The 1 mm continuum distribution, as shown in Fig. 4.2 has a beam size of 2.4″ by 1.3″ with a PA of 18.8°. The highest emission peak reaches a $13\sigma$ (23.9 mJy/beam) intensity.

## 4.2.2 Ancillary archival data

For this study I have also made use of the following data sets that have been presented in the literature before.

### SAURON IFU data

NGC 5248 was observed with the SAURON instrument at the William Herschel Telescope (Bacon et al., 2001) in March 2004 and maps were first presented in Dumas et al. (2007). The FoV of the SAURON IFU instrument is 33″ × 41″ with square 0.94″ lenses. The final data cube is built up out of 5 individual 30 min exposures and has 0.8″×0.8″ spaxels. The spectral range covered is 4825 Å - 5280 Å, with a 4.2 Å resolution and spectral sampling of 1.15 Å. Data reduction and flux calibration were done with the dedicated XSauron software and is explained in detail in Dumas et al. (2007).

The spectral range 4825 Å -5280 Å covers the stellar absorption lines H$\beta$, Fe5015, Mg$\beta$ and Fe5270, as well as the gaseous emission lines, H$\beta$ and the doublets [OIII] ($\lambda$
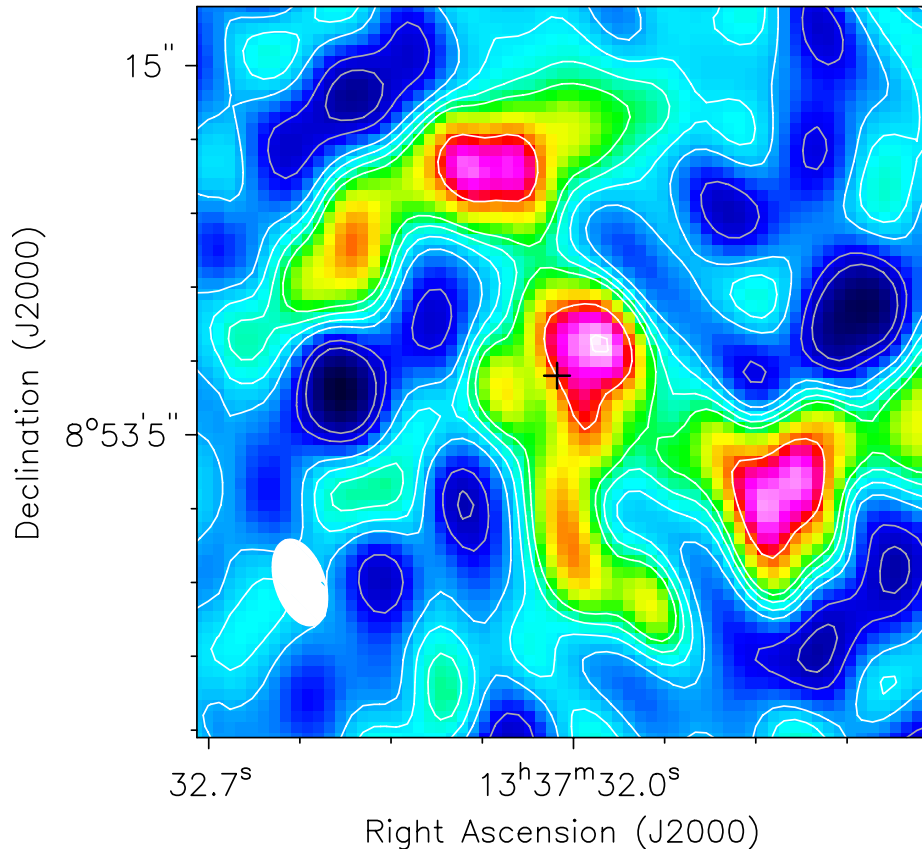
Figure 4.2: 1 mm continuum as observed with the PdBI Widex instrument. The telescope was used in D configuration. Contours give the $-3\sigma$, $-2\sigma$, 0, $2\sigma$, $3\sigma$ and then multiples of $5\sigma$ flux levels. The galaxy center is marked by a black cross. The beam size is $2.4'' \times 1.32''$ and is indicated in the bottom-left corner. Pixel scale is $0.30''$.
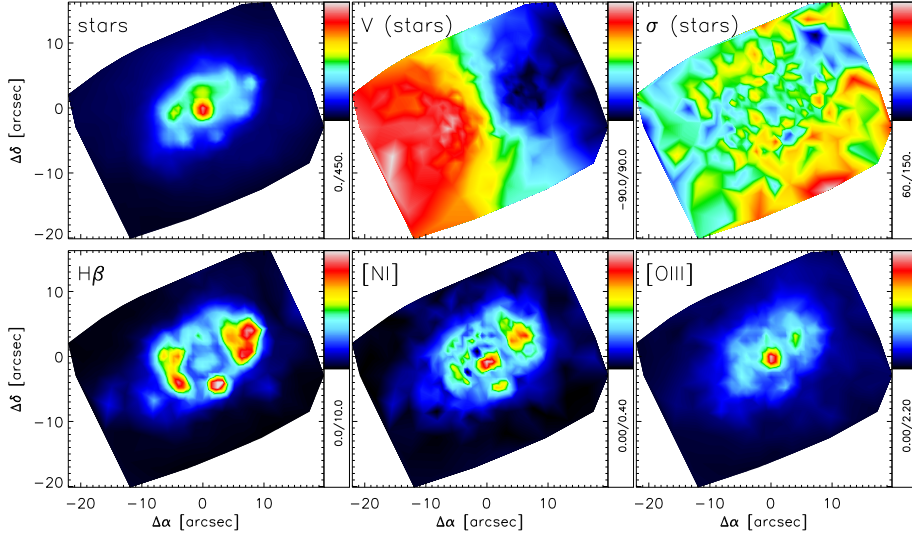
Figure 4.3: *Top:* SAURON maps of the stellar light distribution, velocity field and dispersion. *Bottom:* intensity distributions of the emission lines in the SAURON spectral range; Hβ, [NI] and [OIII]. The maps are oriented with north pointing up, and east to the left.

(4959,5007) Å) and [NI] ($\lambda$ (5200,5202) Å). We fit each spaxel with a combination of single-stellar population spectra (SSP) and gaussian emission line profiles using the IDL-based routines pPXF (Cappellari & Emsellem, 2004; Emsellem et al., 2004) and GANDALF (Sarzi et al., 2006). The combined use of pPXF and GANDALF takes into account the fact that Hβ is present both in absorption and emission.

Several of the resulting maps are shown in Fig. 4.3. The top row in this figure shows the stellar light distribution, velocity field and velocity dispersion. The nebular emission lines are clearly strongest in the outer circumnuclear ring. Some emission is also seen from the inner 2″, but at the resolution of these data it is impossible to distinguish between the nucleus and the inner circumnuclear ring. The positions of highest intensity line emission and stellar light appear anti-correlated with each other in the outer circumnuclear ring. The maps I obtain are nearly identical to the ones presented by Dumas et al. (2007).

**HI**

NGC 5248 was observed with the VLA in C and D array as part of a larger survey (Haan et al., 2008) in 2003 and 2004. I refer to that work for details of the observations and data reduction. The robust weighted data cube used here has a spatial resolution of 20″, with a 2″ pixel size and a FoV of 34′× 34′. The total HI flux measured in these observations is 81.3 Jy km s$^{-1}$, which is equal to a total atomic gas mass of $4.32 \times 10^9 M_\odot$.

The HI distribution follows the large scale stellar bar and the spiral arms at larger

radii. The HI intensity is somewhat higher within the bar radius, but has no pronounced peak at the center.

**BIMA SONG CO(1-0)**

The BIMA SONG survey (Helfer et al., 2003) was designed to systematically observe the CO(1-0) distribution in 44 nearby galaxies. NGC 5248 was observed in May of 1999. The total FoV of these data are $194'' \times 194''$ and the data have a pixel scale of $6''$ and are short-spacing corrected. The resulting data cube and moment maps are available on-line.

Helfer et al. (2003) show that the CO(1-0) distribution increases in the center, with an 'S'-like shape in the inner $20''$ (1.2 kpc) that may indicate two spiral arms at higher resolution. The CO(1-0) emission extends out to $\sim 1'$ (3 kpc) from the nucleus. The large scale bar dust lanes are also partly traced by low-level CO(1-0) emission.

**HST**

In Maoz et al. (2001) a thorough detection of star clusters in the circumnuclear ring of NGC 5248 was preformed. The Maoz et al. (2001) work was based on HST observations in 5 filters; F220W, F336W, F547M, F814W and F160W. A table with the observed fluxes for each star cluster in each band is electronically available with the paper. I refer to that work for details on the data reduction and cluster finding. Total fluxes were derived for 507 possible star clusters in one or more filter bands.

## 4.3 NGC 5248's central structures

In preparation for the coming analysis of the gaseous and stellar content of the circumnuclear region in NGC 5248, here follows a short summary of the known structures in the circumnuclear region of this galaxy.

A large scale stellar bar was reported by Jogee et al. (2002a), with a semi-major axis length of 5.9 kpc ($95''$), a PA of $135°$ and a deprojected ellipticity of 0.44. In broad-band B and I-K images two spiral arms/dust lanes are seen, that lie at the leading edges of this large scale stellar bar (Figure 2 and 4a of Jogee et al., 2002b). The CO(1-0) distribution mapped by BIMA SONG also shows some low-level CO emission in these spiral arms (Helfer et al., 2003). The CO intensity increases at smaller radii, and the CO distribution in the central region is again dominated by two spiral arms, as shown in the CO(1-0) maps by Jogee et al. (2002b). The alignment/orientation of these molecular spiral arms is similar to the larger stellar and dust spiral arms. Jogee et al. (2002b) argue that both the molecular gas spiral arms, and the larger star and dust spiral arms trace the same density wave, that thus winds up over $2\pi$, from the outer edge of the large scale bar at 5.9 kpc to the center. However, this scenario does not account for the inner circumnuclear ring.

Within the central 2 kpc, two circumnuclear star forming rings are detected in H$\alpha$ emission (Maoz et al., 2001). The outer one at $6''$ is very broad, with a radius-to-width ratio of $\sim 2$. The afore mentioned CO spiral arms are at this radius, and are thus co-spatial with (part of) the outer circumnuclear ring. The inner circumnuclear ring at

1.5″ is much narrower. In the circumnuclear region all Hα emission arises from these two rings.

There is evidence for asymmetric distributions of material at and within the outer circumnuclear ring. Laine et al. (1999) have detected a single nuclear dust spiral that extends from 1″ distance from the nucleus out to 4″ in J-, H-, and K-band images. Jogee et al. (2002b) and Böker et al. (2008) both comment on excess light north of the nucleus in the K band. The Sauron map of stellar light presented here (Fig. 4.3) shows the same feature. The J-K dust map shown in Fig. 4b of Jogee et al. (2002b) also shows the presence of much higher extinction in the south.

An oval light distribution in the center of NGC 5248, based on K-band observations, was noted by Jogee et al. (2002b), and corroborated by Böker et al. (2008). The spatial scale of this feature was estimated to be 3″, with a PA of 110-120° and a deprojected ellipticity of 0.1-0.2. Jogee et al. (2002b) speculate that it is a "disk-like component, a late-type bulge, or an unresolved nuclear bar". Analysis of the light profile of this oval in a Spitzer 3.6 $\mu$m image, gives a Sersic-index of 2, just between a disk and a bar.

The circumnuclear region of NGC 5248 thus contains, an m=2 spiral structure, driven by the large scale stellar bar, that extends inwards down to at least the outer circumnuclear ring, possibly further, two circumnuclear rings, a single dust spiral arm between the two rings, an asymmetric distribution of stellar flux and dust and a 3″ oval light distribution at the center.

## 4.4 Molecular gas in the center of NGC 5248

The existence of double circumnuclear rings in NGC 5248 is difficult to relate to a single large scale stellar bar. The morphology and kinematics of the gas in the circumnuclear region will show the formation relation (if any) between between the two rings, the large scale stellar bar and the other structures in the circumnuclear region.

### 4.4.1 CO(2-1) morphology

The distribution of the $^{12}$CO(2-1) line emitting gas is shown in Figure 4.4. At 6″ from the nucleus two partial spiral arms are seen in the north and south. The location of the spiral arms is co-spatial with the location of the outer circumnuclear star forming ring. Morphologically, these two arms either continue to spiral inwards for another 180° or two fractured, lower intensity arms are formed east and west of the nucleus. At 1.5″ radius from the center we find a partial ring. This location is consistent with the location of the inner circumnuclear star forming ring. The CO(2-1) intensity reaches the highest values in this ring.

In total I measure an integrated flux of 684 Jy km s$^{-1}$ within the central 10″ radius, of which 177 Jy km s$^{-1}$ (∼26%) are within the central 3″ radius (the inner ring). This is equal to a gas mass of 4.0×10$^8 M_\odot$ and 1.0×10$^8 M_\odot$, respectively. In this calculation I correct for the helium abundance, and assume an I$_{CO(2-1)}$/I$_{CO(1-0)}$ ratio of 0.89[2] (Braine et al., 1993). We also assume the Galactic X$_{CO}$ value of 2.2e20 cm$^{-2}$ [K km s$^{-1}$]$^{-1}$

---

[2]This value might be higher in the centers of galaxies, but I cannot measure it, therefore I assume this constant value. A ratio higher by a factor $x$, would lower the derived gas mass by a factor $x$.

(Solomon & Barrett, 1991). Table 4.1 summarizes these and other relevant numbers for NGC 5248.

Comparison between the CO(2-1) intensity distribution presented here and the CO(1-0) presented in Jogee et al. (2002b) shows that CO(1-0) and CO(2-1) emission is present in the two spiral arms that trace the outer circumnuclear star forming ring in the north and south. Inside the outer ring radius the distributions differ. The CO(1-0) emission is lower than in the spiral arms, while the CO(2-1) emission is highest in this region. This could indicate that CO(2-1) is preferentially excited over CO(1-0) at these smaller radii (this would imply also a different $I_{CO(2-1)}/I_{CO(1-0)}$ ratio, e.g. Armour & Ballantyne, 2012). The morphology of the CO(1-0) and CO(2-1) emission within the outer ring radius is also different. The CO(1-0) emission is distributed in an elongated structure parallel to the CO spiral arms that were co-spatial with the outer ring, with emission peaks at the inner circumnuclear ring (east and west) and extending low-level emission spurs at the outer circumnuclear ring, where as the CO(2-1) emission shows low intensity spiral arms in the east and west at the outer ring radius and the distinct structure of the inner circumnuclear ring in the center. The different appearance in CO(1-0) and CO(2-1) line emission likely reflects changes in the excitation conditions from the outer to the inner ring, with young star formation, i.e. heating, being a very likely explanation.

## 4.4.2 CO(2-1) kinematics

The first (velocity field) and second (velocity dispersion) moment maps of the CO(2-1) data are shown in Fig. 4.5. The velocity field of the CO(2-1) emitting gas is dominated by circular velocity; it shows the clear "spider diagram" contours of an inclined rotating disk. The dynamical center is slightly offset ($\Delta x$=-0.4″, $\Delta y$=0.1″) from the photometric center. The shape of the velocity field of the CO(2-1) emitting gas and the stellar velocity field of the SAURON observations are very similar. The CO(2-1) velocity range is larger than the SAURON stellar velocity range, but the velocity dispersion is larger in the stars. This implies that, the molecular gas is kinematically colder ($\sigma$ ~15-20 km s$^{-1}$) than the stars and shows more ordered motion.

Given that spiral arms are usually found at the leading side of a bar and that the blue-shifted velocities are in the west, NGC 5248 must be rotating clockwise and thus the south-western part of NGC 5248 is the near side of the galaxy, and the north-eastern part the far side. The orientation is important to be able to determine whether non-circular motions imply in- or out-flow later on.

The highest CO(2-1) velocity dispersions (15-20 km s$^{-1}$) are seen in the spiral arms at 6″ distance from the nucleus and in the inner 4″ (i.e. the inner ring region). Given the location, the higher velocity dispersions could be indicative of non-circular motions caused by shocks or shear in the gas.

As a first investigation of the non-circular motion two position-velocity (pv) diagrams were extracted from the CO(2-1) data cube; one along the major kinematic axis (PA 115° ) and one along the minor kinematic axis (PA 25° ); see Fig. 4.6. The pv-diagram along the major axis shows evidence for solid body rotation for r<2″ (130 pc). The linear pv-distribution along the major kinematic axis indicates that gas along this line is rotating with a single angular velocity. The turn-over of the velocity at larger
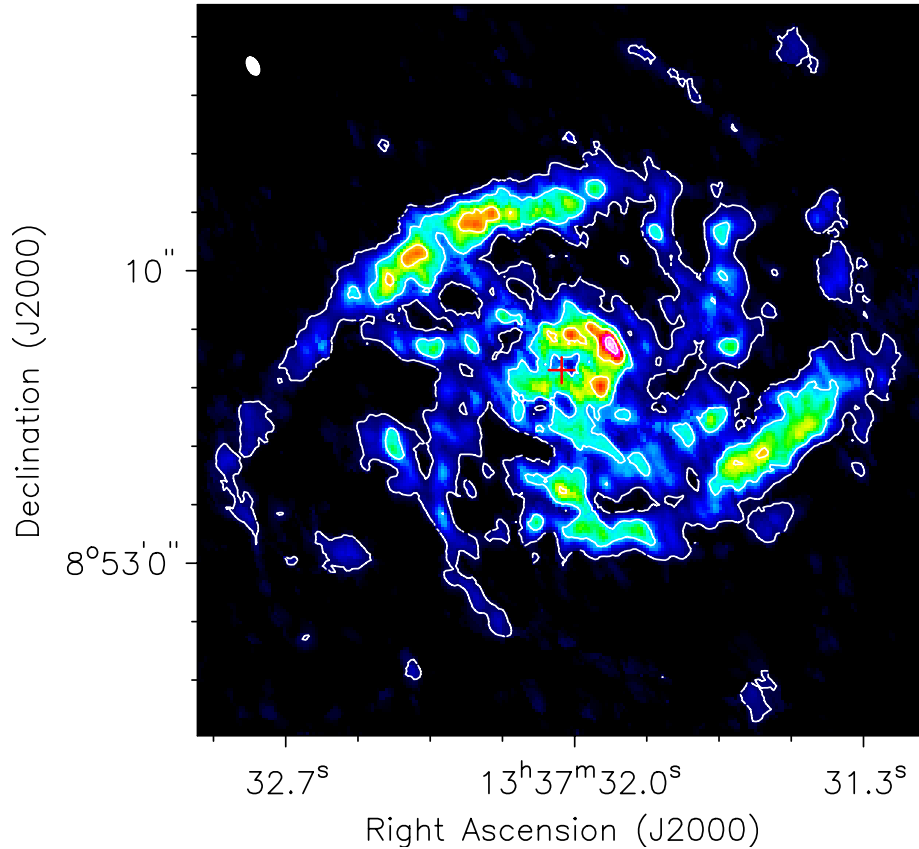
Figure 4.4: Integrated $^{12}$CO(2-1) emission in uniform weighting for the inner 1.5 kpc radius of NGC5248. The $^{12}$CO(2-1) emission has been integrated from -135 km s$^{-1}$ to 155 km s$^{-1}$ relative to the systemic velocity of 1153 km s$^{-1}$. Contours start at 5$\sigma$ in 10$\sigma$ steps (1$\sigma$ = 0.014 Jy beam$^{-1}$ km s$^{-1}$). The red cross indicates the position of the photometric center. The beam size is shown in the upper left corner and corresponds to the values listed in Table 4.2.
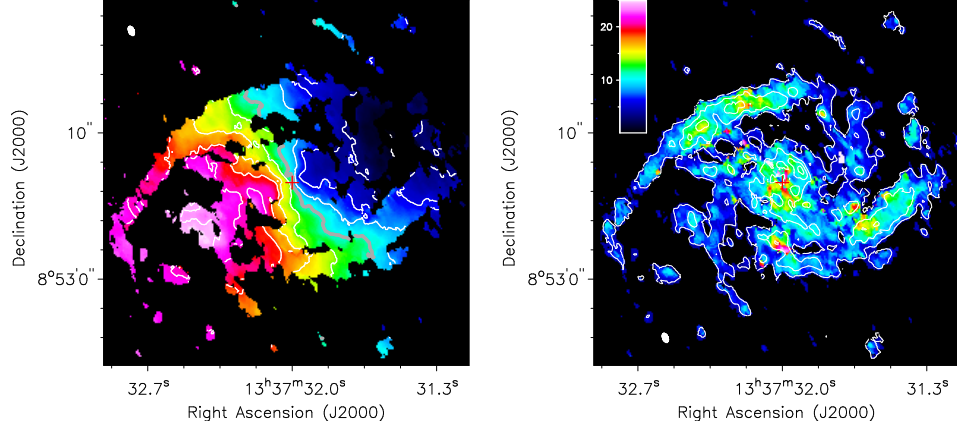
Figure 4.5: *Left:* First moment map of the $^{12}$CO(2-1) emission. Contours: -150 to 150 km s$^{-1}$ with 25 km s$^{-1}$ steps, 0 km s$^{-1}$ thick gray contour. *Right:* Second moment map of the $^{12}$CO(2-1) emission. Contours are the integrated $^{12}$CO(2-1) emission in 10$\sigma$ steps starting at 5$\sigma$. The kinematic center is given with a red cross. The color bar shows the dispersion in km/s.

radii is not smooth, which implies that there might be some non-circular motions present. More evidence for non-circular motions are found in the pv-diagram along the minor axis. If the gas was rotating with only circular velocities, then all velocities along the minor axis should be zero. This is not the case, in the r<2″ range there is some offset (up to -50 km s$^{-1}$). Also at larger radii deviations along this axis are present (at -5″ -7″ up to 30 km s$^{-1}$).

**Non-circular gas motions**

To investigate non-circular motions in the gas in more detail, the rotation curve of the gas is first needed. I have used the new CO(2-1) data in combination with the BIMA SONG CO(1-0) and VLA HI data to obtain a rotation curve spanning the entire galaxy out to 30 kpc, which at the same time has high enough resolution in the central kiloparsecs. The rotation curve was obtained by fitting tilted rings with a fixed PA of 115°, fixed inclination of 43.1° and fixed dynamic center, using the GIPSY routine ROTCUR. The result is shown in Fig. 4.7.

From the center to the edge of the FoV, the CO(2-1) velocity was sampled every 1″ out to 16″ in a 20° wedge around the fixed PA. Similarly, the BIMA SONG CO(1-0) velocity was sampled every 2″ out to 42″. Finally, the HI velocity field was sampled every 6″ out to 6.5′. The derived velocities match very well at the radii where the different datasets touch. Fig. 4.7 shows both a zoom of the inner 4 kpc (*left*) and the full rotation curve (*right*).

Any non-circular (radial) motion contaminates the circular velocity measurement in an inclined disk, as can be understood from simple geometry. Inside the CR of the
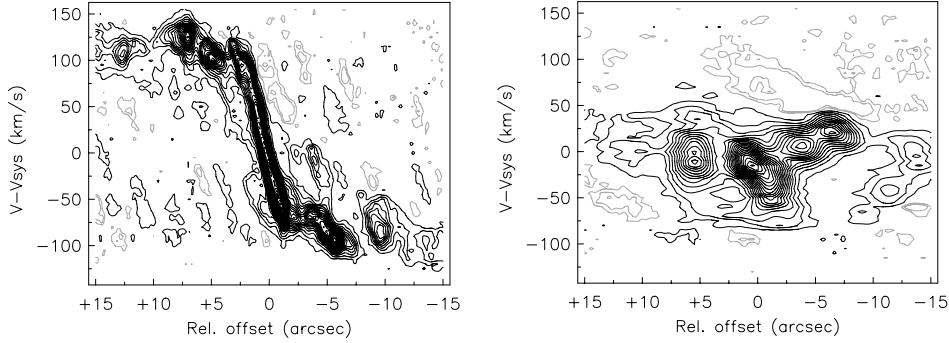
Figure 4.6: *left:* Position-velocity diagram along the major axis (PA of 113°) through the dynamical center. *right:* Position-velocity diagram along the minor axis (PA of 23°) through the dynamical center. In both panels, the contours are at $2\sigma$, in $2\sigma$ steps. The kinematic center is at (0,0).
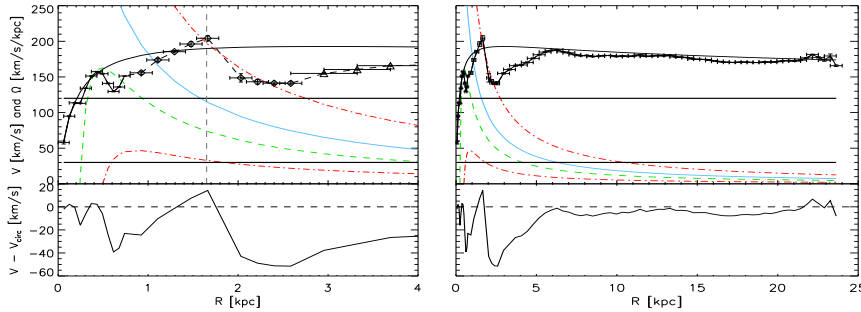


Figure 4.7: Gas rotation curve of NGC 5248, spanning the inner 4 kpc (*left*) and the entire disk out to 24 kpc (*right*). The rotation curve is based on our CO(2-1) (crosses), as well as BIMA SONG CO(1-0) (diamonds) and VLA HI (triangles) observations, giving both high spatial resolution and large radial coverage (fit using equation 4.1, solid line). Frequency curves of $\Omega$ (blue), $\Omega + \kappa/2$, $\Omega - \kappa/2$ (both red) and $\Omega - \kappa/4$ (green) are also presented. Two possible pattern speeds have been added in the *right* panel. The lower one at 30 km/s/kpc is a plausible pattern speed for the large scale stellar bar, and the higher one at 120 km/s/kpc would be a possible pattern speed for an additional inner pattern, such as a bar or disk. The approximate radius (1.65 kpc) where the CR of the inner bar and the oILR of the large scale stellar bar would overlap is given by the grey dashed vertical line in the left panel. The bottom panels show the difference between model and observed velocities. (See text for further details)

large scale stellar bar the radial motion will be a *net* inflow as gas is losing angular momentum, as discussed in Chapter 1.1. An inflow would subtract from the measured circular velocity. Therefore, a circular velocity curve of the following form is fitted as an upper envelope to the peaks in the rotation curve (solid line in Fig. 4.7).

$$V_{rot}(R) = \frac{V_{max} \times (R/R_{max})}{[1/3 + 2/3 \times (R/R_{max})^n]^{3n/2}} \qquad \boxed{4.1}$$

with $V_{max}$=156 km s$^{-1}$, $R_{max}$=440 pc and n=0.855. This smooth profile is indicative of the real galactic rotation profile, if all material was only rotating on circular orbits. The difference between the measured velocity and the circular velocity is shown in the bottom panel of Fig. 4.7. At radii larger than 6 kpc there is very little deviation from the circular velocity profile. Inside 6 kpc the offset reaches - 50 km s$^{-1}$. This radius of 6 kpc (~95″) is equal to the length of the semi-major axis of the large scale bar (Jogee et al., 2002a). The range of influence of the large stellar bar on the gas is thus very clearly observed.

The offset between the circular velocity curve and the observed rotation curve in the inner 4 kpc shows three dips, or vice-versa, three points where both are equal. This is somewhat misleading, as I did fit to these peaks. But, following the earlier statement that non-circular velocity lowers the circular velocity measurement, this result is not biased. The peaks are located at 1.3-1.7 kpc, 400 pc and 100 pc. The latter two can be immediately linked to the radii of the outer and inner circumnuclear rings. At ~1.5 kpc there is no ring structure, but in the dust spiral shown in Fig. 4a of Jogee et al. (2002b) it does seem that the spiral's pitch angle changes significantly at this radius, indicating a change in orbit orientations.

The $\Omega$, $\Omega + \kappa/2$, $\Omega - \kappa/2$ and $\Omega - \kappa/4$ frequency curves, based on the fitted circular velocity, are also included in Fig. 4.7. No definite measurements of the pattern speed of the large scale stellar bar exist. Jogee et al. (2002b) estimate that it must be close to 30 km/s/kpc given the semi-major axis of the bar; the co-rotation radius is typically at 1.2±0.2 times the semi-major axis of the bar (Athanassoula, 1992a). If the pattern speed is 30 km/s/kpc, then the CR would be at 7 kpc, the two ILRs at 1.6 kpc and 600 pc. These two values for the radii of the ILRs are very close to the radii where the change in pitch angle in the dust spiral and the outer circumnuclear star forming ring are located, which makes the proposed pattern speed likely.

It is difficult to match a resonance radius of the large scale stellar bar to the inner ring with 100 pc radius. Only a high order resonance would intersect with the pattern speed at such a small radius, which makes it highly unlikely that a gas ring would form near it. An option is that a nested bar (or any other non-axisymmetric pattern) has a resonance consistent with the location of the inner ring. A stable configuration for a non-axisymmetric pattern would have the CR of the inner pattern at the ILR of the large scale bar (Maciejewski et al., 2002). In Fig. 4.7 a second pattern speed has been drawn at 120 km/s/kpc. At this pattern speed the CR of the inner pattern corresponds to the outer ILR of the large scale bar. In Sect. 4.6 I will provide further arguments for this choice. Maciejewski et al. (2002) also note that an inner pattern ends well within its CR, so the inner pattern would not be very spatially extended.

Using the smooth circular velocity curve, I also look at the 2D distribution of non-circular motions in the CO(2-1) velocity field. The residual velocity field, obtained
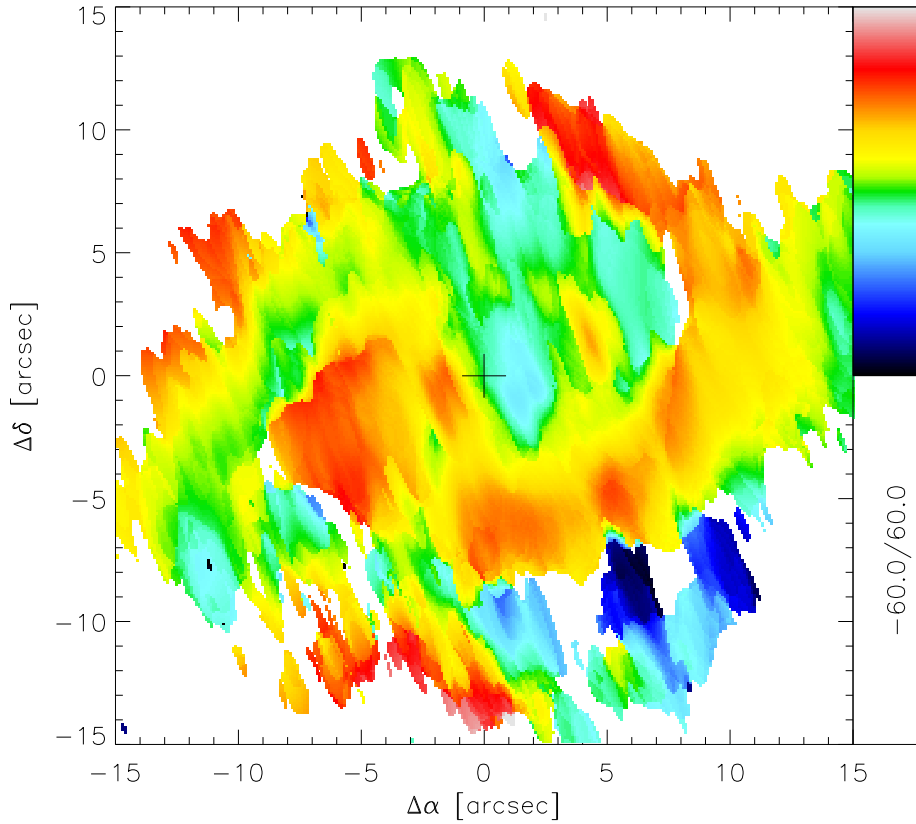
Figure 4.8: CO(2-1) residual velocity field, obtained by subtracting the modeled circular velocity from the observed CO(2-1) velocity field. The velocity range of non-circular velocity spans [-60,60] km s$^{-1}$. The kinematic center is at (0,0).

by subtracting a circular velocity from the observed velocity distribution is shown in Fig. 4.8. The residual field is dominated by a spiral arm structure spiraling out from the east to the south. This southern spiral arm shows residual velocities of up to 40 km s$^{-1}$/sin($i$)=60 km s$^{-1}$. It extends from the inner circumnuclear ring to the edge of our field. Comparison with the velocity dispersion field (Fig. 4.5) shows no corresponding pattern. Given the orientation of the galaxy, the south-west is the near side, which means that the positive non-circular velocity would constitute an inflow. No corresponding spiral arm is seen in the north, implying that the inflow is not symmetric along the large scale bar major axis. Similar asymmetries are present along the one-sided non-zero velocities in the minor axis pv-diagram (Fig. 4.6).

## 4.5   Stars and star formation in the center of NGC 5248

I have provided evidence for gas inflow from the outer to the inner circumnuclear ring, which can very well be due to a nested pattern of non-axisymmetric structure. Inflow and the build up of gas mass at the inner circumnuclear ring should lead to star formation. In this section I investigate the ages of the stellar populations in and around both rings, and constraint the relative star formation histories in both circumnuclear rings, as the final piece to understand the formation of both rings.

### 4.5.1   Ages of the stellar clusters in the rings

The first part of this work is based on the extracted aperture photometry of Maoz et al. (2001) of 507 star cluster candidates. The data set consists of the following broadband filters: F220W, F336W, F547M, F814W and F160W. I used the $\chi^2$ fitting routine and Starburst99 models also used in Chapter 3 to re-determine the ages, masses and color excess for each star cluster. The Starburst99 version (v6.0.2) (Leitherer et al., 1999; Vázquez & Leitherer, 2005; Leitherer et al., 2010) was run, in burst mode, with a Kroupa IMF, solar metallicity and Padova AGB solar metallicity tracks. Output was generated every 2 Myr years. The new results mainly reflect the improvements in stellar models over the past 10 years since the results of Maoz et al. (2001) were published. I also included nebular emission in the model fluxes, which adds significant emission for young ages at, predominantly, the shorter wavelengths. My photometric library also contains a larger age range than the original Maoz et al. (2001) work. Table 4.3 gives the ages, masses and color excesses for the first 20 stellar clusters (the full table is available in the appendix).

I find that in comparison with previous results the star clusters

- have slightly lower $\chi^2$ values,

- are on average 30% times heavier,

- are older (>50Myr), and

- have a similar color excess

There are several factors that can explain why I obtain heavier and older star clusters. I use a Kroupa IMF, while Maoz et al. (2001) used a Salpeter IMF. A Kroupa IMF includes *more* stars with less than 1 solar mass. Most of the luminosity is contained in the high mass stars, so the low mass stars can increase the total mass of a cluster without (significantly) increasing the luminosity. This result holds even when I take the difference in high mass cut-offs into account. A second factor that changes the star cluster mass is that my fitting routine finds on average slightly older star cluster ages. The inclusion of nebular emission boosts the short wavelength side of the younger model SEDs and fewer star clusters fit that description. A direct result is that the fitted mass of the star cluster must then again increase, since the mass-to-light ratio increases with age. These two factors in mass 'gain' are offset by a difference in the adopted distance to the galaxy. I have adopted a newer distance measurement of 12.7 Mpc for NGC 5248 (Tully et al., 2009), while Maoz et al. (2001) adopted a distance of

22.7 Mpc. This should make our results about 3 times lighter. Together these factors culminate in the 30% more massive star clusters in our fitting.

Table 4.3: Star cluster ages, extinctions and masses

| ID | Age [Myr] | E(B-V) | log(Mass/$M_\odot$) | $\chi^2$/d.f. |
|---|---|---|---|---|
| 001 | 6 | 0.00 | 4.8 | 18.29 |
| 002 | 90 | 0.05 | 5.4 | 12.98 |
| 003 | 16 | 0.00 | 4.8 | 10.23 |
| 004 | 38 | 0.06 | 5.0 | 4.19 |
| 005 | 22 | 0.38 | 5.0 | 10.87 |
| 006 | 46 | 0.12 | 5.0 | 3.13 |
| 007 | 6 | 0.00 | 4.0 | 6.31 |
| 008 | 6 | 0.15 | 4.0 | 5.60 |
| 009 | 6 | 0.20 | 4.0 | 6.93 |
| 010 | 52 | 0.00 | 4.8 | 10.87 |
| 011 | 28 | 0.00 | 4.6 | 7.61 |
| 012 | 50 | 0.04 | 4.8 | 9.20 |
| 013 | 6 | 0.05 | 3.8 | 6.54 |
| 014 | 6 | 0.25 | 4.0 | 3.87 |
| 015 | 42 | 0.00 | 4.6 | 4.16 |
| 016 | 34 | 0.07 | 4.6 | 0.34 |
| 017 | 44 | 0.00 | 4.6 | 5.41 |
| 018 | 22 | 0.37 | 4.6 | 12.36 |
| 019 | 26 | 0.00 | 4.4 | 3.31 |
| 020 | 122 | 0.18 | 5.0 | 4.50 |

**Notes:** Results of the $\chi^2$ fitting of age (column 2), color excess (column 3) and mass (column 4) of the observed star clusters (first 20 shown). The star cluster ID in column 1 is equal to that in the Maoz et al. (2001) electronic table. The full table is available in the appendix (Table A.1).

The star cluster fitting output is visualized for each ring separately in Fig. 4.9. I have averaged the results per 45° angle interval for each ring. Any gradient that is visible as a function of azimuthal angle gives information on preferred star formation locations in the ring. For clarity the four quadrants in each ring have been designated by the corresponding point on a compass. The angle is thus measured from the south, in a counter-clockwise manner on the sky.

The star clusters in the outer ring have an average age of 100 Myr, an average stellar mass of $10^{4.5} M_\odot$ and a color excess of 0.4-0.6 magnitude. No variation in any three of these parameters as function of azimuthal angle is seen. This implies that either the star formation was/is occurring in a fairly uniform action in the outer circumnuclear ring or
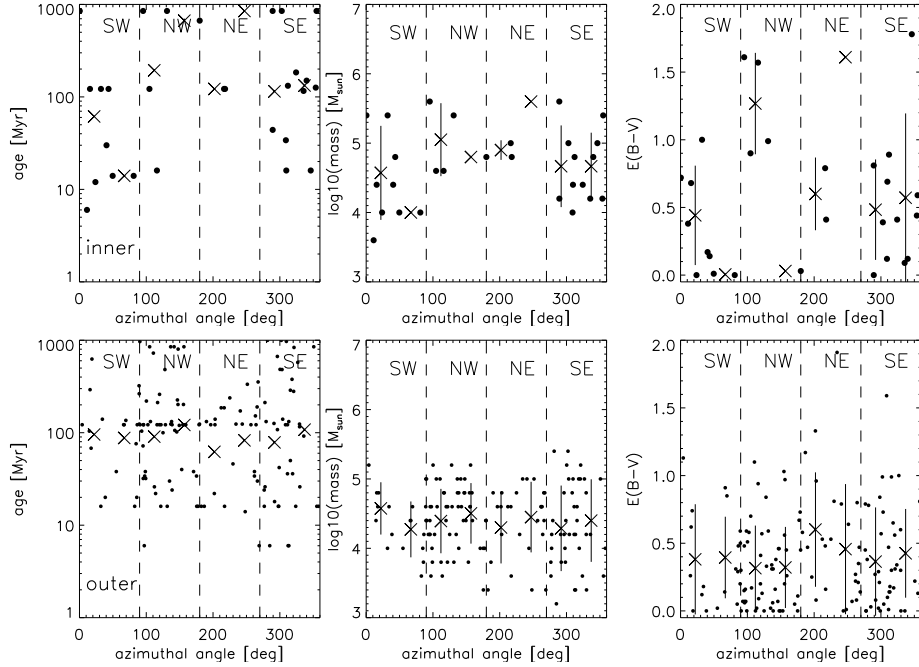
Figure 4.9: Results of the $\chi^2$ fitting. The inner ring is given on the top row, the outer ring is on the lower row. From left-to-ring: age, mass and color excess. The four quadrants of the ring are indicated in the plots.

that any preferential formation location has been washed out by dynamical processes (see also NGC 6951 in the previous chapter).

The inner ring shows bimodal age behavior. The inner ring has on average somewhat older star clusters, but also a large fraction of young (10-30 Myr) star clusters in the SW/SE quadrants. Based on absence of [FeII] Böker et al. (2008) concluded that the inner ring hosts star formation younger than observed in the outer ring. My finding of an additional older population suggests that this is not the first time star formation occurs in this ring. [FeII] emission is believed to trace supernova activity (which starts $\geq 10$ Myr after star formation) and the lack therefore in this ring, combined with the older star clusters I find, suggests that star formation is intermittent, possibly periodic, in the inner ring. The cluster mass range is somewhat higher than in the outer ring, with cluster masses between $10^{4.5}$ and $10^{5.5}$ $M_\odot$. The color excess distribution also shows no azimuthal dependence. The measured E(B-V) is mostly constant, except for the NW quadrant, were it is 1.3 mag. The NW is also were the highest concentration of CO(2-1) emission was detected (Fig. 4.4). Compared with the position of the young star clusters, it appear that in the clockwise rotation of the galaxy, the highest extinction is partly co-spatial with the CO(2-1) emitting gas, followed by the location of the youngest star clusters in this inner circumnuclear ring. I speculate in the discussion on the role that an inner pattern would play in the bimodality of the age distribution and

94

in generating this gradient of extinction, gas and young stars.

We can further infer that the star clusters must form in situ, since the spatial distribution of the observed star clusters shows a clear spatial dichotomy between the two rings. This precludes migration of clusters from the outer onto the inner ring.

### 4.5.2 Stellar populations from SAURON observations

I supplement the star cluster analysis above, with an analysis of the underlying stellar population as traced by SAURON IFU observations. Results from the fit with a full range of age and metallicity SSP models to the SAURON data cube are shown in Fig. 4.3. This more extensive fit showed that solar metallicity is the predominant metallicity in this galaxy. A fitting residual of ~1.5% of the flux remains in each spaxel.

Following the method in the previous chapter (Section 3.6.2.), I used a combination of 4 SSP model spectra to fit again the stellar light in each spaxel. The SSPs selected have solar metallicity and model ages of 70.8 Myr, 158.5 Myr, 398.1 Myr and 3.2 Gyr. The emission lines, H$\beta$, [OIII], and [NI], are also fitted in this analysis, to avoid contamination of the SSP results by gaseous line emission. I iterated the fitting 30 times, and each time introduced some random noise on the level of the initial fitting residual. A fitting uncertainty of less than 5% is reached in this manner.

The output from pPXF and GANDALF contains the number weighted fractions of each SSP spectrum at each spaxel. From these number weighted fractions the mass weighted fractions at each position are determined. This mass fraction is multiplied with the stellar intensity at each position to give an absolute mass distribution in each SSP age bin. The result is shown in Fig. 4.10.

In the youngest age bin, high stellar masses are predominantly seen at two locations opposite each other at the radius of the outer ring. Relative to the position angle of the large scale stellar bar, these locations are parallel to the bar. No significant stellar mass at the position of the inner ring is seen. This could indicate that, even though we detected young stellar clusters in the inner ring, they have not build up enough stellar mass to be visible in this analysis. The north-south devision seen in the 'original' SAURON stellar light distribution (Fig. 4.3) is also present here, which means that the overall stellar light is dominated by young stars.

The intermediate age bins of 158.5 Myr and 398.1 Myr show the least stellar mass of all panels. In Section 3.6.2. I also remarked on this. The fitting routine minimizes the number of SSP spectra needed to achieve an acceptable fit. The high(est) contrast between 'young' and 'old' is used when possible. Nevertheless, some intermediate age stellar populations are found in both the outer and inner circumnuclear ring. The 'old' stellar mass map clearly traces the stellar bulge population, peaking in the center.

## 4.6 Discussion

### 4.6.1 Clues to the nested bar scenario

The large scale stellar bar has a dominant influence on the gas distribution in the circumnuclear region. The pattern speed proposed by Jogee et al. (2002b) of approxi-
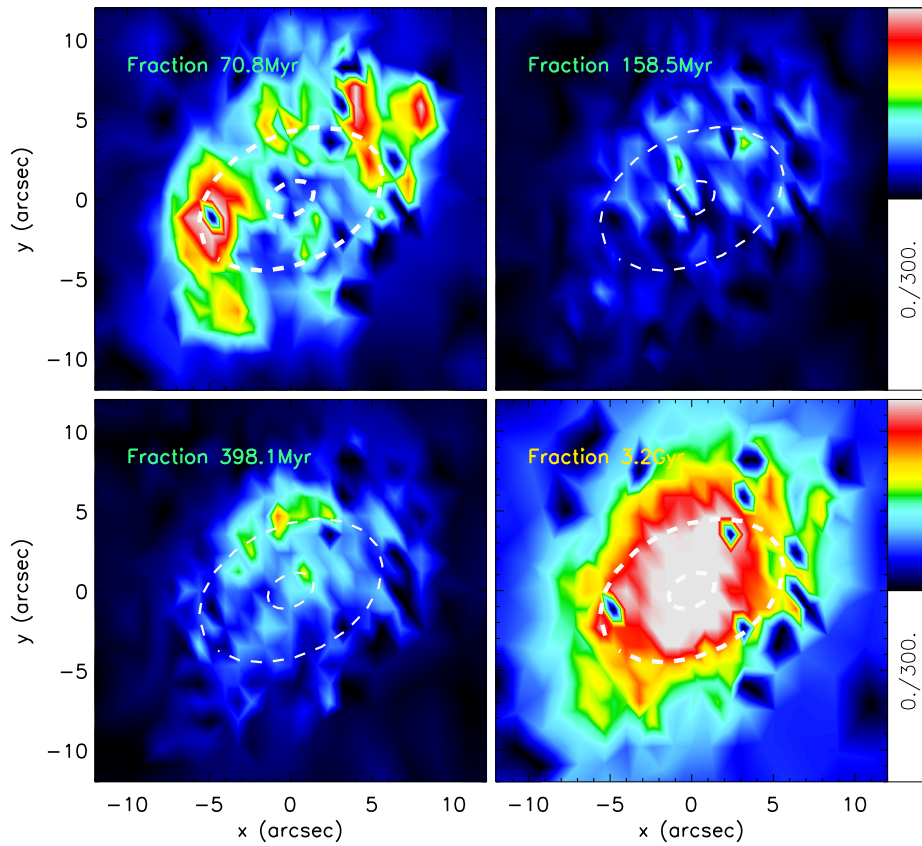
Figure 4.10: Stellar 'mass' maps for the 4 age bins fitted to the SAURON IFU data set. The ages of each SSP is given above. The maps have been corrected for inclination and the positions of the two circumnuclear rings (1.5″ and 6″) have been indicated.

mately 30 km/s/kpc for this bar is reasonable, given the size of the bar and the location of the outer circumnuclear ring (just inside the ILR).

This outer circumnuclear ring is most likely indeed a ring and not a spiral structure in the gas, even though the molecular gas does not form a full ring. Firstly, the outer circumnuclear star forming ring is clearly a ring in H$\alpha$ images. The distribution of star clusters in the circumnuclear region also shows a gap in star cluster positions between the inner and outer circumnuclear ring radii. It is true, that the distribution of CO molecular gas does not show a ring structure at the outer ring radius, but two spiral arms in the north and south. If these CO spiral arms would form a ring at this radius, then the molecular gas inflow is sporadic and gas has been depleted. Consequently the inner CO spiral structure must be independent of the large scale bar. If the CO spiral arms continue to spiral inwards and the outer ring is only a stellar ring, then it presents no effective barrier to continued gas inflow. The first scenario is more likely, given the low CO(2-1) velocity dispersion; the molecular gas is probably too cold (Maciejewski, 2004b) to continue to spiral inwards as in the spiral density scenario that has been proposed by Englmaier & Shlosman (2000). I thus believe that the outer ring is a proper circumnuclear star forming ring that acts as a gas barrier to inflowing gas. The inner CO structure could be shaped by gravitational torques from a nested pattern acting on the gas. The oval of 3″ size would fit this role perfectly.

There are more arguments to support the claim of nested patterns in NGC 5248. In the region of influence of the large scale stellar bar there are 3 radii where the observed rotation curve and the fit circular velocity curve are equal. At these radii (100 pc, 400 pc and 1.3 - 1.7 kpc) the gas must be undergoing only minimal radial velocities and thus be on either $x_1$ or $x_2$ orbits. The inner and outer circumnuclear rings cannot be both on $x_2$ orbits, otherwise there should be no clear gap. If the gas on the inner ring is then on a new set of relaxed orbits, this flip in orbit families can only be caused by an inner pattern. This is a somewhat simplified version of orbits in a double (bar) pattern potential, a more detailed model of orbits in double bar potentials is given by Maciejewski & Athanassoula (2007).

The gravitational torque distribution for NGC 5248, derived by Haan et al. (2009) does not show the characteristic 'butterfly' pattern of a bar at these radii. Instead it is more characteristic of a m=1 perturbation. Therefore, the gravitational torque distribution at these radii is clearly not a continuation of the large scale stellar bar torque distribution which is seen at larger radii (Figure 11 from Haan et al., 2009). This leads me to hypothesize that the 3″ oval is a lop-sided disk. There is some corroborating evidence for the possible lopsidedness of the inner pattern. A single arm with inflow velocities was found, which also indicates some type of uneven distribution, and in the pv-diagram along the minor axis, non-zero motions were only found on the same, one side of the velocity field. Lop-sidedness of an inner pattern also has consequences for the inflow frequency onto the inner ring, which allows me to explain the bimodal age distribution of the star clusters in the inner ring very well, as which I will discuss in the next section. This good correspondence provides another argument for the presence of a lop-sided nested pattern in NGC 5248.

### 4.6.2 Star formation scenarios in the circumnuclear rings

The star clusters in the outer circumnuclear ring show no correlation between their age and their location in the outer circumnuclear ring. However, in the IFU results, there is a relation between stellar 'mass' in the young SSP bin and location in the outer circumnuclear ring. In the young age bin, the highest stellar masses are found at two positions in the ring. These positions are north-west and south-east, and are anti-correlated with the CO spiral arms at this radius. This result would corroborate my hypothesis that gas has been depleted in these parts of the ring, but that a gas ring would be observed if the gas inflow was higher or if the gas was not depleted at these positions. This offset is, furthermore, an indication for the 'pearls-on-a-string' scenario, proposed to characterize how star formation occurs in circumnuclear rings by Böker et al. (2008). In this scenario, star clusters form at preferred locations in the ring. These locations are where the dust/gas lanes of the large scale bar connect to the ring, and are named 'overdensity regions'.

Evidence for these overdensity regions may further be found in the 1 mm continuum map (Fig. 4.2). Two high emission regions are present in the 1 mm continuum distribution at the radius of the outer circumnuclear stellar ring. 1 mm emission arises most likely from cold dust and traces the bulk of the gas mass in the circumnuclear region. The position of these 1 mm emission peaks is consistent with the reasonable assumption on the locations of overdensity regions, given the PA of the large scale stellar bar. The combination of the high emission regions in the 1 mm continuum map and the young stellar mass concentration would form two 'pearls' of the 'pearls-on-a-string' scenario; current star formation and recent star formation.

As for the lack of correlation between the star cluster ages and their location in the outer circumnuclear ring, this is puzzling and deserves further study.

The star formation in the inner ring showed also some indication for sites of preferred star formation. The young star clusters (ages <40 Myr) are found exclusively in the southern half of the ring. A sequence is found, going from position with the highest extinction (interpreted as location of current/future star formation), followed by/partly co-spatial with the CO(2-1) emitting gas, followed by the location of the youngest star clusters in this inner circumnuclear ring. In analogy with the outer circumnuclear ring, we could have 3 'pearls' here, but starting only at one contact point.

Given the two proposed pattern speeds, based on the CR/ILR overlap (Fig. 4.7) and hypothesized lop-sidedness of the inner pattern, I can also make estimates for the frequency of inflow onto the inner ring. The two bars should align every 80 Myr ($\frac{2\pi}{\Omega_{p,inner}-\Omega_{p,large}}$). Half of that time (40 Myr) some part of the gravitational torque distributions will be aligned to allow inflow. The dichotomy between the young <40 Myr and the old >100 Myr star clusters would be well explained in this context.

The 26% of total observed molecular gas mass we find in the inner circumnuclear ring region, can quickly be build up. In this 40 Myr timescale the gas on the inner ring will have completed several orbits ($\frac{\pi}{50\,[\mathrm{km/s}]/0.1\,[\mathrm{kpc}]}$) in its inertial frame. This makes detecting any stellar age gradient beyond the very crude and broad one I do find, impossible.

## 4.7 Summary

The double circumnuclear star forming ring system in NGC 5248 cannot be explained in the context of a single large scale stellar bar influencing the gas distribution in the central region of this galaxy. The outer circumnuclear ring at 370 pc is close to the iILR of the large scale stellar bar and can be explained by gas settling on $x_2$ orbits just inside the resonance, but the same cannot be true for the inner circumnuclear ring at 100 pc.

An inner oval of 3″ size is very likely responsible for the inner circumnuclear ring. In the context of nested patterns, the inner circumnuclear ring would be a result of this inner oval, and not the large scale bar. I find evidence of non-circular inflow motion between the two star forming rings. This inflow motion is contained in a single spiral arm. This result, the m=1 gravitational torque distribution found by Haan et al. (2009) and the relation between the 1 mm continuum, CO and young star cluster locations in the inner ring, all imply that the inner oval is a lop-sided disk.

A stable system of nested patterns can be sustained when the inner pattern's CR is at the same radius as the large scale bar's ILR. The large scale bar has a likely pattern speed of 30 km/s/kpc. Therefore, the pattern speed of the inner pattern is likely 120 km/s/kpc.

In both circumnuclear star forming rings I find evidence for preferred sites of star formation that can be linked to the inflow locations of gas onto the rings. This is in accordance with the 'pearls-on-a-string' scenario by Böker et al. (2008), where star formation occurs quickly after gas has reached the resonance ring location.

# 5

# Summary and outlook

The aim of this thesis is to understand the role that circumnuclear star forming rings play in the secular evolution of galaxies. Circumnuclear rings have radii of 50 pc to 1 kpc and are present in the central regions of ~20% of all nearby disk galaxies (Knapen, 2005; Comerón et al., 2010). They act as gas reservoirs, halting gas inflow, and are strongly star forming, with star formation rates of up to 50 times that of quiescent star forming galaxy disks (Kennicutt, 1998a). Depending on their life times they may build up large stellar masses in the central region.

I study the following aspects of circumnuclear star forming rings in the two nearby galaxies, NGC 5248 and NGC 6951, using multi-wavelength data. I investigate the gas dynamics in and around the circumnuclear rings to determine how circumnuclear star forming rings influence gas dynamics and quench nuclear feeding, and I study the stellar content in these rings to determine the life times of the rings and the duration and intensity of star formation episodes in the ring.

## 5.1   Questions raised in this thesis

### 5.1.1   How does a circumnuclear star formation ring influence gas (in)flow in the central region of their host galaxy?

Theory and modeling has shown already that circumnuclear rings form where gas does not receive a further *net* gravitational torque and when there is a sufficient number of $x_2$ orbits present (Athanassoula, 1992b; Regan & Teuben, 2003; Maciejewski, 2004a,b). Gas will stop flowing inward and the circumnuclear ring forms at the gas barrier. However, there is little observational evidence of the true effectiveness of a circumnuclear ring as a gas barrier.

In NGC 6951 we see that almost no molecular gas is found inside the ring radius. The observed amount of CO emitting gas inside the ring, compared to the total amount I found, is only 3% ($M_{H_2}$ ~0.7/22.0 $\times 10^8$ $M_\odot$).

The gravitational torque distribution as a function of radius (Fig. 2.12) showed *net* positive gravitational torques inside the circumnuclear ring radius in NGC 6951. However, the inclusion of the 30m data did show that this barrier is much lower than was previously calculated using interferometric data alone (García-Burillo et al., 2005; Haan et al., 2009). I also found some CO emission inside the ring radius that showed

peculiar motion offset with respect to the overall velocity field by up to 70-90 km/s (Fig. 2.7). I hypothesized that this small package of molecular gas (only $2.4 \times 10^6 \, M_\odot$) is inflowing under the influence of a nuclear oval (García-Burillo et al., 2005). Although I did not remark upon this in chapter 2, NGC 6951 seems to be hosting a nested bar system.

A nested system of patterns is also what I find in NGC 5248. I believe the molecular gas distribution cannot be explained, unless the gas distribution is driven by two nested patterns. Since the velocity dispersion of the gas is low, an Englmaier & Shlosman (2000) like nuclear spiral, which was proposed by Jogee et al. (2005) seems unlikely. This implies that a second perturbation is necessary to move gas inward to the inner ring.

Other processes that may play a role in gas motion (dynamical friction and viscosity torques) were discussed in detail by, e.g., García-Burillo et al. (2005). They show that dynamical friction, or gravitational drag, influences gas motion on much longer time scales than gravitational torques and is thus of very low importance in the overall gas motion. The authors do mention that dynamical friction could have a significant influence on the gas already at the nucleus in NGC 6951. NGC 6951 has an AGN at the center. Within the inner 50 pc, the time-scale of dynamical friction would be ~1 Myr. And the current molecular concentration at the nucleus ($M_{H_2} \sim 7 \times 10^7 \, M_\odot$) is sufficient to maintain the nuclear feeding at this level for the next $10^4$ Gyr, if we use the mass accretion rate ($\dot{M} = 6 \times 10^{-6} \, M_\odot$) derived by Dumas et al. (2007). But at larger radii, the influence of dynamical friction would quickly diminish, as time for dynamical friction scales with $r^2$ (Chandrasekhar, 1943). At the radii of the circumnuclear rings in NGC 6951 and NGC 5248 it should therefore play no role.

Viscosity torques are also predominantly becoming important at small radii, but can be enhanced by strong density gradients in the gas. In this context, viscosity may play a role in transporting gas from the inner circumnuclear ring inward towards the nucleus in NGC 5248. This is nicely shown in the figure by García-Burillo et al. (2005), reproduced here (Fig. 5.1). A gas ring at 100 pc from the nucleus (exactly like the inner circumnuclear ring in NGC 5248) would broaden due to viscous torques and reach the nucleus within 60 Myr.

Taken together, I observe that circumnuclear star forming rings halt gas flow towards the galactic nuclei, but in both galaxies I find indications for secondary gravitational components that could enable further inflow. This is most clearly seen in NGC 5248, where there are actually two circumnuclear star forming rings.

### 5.1.2 In which manner does star formation proceed in circumnuclear star formation rings?

There are two competing scenarios for the manner in which star formation in circumnuclear star forming ring proceeds, the 'popcorn' scenario proposed by Elmegreen (1994) and the 'pearls-on-a-string' scenario proposed by Böker et al. (2008). I show a cartoon in Fig. 5.2 (adapted from Böker et al., 2008) that clearly shows the observable differences between the two scenarios. In the 'popcorn' scenario there should be no azimuthal dependence on age, in the 'pearls-on-a-string' scenario that is the main characteristic.
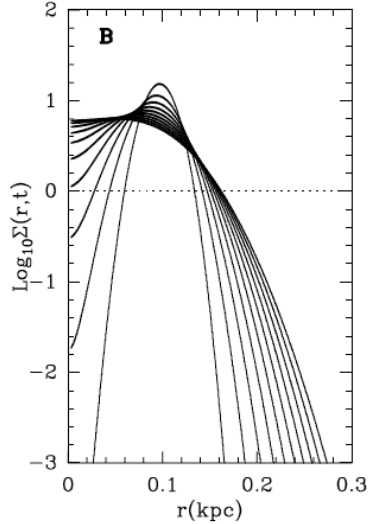
Figure 5.1: Time evolution of viscosity torques in a 100 pc radius gas ring. The initial ring has a radius of 100 pc, and a width of 20 pc. As time progresses in $2 \times 10^7$ yr steps, the surface density distribution broadens. The dashed horizontal line is an arbitrary detection limit. In this plot, we would detect gas at the nucleus $6 \times 10^7$ yrs after the ring is formed. Adapted from García-Burillo et al. (2005)

In both NGC 5248 and NGC 6951 I have found evidence for the 'pearls-on-a-string' scenario.

For all three rings I performed a star cluster age analysis. The inner ring of NGC 5248 and the ring of NGC 6951 show preferential locations for young star clusters in their rings. These positions are consistent with locations where gas enters the ring. The star clusters in the outer circumnuclear ring of NGC 5248 do not show a differential age distribution.

In the stellar population analysis with the SAURON IFU data, preferred locations for young stars were also found. The locations with young stars in NGC 6951 derived with this second method is consistent with the location inferred from the star cluster age analysis. In NGC 5248, the outer ring does show preferred locations for young stellar populations unlike in the star cluster analysis. Also in this ring the locations are consistent with the locations where gas enters the ring. The inner ring of NGC 5248 was not detected, most likely since the observed spectra from this region are dominated by the stellar light from the old population.

Obtaining a true age gradient is observationally near-impossible. The short dynamical timescales in these central regions quickly mask any azimuthal age signature within 10-20 Myr, as I have discussed in Section 3.7.1 and 4.6. The best signposts are hot spots of young stars at the correct locations, as I have found. My results thus do imply that the 'pearls-on-a-string' scenario is correct.

Several other studies have also run into the same age detection limit and recov-
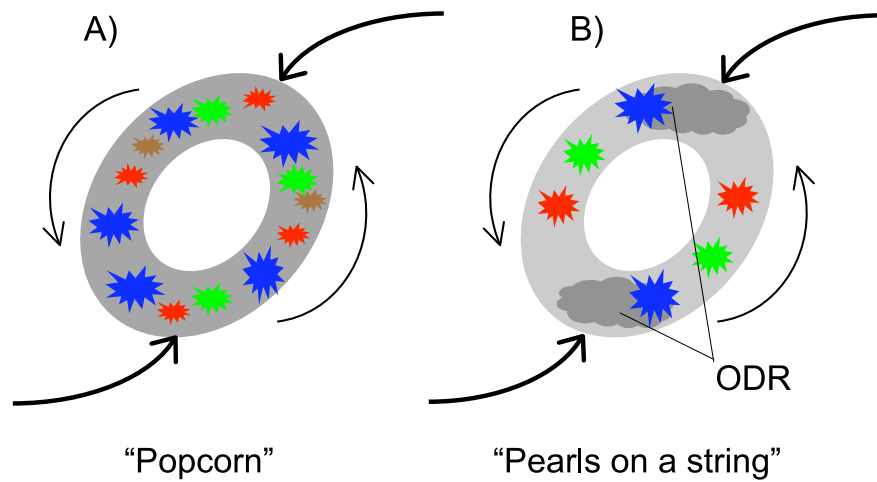
Figure 5.2: Cartoon of the two star formation scenarios proposed for star formation in circumnuclear star forming rings. On the left, the 'popcorn' scenario where gas mass builds up uniformly in the ring. Star formation events are distributed randomly throughout the ring. On the right, the 'pearls-on-a-string' scenario where gas density is higher near the gas inflow points and star formation occurs at preferred locations. As the system rotates, and star formation continues, an age gradient in the stellar ring population is introduced. Star formation events are depicted with blue (youngest SF), green (younger SF) and red (young SF) symbols. The gas inflow onto the ring is indicated by the thick arrows and the rotation sense of the system with the thin arrows. Figure adapted from Böker et al. (2008)

ered some evidence for the 'pearl-on-a-string' scenario. Two studies of NGC 4321 have found the clearest signature. Both studies measured stellar absorption indices and measured emission lines, which trace stellar ages up to ~10 Myr (Ryder et al., 2001; Allard et al., 2005). Similar signatures are present in the circumnuclear rings studied in Böker et al. (2008), the near-infrared emission lines [FeII], HeI and Br$\gamma$ trace stellar populations younger than ~35 Myr.

### 5.1.3  What is the age and lifespan of circumnuclear rings?

In Section 3.7.2 I have already discussed the probable high age of 1-1.5 Gyr for the circumnuclear ring in NGC 6951. A similar calculation using the star cluster results of NGC 5248 implies an age for the outer circumnuclear ring of 1-2 Gyr.

How long the ring can further survive, depends critically on the life time of the large scale stellar bar which drives the gas inflow. Jogee et al. (2004) and Sheth et al. (2008) have shown that the fraction of strongly barred, massive galaxies does not change out to z ~ 1. Therefore, the authors conclude that large scale stellar bars must be long lived structures. Modeling of circumnuclear rings has shown that the build up of stellar mass at the center (i.e. the formation of a (pseudo-)bulge) can destroy a bar Athanassoula et al., 2005). However, the central mass concentration has to reach several percent of the total disk mass in this model. On the other hand, Bournaud et al. (2005) suggest that large scale bars are transient features, and that it is not the central mass concentration, but the increase in angular momentum in the bar, obtained from the gas that is flowing inward, that completely destroys a bar. In this scenario large scale stellar bars would have a life time of only 1-2 Gyr.

In the first scenario circumnuclear star forming rings would be long lived; in the last 1 Gyr only of order $10^7 M_\odot$ in stellar mass has been formed in the circumnuclear rings in both galaxies, while the stellar mass of each galaxy is ~$10^{10} M_\odot$. Star formation would have to continue for another 10 Gyr before sufficient mass would be build up to destroy the bar which provides the inflowing gas for continued star formation in the ring.

In the second scenario, both circumnuclear rings would already be at the end of their star forming lives. In this scenario, the large scale stellar bar would dissolve now or soon, gas inflow onto the ring would stop and the stellar populations in circumnuclear ring would passively age.

To my knowledge, no such rings (with only red, old stellar populations) have been found. Thus large scale stellar bars and circumnuclear star forming rings must continue to live for a long time.

## 5.2  Outlook

Science is never done and each answer I have given here, leads to new questions in return. I discuss two avenues of inquiry that follow from the work I have done in this thesis.

### 5.2.1 Molecular gas physics in the ring

The distribution of young stars is not uniform in the circumnuclear rings I studied. This provides an ideal opportunity to study the relation between various molecular species and star formation, in a well constraint environment. The dynamics of the gas in the circumnuclear ring is known, i.e. gas is moving on well understood orbits, with minimal to no radial flows. Any relation found between gaseous and stellar tracers in circumnuclear rings, can be interpreted without the need to account for highly varying influences from the large scale environment, such as would be the case in spiral arms or in the star formation hot spots at the ends of large scale stellar bars.

Observing other molecular species and line transitions other than $^{12}CO(1-0)$ or $^{12}CO(2-1)$ is the next step in understanding the molecular gas physics in the extra-galactic context. Detailed studies of multiple molecules is something that is regularly done in Galactic studies, however higher sensitivities and good resolutions are required to conduct similar studies in extragalactic sources. Work by Usero et al. (2004); Meier et al. (2008); García-Burillo et al. (2010) and Meier et al. (2011) show that line diagnostics of multiple molecular species can now be resolved on scales relevant for detailed investigations into the circumnuclear regions of nearby galaxies.

The necessity of observing multiple molecular species is first of all the fact that $^{12}CO(1-0)$ is optically thick under many conditions. It is therefore not possible to learn any quantitative detail from the region under study just from $^{12}CO(1-0)$ alone. To obtain real measures of the density or temperature of the molecular gas an optically thin line transition needs to be observed, for instance from the isotope $^{13}CO$. Secondly, various molecules and ions trace different physics; density, heating, shocks, ionization. The chemistry of the ISM under the influence of stellar radiation from young stars is very complex (e.g. van Dishoeck & Black, 1988; Sternberg & Dalgarno, 1995), but can be understood by investigating a combination of molecular species that trace these various physics.

Most molecules have their rotational emission lines in the(sub-)mm wavelengths. Therefore, observations of these molecular species need mm-interferometers. The on-going extension of the PdBI to 12 dishes, i.e. the NOrthern Extended Millimeter Array (NOEMA[1]), providing, more sensitive receivers and longer baselines and, of course, the completion of ALMA (Atacama Large Millimeter Array) in Chile really open up this field of study to the extra-galactic regime and circumnuclear star forming rings would form an ideal laboratory.

### 5.2.2 Stellar radiation feedback on the gas

One process that I have not investigated in this thesis is the feedback of the star formation on the molecular gas present in the circumnuclear ring. We have seen that the locations of molecular gas inflow and star formation are linked, but the loop has not been fully closed.

The high FUV (6eV < h$\nu$ < 13.6eV) fluxes associated with young O and B stars have a strong influence on the state of the interstellar medium (ISM) that surrounds them. Depending on the strength of the FUV radiation field, FUV photons can deeply

---

[1]The NOEMA project: http://www.iram-institute.org/EN/content-page-235-3-235-0-0-0.html

penetrate molecular clouds up to $A_v$ <10 (Sternberg & Dalgarno, 1995).  The regions influenced by the FUV photons are called photo-dissociation or photo-dominated regions (PDRs).  The high depth that FUV photons can penetrate into molecular gas clouds implies that star formation can shut down or delay the next round of star formation by dissociating $H_2$.

The radiation density that is generated by the stars can be derived by observing the fine-structure lines of [CII] at $158\,\mu$m, [OI] at $63\,\mu$m and the FIR luminosity and comparing them against PDR models (e.g. Kaufman et al., 1999).  The outcome will give a measure for the (Hydrogen) number density, $n_H$, and the strength of the FUV radiation field, $G_0$.  From that it is possible to estimate the impact of the recent star formation on the (molecular) gas. By combining these results with observations of the current amount of HI in such a ring, an estimate can be made how much molecular gas goes into stars, how much survives and how much is photo-dissociated, thus closing the loop on the ISM life-cycle.

The KINGFISH survey (Kennicutt et al., 2011) has been set up to answer this and other questions related to the heating and cooling of the ISM. As part of this survey, I have already started an investigation into the heating of the ISM in the circumnuclear ring of the nearby galaxy NGC 4736. This galaxy is very bright in the NUV and FUV bands of GALEX and $H\alpha$, indicating recent strong star formation.

# A

# Appendix

Table A.1: Star cluster ages, extinctions and masses in the circumnuclear star forming rings of NGC 5248

| ID | Age [Myr] | E(B-V) | log(Mass/M$_\odot$) | $\chi^2$/d.f. |
|----|-----------|--------|---------------------|---------------|
| 001 | 6 | 0.00 | 4.8 | 18.29 |
| 002 | 90 | 0.05 | 5.4 | 12.98 |
| 003 | 16 | 0.00 | 4.8 | 10.23 |
| 004 | 38 | 0.06 | 5.0 | 4.19 |
| 005 | 22 | 0.38 | 5.0 | 10.87 |
| 006 | 46 | 0.12 | 5.0 | 3.13 |
| 007 | 6 | 0.00 | 4.0 | 6.31 |
| 008 | 6 | 0.15 | 4.0 | 5.60 |
| 009 | 6 | 0.20 | 4.0 | 6.93 |
| 010 | 52 | 0.00 | 4.8 | 10.87 |
| 011 | 28 | 0.00 | 4.6 | 7.61 |
| 012 | 50 | 0.04 | 4.8 | 9.20 |
| 013 | 6 | 0.05 | 3.8 | 6.54 |
| 014 | 6 | 0.25 | 4.0 | 3.87 |
| 015 | 42 | 0.00 | 4.6 | 4.16 |
| 016 | 34 | 0.07 | 4.6 | 0.34 |
| 017 | 44 | 0.00 | 4.6 | 5.41 |
| 018 | 22 | 0.37 | 4.6 | 12.36 |
| 019 | 26 | 0.00 | 4.4 | 3.31 |
| 020 | 122 | 0.18 | 5.0 | 4.50 |
| 021 | 28 | 0.01 | 4.4 | 11.30 |
| 022 | 34 | 0.27 | 4.6 | 1.57 |
| 023 | 38 | 0.22 | 4.6 | 1.26 |
| 024 | 122 | 0.23 | 5.0 | 5.19 |
| 025 | 6 | 0.36 | 3.8 | 10.19 |
| 026 | 12 | 0.00 | 4.0 | 3.01 |
| 029 | 36 | 0.00 | 4.4 | 4.56 |

Table A.1 – continued from previous page

| ID | Age [Myr] | E(B-V) | log(Mass/$M_\odot$) | $\chi^2$/d.f. |
|-----|-----|-----|-----|-----|
| 030 | 122 | 1.00 | 5.4 | 16.86 |
| 032 | 122 | 0.56 | 5.2 | 13.40 |
| 033 | 122 | 0.11 | 4.8 | 2.79 |
| 034 | 30 | 0.17 | 4.4 | 2.90 |
| 036 | 220 | 0.51 | 5.2 | 0.52 |
| 037 | 998 | 0.42 | 5.6 | 4.07 |
| 038 | 20 | 0.00 | 4.2 | 1.03 |
| 039 | 122 | 0.13 | 4.8 | 3.47 |
| 040 | 14 | 0.00 | 4.0 | 0.76 |
| 041 | 122 | 0.49 | 5.0 | 3.22 |
| 042 | 20 | 0.03 | 4.2 | 6.11 |
| 043 | 122 | 0.47 | 5.0 | 3.09 |
| 044 | 6 | 0.16 | 3.6 | 0.32 |
| 045 | 42 | 0.00 | 4.4 | 1.15 |
| 046 | 150 | 0.12 | 4.8 | 0.52 |
| 048 | 14 | 0.01 | 4.0 | 0.79 |
| 052 | 850 | 1.86 | 6.4 | 45.91 |
| 053 | 16 | 0.27 | 4.2 | 5.03 |
| 054 | 124 | 0.31 | 4.8 | 0.08 |
| 055 | 26 | 0.00 | 4.2 | 1.90 |
| 056 | 52 | 0.09 | 4.4 | 3.33 |
| 057 | 122 | 0.14 | 4.8 | 6.24 |
| 058 | 132 | 1.94 | 5.8 | 6.75 |
| 059 | 16 | 0.00 | 4.0 | 4.91 |
| 060 | 6 | 0.38 | 3.6 | 2.49 |
| 062 | 212 | 0.09 | 4.8 | 0.34 |
| 063 | 30 | 0.35 | 4.4 | 1.49 |
| 064 | 16 | 0.69 | 4.4 | 3.71 |
| 065 | 122 | 0.31 | 4.8 | 0.31 |
| 066 | 6 | 0.14 | 3.4 | 1.73 |
| 067 | 30 | 0.00 | 4.2 | 4.40 |
| 068 | 122 | 0.40 | 4.8 | 4.25 |
| 069 | 132 | 0.06 | 4.6 | 0.14 |
| 070 | 122 | 0.03 | 4.6 | 2.74 |
| 071 | 112 | 0.00 | 4.6 | 2.49 |
| 072 | 36 | 0.01 | 4.2 | 0.42 |
| 073 | 30 | 0.02 | 4.2 | 0.18 |
| 074 | 22 | 0.23 | 4.2 | 3.69 |
| 075 | 122 | 0.41 | 4.8 | 1.05 |
| 078 | 190 | 0.21 | 4.8 | 0.19 |
| 079 | 16 | 0.12 | 4.0 | 0.76 |
| 081 | 44 | 0.00 | 4.2 | 0.31 |
| 082 | 246 | 1.03 | 5.4 | 2.38 |

– Continued on next page

Table A.1 – continued from previous page

| ID | Age [Myr] | E(B-V) | log(Mass/M$_\odot$) | $\chi^2$/d.f. |
|-----|-----|-----|-----|-----|
| 083 | 6 | 0.14 | 3.4 | 1.78 |
| 084 | 122 | 0.06 | 4.6 | 1.67 |
| 087 | 122 | 0.07 | 4.6 | 4.25 |
| 088 | 122 | 0.76 | 5.0 | 5.81 |
| 089 | 122 | 0.45 | 4.8 | 1.73 |
| 090 | 122 | 1.01 | 5.2 | 18.45 |
| 091 | 136 | 1.12 | 5.2 | 5.07 |
| 094 | 32 | 0.48 | 4.4 | 1.22 |
| 095 | 122 | 0.13 | 4.6 | 0.31 |
| 096 | 122 | 1.39 | 5.4 | 16.53 |
| 097 | 132 | 0.47 | 4.8 | 0.75 |
| 098 | 132 | 0.17 | 4.6 | 0.63 |
| 099 | 132 | 1.12 | 5.2 | 8.68 |
| 100 | 122 | 0.79 | 5.0 | 3.64 |
| 102 | 850 | 0.75 | 5.6 | 5.65 |
| 103 | 152 | 0.08 | 4.6 | 1.80 |
| 104 | 16 | 1.78 | 5.0 | 7.55 |
| 106 | 850 | 0.81 | 5.6 | 9.51 |
| 107 | 122 | 1.13 | 5.2 | 0.44 |
| 108 | 16 | 0.54 | 4.2 | 16.84 |
| 110 | 140 | 0.18 | 4.6 | 0.54 |
| 111 | 16 | 0.49 | 4.2 | 3.73 |
| 112 | 54 | 0.00 | 4.2 | 3.11 |
| 113 | 6 | 0.18 | 3.4 | 1.23 |
| 114 | 28 | 0.32 | 4.2 | 2.64 |
| 115 | 544 | 0.40 | 5.2 | 2.17 |
| 116 | 122 | 0.52 | 4.8 | 8.81 |
| 117 | 122 | 0.79 | 5.0 | 3.87 |
| 118 | 6 | 0.03 | 3.2 | 1.95 |
| 119 | 16 | 1.38 | 4.8 | 2.53 |
| 120 | 24 | 0.00 | 4.0 | 0.08 |
| 121 | 22 | 0.09 | 4.0 | 2.44 |
| 122 | 104 | 0.00 | 4.4 | 6.49 |
| 123 | 122 | 0.57 | 4.8 | 3.44 |
| 125 | 124 | 0.60 | 4.8 | 0.90 |
| 126 | 16 | 0.21 | 4.0 | 0.88 |
| 127 | 122 | 0.25 | 4.6 | 0.92 |
| 128 | 16 | 0.21 | 4.0 | 6.21 |
| 129 | 120 | 0.00 | 4.4 | 0.30 |
| 130 | 136 | 0.94 | 5.0 | 3.48 |
| 131 | 262 | 0.00 | 4.6 | 2.35 |
| 132 | 124 | 0.63 | 4.8 | 4.42 |
| 133 | 102 | 0.07 | 4.4 | 0.79 |

Table A.1 – continued from previous page

| ID | Age [Myr] | E(B-V) | $\log(\text{Mass}/\text{M}_\odot)$ | $\chi^2$/d.f. |
|-----|-----------|--------|-----------|--------|
| 135 | 124 | 0.61 | 4.8 | 2.62 |
| 136 | 280 | 0.56 | 5.0 | 0.38 |
| 137 | 114 | 0.00 | 4.4 | 3.70 |
| 139 | 172 | 0.79 | 5.0 | 0.38 |
| 140 | 106 | 0.38 | 4.6 | 0.25 |
| 141 | 484 | 0.57 | 5.2 | 0.76 |
| 142 | 264 | 0.59 | 5.0 | 0.41 |
| 143 | 16 | 1.34 | 4.6 | 7.60 |
| 146 | 122 | 0.33 | 4.6 | 1.86 |
| 147 | 202 | 0.47 | 4.8 | 2.82 |
| 149 | 122 | 0.00 | 4.4 | 0.74 |
| 150 | 122 | 1.54 | 5.4 | 12.93 |
| 151 | 850 | 0.59 | 5.4 | 2.54 |
| 155 | 34 | 0.00 | 4.0 | 0.10 |
| 156 | 92 | 0.00 | 4.2 | 0.38 |
| 157 | 850 | 1.27 | 5.8 | 9.61 |
| 158 | 802 | 0.00 | 5.0 | 1.42 |
| 159 | 16 | 1.34 | 4.6 | 4.08 |
| 160 | 122 | 0.07 | 4.4 | 0.59 |
| 161 | 202 | 0.46 | 4.8 | 0.68 |
| 162 | 16 | 1.31 | 4.6 | 6.06 |
| 163 | 836 | 0.31 | 5.2 | 1.78 |
| 165 | 850 | 0.72 | 5.4 | 2.99 |
| 167 | 850 | 0.71 | 5.4 | 4.03 |
| 168 | 132 | 1.06 | 5.0 | 3.49 |
| 171 | 850 | 0.07 | 5.0 | 2.77 |
| 172 | 122 | 1.05 | 5.0 | 13.68 |
| 175 | 850 | 1.32 | 5.8 | 19.25 |
| 176 | 202 | 0.20 | 4.6 | 0.34 |
| 177 | 626 | 0.00 | 4.8 | 0.31 |
| 179 | 226 | 0.46 | 4.8 | 0.33 |
| 180 | 34 | 0.12 | 4.0 | 1.32 |
| 182 | 104 | 0.26 | 4.4 | 1.15 |
| 183 | 68 | 0.74 | 4.6 | 0.09 |
| 184 | 948 | 0.73 | 5.4 | 3.50 |
| 185 | 122 | 0.65 | 4.8 | 8.75 |
| 186 | 850 | 1.07 | 5.6 | 20.19 |
| 187 | 38 | 0.02 | 4.0 | 0.21 |
| 188 | 972 | 0.10 | 5.0 | 0.29 |
| 189 | 334 | 0.64 | 5.0 | 0.53 |
| 190 | 850 | 0.31 | 5.2 | 8.27 |
| 191 | 100 | 0.00 | 4.2 | 0.27 |
| 193 | 38 | 0.05 | 4.0 | 0.11 |

Table A.1 – continued from previous page

| ID | Age [Myr] | E(B-V) | log(Mass/M$_\odot$) | $\chi^2$/d.f. |
|----|-----------|--------|---------------------|---------------|
| 194 | 72 | 0.15 | 4.2 | 0.02 |
| 195 | 122 | 0.14 | 4.4 | 0.24 |
| 197 | 122 | 0.47 | 4.6 | 1.14 |
| 198 | 18 | 0.08 | 3.8 | 0.24 |
| 199 | 668 | 0.02 | 4.8 | 0.57 |
| 200 | 122 | 1.13 | 5.0 | 5.03 |
| 201 | 850 | 1.73 | 6.0 | 15.51 |
| 203 | 156 | 0.77 | 4.8 | 2.43 |
| 204 | 850 | 0.16 | 5.0 | 1.63 |
| 207 | 122 | 0.20 | 4.4 | 0.21 |
| 208 | 132 | 1.17 | 5.0 | 4.33 |
| 210 | 36 | 0.17 | 4.0 | 0.41 |
| 211 | 238 | 0.53 | 4.8 | 0.44 |
| 213 | 16 | 0.37 | 4.0 | 4.24 |
| 214 | 22 | 1.33 | 4.6 | 1.81 |
| 216 | 136 | 1.49 | 5.2 | 4.25 |
| 217 | 998 | 0.78 | 5.4 | 0.70 |
| 218 | 16 | 0.79 | 4.2 | 6.47 |
| 219 | 16 | 1.48 | 4.6 | 5.83 |
| 220 | 16 | 0.88 | 4.2 | 2.49 |
| 221 | 132 | 0.89 | 4.8 | 3.13 |
| 222 | 16 | 1.57 | 4.6 | 3.12 |
| 223 | 850 | 2.11 | 6.2 | 8.27 |
| 224 | 126 | 0.88 | 4.8 | 2.75 |
| 225 | 378 | 0.65 | 5.0 | 0.50 |
| 226 | 850 | 0.22 | 5.0 | 0.69 |
| 227 | 850 | 0.50 | 5.2 | 2.78 |
| 229 | 16 | 2.17 | 5.0 | 3.36 |
| 231 | 482 | 0.84 | 5.2 | 0.18 |
| 232 | 124 | 1.84 | 5.4 | 19.71 |
| 233 | 948 | 0.55 | 5.2 | 2.02 |
| 234 | 136 | 1.20 | 5.0 | 4.05 |
| 237 | 668 | 0.03 | 4.8 | 1.69 |
| 239 | 122 | 0.94 | 4.8 | 1.07 |
| 241 | 104 | 0.07 | 4.2 | 0.26 |
| 242 | 122 | 0.26 | 4.4 | 0.73 |
| 243 | 122 | 1.53 | 5.2 | 25.08 |
| 244 | 322 | 0.20 | 4.6 | 0.05 |
| 245 | 850 | 0.64 | 5.2 | 2.57 |
| 247 | 26 | 0.00 | 3.8 | 0.27 |
| 248 | 126 | 1.61 | 5.2 | 16.14 |
| 250 | 968 | 0.30 | 5.0 | 0.37 |
| 251 | 354 | 0.47 | 4.8 | 0.15 |

Table A.1 – continued from previous page

| ID | Age [Myr] | E(B-V) | log(Mass/M$_\odot$) | $\chi^2$/d.f. |
|---|---|---|---|---|
| 253 | 32 | 0.00 | 3.8 | 0.53 |
| 254 | 116 | 0.09 | 4.2 | 0.21 |
| 256 | 122 | 0.56 | 4.6 | 1.71 |
| 257 | 122 | 1.26 | 5.0 | 9.58 |
| 259 | 122 | 0.07 | 4.2 | 0.10 |
| 261 | 850 | 0.34 | 5.0 | 1.93 |
| 262 | 140 | 0.96 | 4.8 | 1.09 |
| 263 | 20 | 0.29 | 3.8 | 0.78 |
| 264 | 288 | 0.30 | 4.6 | 0.03 |
| 265 | 122 | 1.23 | 5.0 | 5.20 |
| 266 | 850 | 0.99 | 5.4 | 5.22 |
| 268 | 186 | 0.48 | 4.6 | 0.52 |
| 269 | 6 | 0.00 | 3.0 | 2.76 |
| 270 | 140 | 0.05 | 4.2 | 0.05 |
| 271 | 122 | 0.08 | 4.2 | 1.20 |
| 272 | 132 | 0.38 | 4.4 | 0.01 |
| 273 | 16 | 2.44 | 5.2 | 3.03 |
| 275 | 40 | 0.00 | 3.8 | 0.04 |
| 276 | 292 | 0.62 | 4.8 | 0.18 |
| 277 | 122 | 1.66 | 5.2 | 13.95 |
| 278 | 850 | 1.65 | 5.8 | 7.97 |
| 279 | 186 | 0.53 | 4.6 | 0.04 |
| 280 | 76 | 0.05 | 4.0 | 0.24 |
| 281 | 124 | 0.45 | 4.4 | 1.01 |
| 283 | 16 | 1.67 | 4.6 | 5.57 |
| 284 | 260 | 0.41 | 4.6 | 0.09 |
| 285 | 132 | 0.14 | 4.2 | 1.16 |
| 286 | 122 | 1.03 | 4.8 | 1.78 |
| 287 | 16 | 0.16 | 3.6 | 1.98 |
| 289 | 482 | 0.73 | 5.0 | 0.30 |
| 290 | 850 | 0.39 | 5.0 | 4.69 |
| 292 | 14 | 0.01 | 3.4 | 0.09 |
| 293 | 850 | 0.89 | 5.4 | 4.89 |
| 298 | 850 | 1.33 | 5.6 | 4.40 |
| 299 | 132 | 1.40 | 5.0 | 4.13 |
| 300 | 998 | 0.99 | 5.4 | 0.61 |
| 301 | 850 | 0.79 | 5.2 | 2.31 |
| 302 | 122 | 1.04 | 4.8 | 2.16 |
| 304 | 850 | 1.05 | 5.4 | 7.25 |
| 305 | 850 | 0.62 | 5.2 | 2.63 |
| 306 | 16 | 0.67 | 4.0 | 0.16 |
| 307 | 132 | 0.83 | 4.6 | 3.88 |
| 308 | 16 | 0.81 | 4.0 | 1.54 |

Table A.1 – continued from previous page

| ID | Age [Myr] | E(B-V) | log(Mass/$M_\odot$) | $\chi^2$/d.f. |
|---|---|---|---|---|
| 309 | 850 | 2.23 | 6.2 | 19.19 |
| 310 | 124 | 0.50 | 4.4 | 0.47 |
| 311 | 136 | 0.85 | 4.6 | 1.84 |
| 313 | 122 | 0.84 | 4.6 | 5.09 |
| 316 | 0 | 0.26 | 3.0 | 3.56 |
| 317 | 16 | 1.08 | 4.2 | 4.14 |
| 318 | 16 | 0.31 | 3.6 | 1.89 |
| 324 | 122 | 0.18 | 4.2 | 3.84 |
| 325 | 16 | 0.57 | 3.8 | 0.26 |
| 326 | 126 | 0.27 | 4.2 | 0.03 |
| 328 | 108 | 0.29 | 4.2 | 0.14 |
| 331 | 124 | 0.00 | 4.0 | 0.03 |
| 333 | 22 | 0.02 | 3.6 | 1.92 |
| 335 | 24 | 0.45 | 3.8 | 1.65 |
| 336 | 124 | 0.89 | 4.6 | 7.84 |
| 340 | 16 | 0.13 | 3.6 | 0.25 |
| 341 | 850 | 2.73 | 6.4 | 10.58 |
| 342 | 16 | 1.23 | 4.2 | 3.81 |
| 344 | 184 | 0.41 | 4.4 | 0.27 |
| 348 | 50 | 0.99 | 4.4 | 0.07 |
| 351 | 116 | 0.30 | 4.2 | 0.13 |
| 352 | 16 | 0.59 | 3.8 | 0.25 |
| 353 | 850 | 0.80 | 5.2 | 9.46 |
| 354 | 850 | 0.70 | 5.0 | 0.66 |
| 355 | 122 | 0.68 | 4.4 | 0.61 |
| 359 | 16 | 0.83 | 4.0 | 3.52 |
| 361 | 46 | 0.81 | 4.2 | 0.10 |
| 362 | 122 | 0.90 | 4.6 | 4.21 |
| 364 | 38 | 0.59 | 4.0 | 0.19 |
| 365 | 16 | 0.23 | 3.6 | 4.39 |
| 366 | 126 | 0.44 | 4.2 | 0.24 |
| 369 | 122 | 0.73 | 4.4 | 1.14 |
| 370 | 850 | 0.97 | 5.2 | 0.76 |
| 371 | 124 | 2.58 | 5.6 | 14.58 |
| 374 | 850 | 1.61 | 5.6 | 4.44 |
| 377 | 850 | 1.59 | 5.6 | 6.07 |
| 378 | 850 | 2.70 | 6.4 | 23.93 |
| 379 | 16 | 2.94 | 5.2 | 10.26 |
| 381 | 16 | 0.48 | 3.6 | 2.06 |
| 383 | 16 | 1.33 | 4.2 | 5.22 |
| 384 | 576 | 1.00 | 5.0 | 0.10 |
| 386 | 16 | 0.84 | 3.8 | 1.50 |
| 387 | 16 | 1.45 | 4.2 | 3.68 |

Table A.1 – continued from previous page

| ID | Age [Myr] | E(B-V) | log(Mass/M$_\odot$) | $\chi^2$/d.f. |
|---|---|---|---|---|
| 388 | 212 | 0.00 | 4.0 | 0.12 |
| 390 | 122 | 0.48 | 4.2 | 0.50 |
| 392 | 16 | 0.34 | 3.6 | 0.64 |
| 396 | 26 | 0.00 | 3.4 | 0.15 |
| 397 | 122 | 0.58 | 4.2 | 0.84 |
| 401 | 16 | 0.11 | 3.4 | 1.70 |
| 406 | 16 | 0.27 | 3.4 | 4.89 |
| 408 | 16 | 2.91 | 5.0 | 2.71 |
| 409 | 124 | 1.91 | 5.0 | 1.98 |
| 410 | 122 | 0.91 | 4.4 | 1.35 |
| 414 | 850 | 1.81 | 5.6 | 2.43 |
| 418 | 16 | 0.79 | 3.6 | 1.05 |
| 419 | 16 | 2.40 | 4.6 | 16.45 |
| 421 | 726 | 1.10 | 5.0 | 0.02 |
| 423 | 850 | 1.58 | 5.4 | 18.21 |
| 425 | 16 | 2.80 | 5.0 | 27.13 |
| 427 | 122 | 1.59 | 4.8 | 1.49 |
| 428 | 16 | 0.58 | 3.4 | 0.88 |
| 429 | 122 | 0.80 | 4.2 | 0.11 |
| 431 | 122 | 2.92 | 5.6 | 7.55 |
| 438 | 850 | 2.99 | 6.4 | 6.13 |
| 453 | 16 | 1.17 | 3.8 | 0.68 |
| 461 | 16 | 2.82 | 4.6 | 13.81 |

**Notes:** Results of the $\chi^2$ fitting of age (column 2), color excess (column 3) and mass (column 4) of the observed star clusters of NGC 5248. The star cluster ID in column 1 is equal to that in the Maoz et al. (2001) electronic table.

## Acknowledgements

It has been more than 3 years since I have left The Netherlands and started my journey to obtain a PhD degree in Astronomy. After all this time there are still several food items I will bring back with me every time I go home. One of these is a Dutch-Indonesian herb paste to spice beef. I say Dutch-Indonesian, because it is of course a very simplified, 'we-don't-want-to-spend-the-whole-day-in-the-kitchen' version of a more traditional Indonesian dish. As such, the packaging reads (translated):

*Many roads lead to the top of the mountain, but the view is always the same*

This saying has always irked me. It is not true of the beef dish and it is certainly not true of life in general. The path I have travelled and the people that I have met along the way have shaped my view now that I have reached the top of the (PhD) mountain in ways no other path could have. The road has known many ups and downs and has some meanderings over the entire globe.

The road starts almost exactly 4 years ago to the date of my defense with a phone-call I received from Eva. I had worked with her on my Master thesis at Groningen university and for some reason she was impressed enough to ask me to come to Heidelberg to work with her on a PhD project. Within weeks of finally arriving in March of the following year she kicked me out on the road to work with collaborators in Paris. I was terrified! She didn't stop pushing me out the door either, I've also been to Grenoble, Garching, Oxford, Bad Honnef and Pasadena for conferences, workshops and collaboration meetings. Eva, I now thank you for that, for the valuable opportunities and chances you have given me by making me go out and meet people. You also deserve a big thank you for your eternal patience in commenting on each paper draft and thesis chapter I've brought to you.

My biggest meandering during the last 3 years was a 6-month stay in Pasadena this last winter/spring. I want to thank everyone at IPAC, and specifically Phil Appleton and Lee Armus, for funding and hosting me for all that time. My time with you was super, and not only for the weather!

I would like to thank Hans-Walter Rix and Kees Dullemond for reading and grading this thesis and Eva Grebel and Luca Amendola for examining me. A big thank you also goes to all the people I have worked with: Lee Armus, Andrew Baker, Pedro Beirão, Torsten Böker, Frederic Boone, Dario Colombo, Francoise Combes, Gaelle Dumas, Eric Emsellem, Santiago Garcia-Burillo, Brent Groves, Sebastian Haan, Leslie Hunt, Stephane Leon, Guilin Liu, Witold Maciejewski, Sharon Meidt, Richard McDermid, Carole Mundell, Hervé Wozniak.

Doing a PhD isn't all about the work. I couldn't have succeeded without the great friends I have around me (you know who you are!). Each of you have shaped me in one way or another. A few of them deserve a special mention though. Karsten, we were student representatives in very difficult times. We did well, together. Partner. Gisella, mia cara. What more is there to say? You have seen the best and the worst of me. Our sauna visit talks gave me perspective and taught me to relax again. Ioanna, I feel so happy that we will end up in the same city again. Our near-daily chats while I was in Pasadena made me smile, cry, shout, and generally see what is important; love,

friendship and unbound fascination with the world. Michelle, you gave me a home instead of a room on the other side of the world and a sister instead of a landlady. Mi casa es su casa goes both ways, you will always be welcome where ever I end up next. And thank you for bringing all that music into my life.

Finally, I want to acknowledge my parents Cees and Dymph van der Laan. Dad, mum, your pride in my accomplishments and unwavering support has always warmed me and kept me going when the going got tough.

This concludes my ramblings. The thesis is done. I'm off to new horizons.

# Bibliography

Aguerri, J. A. L., Beckman, J. E., & Prieto, M. 1998, AJ, 116, 2136

Allard, E. L., Peletier, R. F., & Knapen, J. H. 2005, ApJ, 633, L25

Armour, J. N., & Ballantyne, D. R. 2012, ApJ, 752, 87

Athanassoula, E. 1992a, MNRAS, 259, 328

—. 1992b, MNRAS, 259, 345

—. 2002, ApJ, 569, L83

—. 2003, MNRAS, 341, 1179

Athanassoula, E., Lambert, J. C., & Dehnen, W. 2005, MNRAS, 363, 496

Bacon, R., et al. 2001, MNRAS, 326, 23

Barth, A. J., Ho, L. C., Filippenko, A. V., & Sargent, W. L. 1995, AJ, 110, 1009

Beck, R. 2005, in Lecture Notes in Physics, Berlin Springer Verlag, Vol. 664, Cosmic
   Magnetic Fields, ed. R. Wielebinski & R. Beck, 41

Bertin, E., & Arnouts, S. 1996, A&AS, 117, 393

Bigiel, F., Leroy, A., Walter, F., Brinks, E., de Blok, W. J. G., Madore, B., & Thornley,
   M. D. 2008, AJ, 136, 2846

Binney, J., & Tremaine, S. 2008, Galactic Dynamics: Second Edition (Princeton Uni-
   versity Press)

Block, D. L., Buta, R., Knapen, J. H., Elmegreen, D. M., Elmegreen, B. G., & Puerari,
   I. 2004, AJ, 128, 183

Böker, T., Falcón-Barroso, J., Schinnerer, E., Knapen, J. H., & Ryder, S. 2008, AJ,
   135, 479

Böker, T., et al. 1999, ApJS, 124, 95

Boone, F., Schilke, P., Muders, D., Comito, C., Leurini, S., Parise, B., van der Tak, F.,
   & Menten, K. 2006, in EAS Publications Series, Vol. 18, EAS Publications Series,
   ed. P. Stee, 299–305

Boone, F., et al. 2007, A&A, 471, 113

Bournaud, F., Combes, F., & Semelin, B. 2005, MNRAS, 364, L18

Braine, J., Combes, F., Casoli, F., Dupraz, C., Gerin, M., Klein, U., Wielebinski, R., &
   Brouillet, N. 1993, A&AS, 97, 887

Buta, R., Block, D. L., & Knapen, J. H. 2003, AJ, 126, 1148

Buta, R., & Combes, F. 1996, Fund. Cosmic Phys., 17, 95

Byrd, G., Rautiainen, P., Salo, H., Buta, R., & Crocher, D. A. 1994, AJ, 108, 476

Calzetti, D., Armus, L., Bohlin, R. C., Kinney, A. L., Koornneef, J., & Storchi-Bergmann, T. 2000, ApJ, 533, 682

Cappellari, M., & Emsellem, E. 2004, PASP, 116, 138

Cardelli, J. A., Clayton, G. C., & Mathis, J. S. 1989, ApJ, 345, 245

Casasola, V., Combes, F., García-Burillo, S., Hunt, L. K., Léon, S., & Baker, A. J. 2008, A&A, 490, 61

Casasola, V., Hunt, L. K., Combes, F., García-Burillo, S., Boone, F., Eckart, A., Neri, R., & Schinnerer, E. 2010, A&A, 510, A52+

Chandrasekhar, S. 1943, ApJ, 97, 255

Combes, F. 2004, in IAU Symposium, Vol. 222, The Interplay Among Black Holes, Stars and ISM in Galactic Nuclei, ed. T. Storchi-Bergmann, L. C. Ho, & H. R. Schmitt, 383–388

Combes, F. 2008, in IAU Symposium, Vol. 245, IAU Symposium, ed. M. Bureau, E. Athanassoula, & B. Barbuy, 151–160

Combes, F., & Gerin, M. 1985, A&A, 150, 327

Combes, F., et al. 2004, A&A, 414, 857

—. 2009, A&A, 503, 73

Comerón, S., Knapen, J. H., Beckman, J. E., Laurikainen, E., Salo, H., Martínez-Valpuesta, I., & Buta, R. J. 2010, MNRAS, 402, 2462

Contopoulos, G., & Papayannopoulos, T. 1980, A&A, 92, 33

de Vaucouleurs, G., de Vaucouleurs, A., Corwin, Jr., H. G., Buta, R. J., Paturel, G., & Fouque, P. 1991, Third Reference Catalogue of Bright Galaxies

Dumas, G., Mundell, C. G., Emsellem, E., & Nagar, N. M. 2007, MNRAS, 379, 1249

Elmegreen, B. G. 1994, ApJ, 425, L73

Emsellem, E., et al. 2004, MNRAS, 352, 721

Englmaier, P., & Shlosman, I. 2000, ApJ, 528, 677

—. 2004, ApJ, 617, L115

Falcón-Barroso, J., Sánchez-Blázquez, P., Vazdekis, A., Ricciardelli, E., Cardiel, N., Cenarro, A. J., Gorgas, J., & Peletier, R. F. 2011, A&A, 532, A95+

Fathi, K., van de Ven, G., Peletier, R. F., Emsellem, E., Falcón-Barroso, J., Cappellari, M., & de Zeeuw, T. 2005, MNRAS, 364, 773

Feldmann, R., Gnedin, N. Y., & Kravtsov, A. V. 2011, ApJ, 732, 115

Ferrarese, L., & Ford, H. 2005, Space Science Reviews, 116, 523

Gao, Y., & Solomon, P. M. 2004, ApJ, 606, 271

García-Burillo, S., Combes, F., Schinnerer, E., Boone, F., & Hunt, L. K. 2005, A&A, 441, 1011

García-Burillo, S., et al. 2003a, A&A, 407, 485

García-Burillo, S., et al. 2003b, in Astronomical Society of the Pacific Conference Series, Vol. 290, Active Galactic Nuclei: From Central Engine to Host Galaxy, ed. S. Collin, F. Combes, & I. Shlosman, 423–+

—. 2009, A&A, 496, 85

—. 2010, A&A, 519, A2

Haan, S., Schinnerer, E., Emsellem, E., García-Burillo, S., Combes, F., Mundell, C. G., & Rix, H.-W. 2009, ApJ, 692, 1623

Haan, S., Schinnerer, E., Mundell, C. G., García-Burillo, S., & Combes, F. 2008, AJ, 135, 232

Helfer, T. T., Thornley, M. D., Regan, M. W., Wong, T., Sheth, K., Vogel, S. N., Blitz, L., & Bock, D. C.-J. 2003, ApJS, 145, 259

Ho, L. C., Filippenko, A. V., & Sargent, W. L. W. 1997, ApJ, 487, 568

Hopkins, P. F., & Quataert, E. 2010, MNRAS, 407, 1529

Hsieh, P.-Y., Matsushita, S., Liu, G., Ho, P. T. P., Oi, N., & Wu, Y.-L. 2011, ApJ, 736, 129

Hummer, D. G., & Storey, P. J. 1987, MNRAS, 224, 801

Hunt, L. K., & Malkan, M. A. 2004, ApJ, 616, 707

Hunt, L. K., et al. 2008, A&A, 482, 133

Jogee, S., Knapen, J. H., Laine, S., Shlosman, I., Scoville, N. Z., & Englmaier, P. 2002a, ApJ, 570, L55

Jogee, S., Scoville, N., & Kenney, J. D. P. 2005, ApJ, 630, 837

Jogee, S., Shlosman, I., Laine, S., Englmaier, P., Knapen, J. H., Scoville, N., & Wilson, C. D. 2002b, ApJ, 575, 156

Jogee, S., et al. 2004, ApJ, 615, L105

Kalnajs, A. J. 1973, Proceedings of the Astronomical Society of Australia, 2, 174

Kaufman, M. J., Wolfire, M. G., Hollenbach, D. J., & Luhman, M. L. 1999, ApJ, 527, 795

Kenney, J. D. P., Wilson, C. D., Scoville, N. Z., Devereux, N. A., & Young, J. S. 1992, ApJ, 395, L79

Kennicutt, R. C., Lee, J. C., Akiyama, S., Funes, J. G., & Sakai, S. 2005, in American Institute of Physics Conference Series, Vol. 783, The Evolution of Starbursts, ed. S. Hüttmeister, E. Manthey, D. Bomans, & K. Weis, 3–16

Kennicutt, R. C., et al. 2011, PASP, 123, 1347

Kennicutt, Jr., R. C. 1989, ApJ, 344, 685

—. 1998a, ARA&A, 36, 189

—. 1998b, ApJ, 498, 541

Kennicutt, Jr, R. C., & Evans, II, N. J. 2012, ArXiv e-prints

Kim, W.-T., Seo, W.-Y., Stone, J. M., Yoon, D., & Teuben, P. J. 2012, ApJ, 747, 60

Knapen, J. H. 2005, A&A, 429, 141

Kohno, K., Kawabe, R., & Vila-Vilaró, B. 1999, ApJ, 511, 157

Kormendy, J., & Kennicutt, Jr., R. C. 2004, ARA&A, 42, 603

Krips, M., et al. 2005, A&A, 442, 479

—. 2007, A&A, 468, L63

Laine, S., Knapen, J. H., Perez-Ramirez, D., Doyon, R., & Nadeau, D. 1999, MNRAS, 302, L33

Laine, S., Knapen, J. H., Pérez-Ramírez, D., Englmaier, P., & Matthias, M. 2001, MNRAS, 324, 891

Leitherer, C., Ortiz Otálvaro, P. A., Bresolin, F., Kudritzki, R., Lo Faro, B., Pauldrach, A. W. A., Pettini, M., & Rix, S. A. 2010, ApJS, 189, 309

Leitherer, C., et al. 1999, ApJS, 123, 3

Leroy, A. K., Walter, F., Brinks, E., Bigiel, F., de Blok, W. J. G., Madore, B., & Thornley, M. D. 2008, AJ, 136, 2782

Leroy, A. K., et al. 2012, AJ, 144, 3

Lindblad, B. 1964, Astrophysica Norvegica, 9, 103

Lindt-Krieg, E., Eckart, A., Neri, R., Krips, M., Pott, J.-U., García-Burillo, S., & Combes, F. 2008, A&A, 479, 377

Maciejewski, W. 2004a, MNRAS, 354, 883

—. 2004b, MNRAS, 354, 892

Maciejewski, W., & Athanassoula, E. 2007, MNRAS, 380, 999

Maciejewski, W., & Small, E. E. 2010, ApJ, 719, 622

Maciejewski, W., Teuben, P. J., Sparke, L. S., & Stone, J. M. 2002, MNRAS, 329, 502

Maoz, D., Barth, A. J., Ho, L. C., Sternberg, A., & Filippenko, A. V. 2001, AJ, 121, 3048

Martini, P., & Pogge, R. W. 1999, AJ, 118, 2646

Mazzuca, L. M., Knapen, J. H., Veilleux, S., & Regan, M. W. 2008, ApJS, 174, 337

McDermid, R., Bacon, R., Adam, G., Benn, C., & Cappellari, M. 2004, in Society of Photo-Optical Instrumentation Engineers (SPIE) Conference Series, Vol. 5492, Society of Photo-Optical Instrumentation Engineers (SPIE) Conference Series, ed. A. F. M. Moorwood & M. Iye, 822–829

Meier, D. S., Turner, J. L., & Hurt, R. L. 2008, ApJ, 675, 281

Meier, D. S., Turner, J. L., & Schinnerer, E. 2011, AJ, 142, 32

Mulchaey, J. S., & Regan, M. W. 1997, ApJ, 482, L135

Mulchaey, J. S., Regan, M. W., & Kundu, A. 1997, ApJS, 110, 299

Murphy, E. J., et al. 2011, ApJ, 737, 67

Osterbrock, D. E. 1989, Astrophysics of gaseous nebulae and active galactic nuclei, ed. Osterbrock, D. E.

Pérez, E., Márquez, I., Marrero, I., Durret, F., González Delgado, R. M., Masegosa, J., Maza, J., & Moles, M. 2000, A&A, 353, 893

Pineda, J. L., Goldsmith, P. F., Chapman, N., Snell, R. L., Li, D., Cambrésy, L., & Brunt, C. 2010, ApJ, 721, 686

Piner, B. G., Stone, J. M., & Teuben, P. J. 1995, ApJ, 449, 508

Prendergast, K. H. 1983, in IAU Symposium, Vol. 100, Internal Kinematics and Dynamics of Galaxies, ed. E. Athanassoula, 215–220

Rees, M. J. 1984, ARA&A, 22, 471

Regan, M. W., & Mulchaey, J. S. 1999, AJ, 117, 2676

Regan, M. W., & Teuben, P. 2003, ApJ, 582, 723

Regan, M. W., & Teuben, P. J. 2004, ApJ, 600, 595

Roussel, H., et al. 2007, ApJ, 669, 959

Rozas, M., Relaño, M., Zurita, A., & Beckman, J. E. 2002, A&A, 386, 42

Ryder, S. D., Knapen, J. H., & Takamiya, M. 2001, MNRAS, 323, 663

Saikia, D. J., Phookun, B., Pedlar, A., & Kohno, K. 2002, A&A, 383, 98

Sakamoto, K., Baker, A. J., & Scoville, N. Z. 2000, ApJ, 533, 149

Sakamoto, K., Okumura, S. K., Ishizuki, S., & Scoville, N. Z. 1999, ApJ, 525, 691

Sánchez-Blázquez, P., et al. 2006, MNRAS, 371, 703

Sarzi, M., et al. 2006, MNRAS, 366, 1151

Schmidt, M. 1959, ApJ, 129, 243

—. 1963, ApJ, 137, 758

Schwarz, M. P. 1981, ApJ, 247, 77

—. 1984, MNRAS, 209, 93

Sheth, K., Vogel, S. N., Regan, M. W., Thornley, M. D., & Teuben, P. J. 2005, ApJ, 632, 217

Sheth, K., et al. 2008, ApJ, 675, 1141

Shlosman, I., Begelman, M. C., & Frank, J. 1990, Nature, 345, 679

Shlosman, I., Frank, J., & Begelman, M. C. 1989, Nature, 338, 45

Solomon, P. M., & Barrett, J. W. 1991, in IAU Symposium, Vol. 146, Dynamics of Galaxies and Their Molecular Cloud Distributions, ed. F. Combes & F. Casoli, 235–+

Sparke, L. S., & Gallagher, III, J. S. 2000, Galaxies in the universe : an introduction

Sternberg, A., & Dalgarno, A. 1995, ApJS, 99, 565

Stetson, P. B. 1987, PASP, 99, 191

Stetson, P. B. 1992, in Astronomical Society of the Pacific Conference Series, Vol. 25, Astronomical Data Analysis Software and Systems I, ed. D. M. Worrall, C. Biemesderfer, & J. Barnes, 297–+

Stetson, P. B., Davis, L. E., & Crabtree, D. R. 1990, in Astronomical Society of the Pacific Conference Series, Vol. 8, CCDs in astronomy, ed. G. H. Jacoby, 289–304

Stoklasová, I., Ferruit, P., Emsellem, E., Jungwiert, B., Pécontal, E., & Sánchez, S. F. 2009, A&A, 500, 1287

Storchi-Bergmann, T., Dors, Jr., O. L., Riffel, R. A., Fathi, K., Axon, D. J., Robinson, A., Marconi, A., & Östlin, G. 2007, ApJ, 670, 959

Tabatabaei, F. S., & Berkhuijsen, E. M. 2010, A&A, 517, A77

Tremaine, S., & Weinberg, M. D. 1984, ApJ, 282, L5

Tully, R. B. 1988, Nearby galaxies catalog, ed. R. B. Tully

Tully, R. B., Rizzi, L., Shaya, E. J., Courtois, H. M., Makarov, D. I., & Jacobs, B. A. 2009, AJ, 138, 323

Usero, A., García-Burillo, S., Fuente, A., Martín-Pintado, J., & Rodríguez-Fernández, N. J. 2004, A&A, 419, 897

Van de Ven, G., & Fathi, K. 2010, ApJ, 723, 767

Van der Hulst, J. M., Terlouw, J. P., Begeman, K. G., Zwitser, W., & Roelfsema, P. R. 1992, in Astronomical Society of the Pacific Conference Series, Vol. 25, Astronomical Data Analysis Software and Systems I, ed. D. M. Worrall, C. Biemesderfer, & J. Barnes, 131–+

Van der Laan, T. P. R., et al. 2011, A&A, 529, A45+

van Dishoeck, E. F., & Black, J. H. 1988, ApJ, 334, 771

Vázquez, G. A., & Leitherer, C. 2005, ApJ, 621, 695

Weedman, D. W., Feldman, F. R., Balzano, V. A., Ramsey, L. W., Sramek, R. A., & Wuu, C.-C. 1981, ApJ, 248, 105

Weiß, A., Neininger, N., Hüttemeister, S., & Klein, U. 2001, A&A, 365, 571

Wu, J., Evans, II, N. J., Shirley, Y. L., & Knez, C. 2010, ApJS, 188, 313

Young, J. S., et al. 1995, ApJS, 98, 219